



BRNO UNIVERSITY OF TECHNOLOGY

VYSOKÉ UČENÍ TECHNICKÉ V BRNĚ

FACULTY OF MECHANICAL ENGINEERING

FAKULTA STROJNÍHO INŽENÝRSTVÍ

INSTITUTE OF SOLID MECHANICS, MECHATRONICS AND BIOMECHANICS

ÚSTAV MECHANIKY TĚLES, MECHATRONIKY A BIOMECHANIKY

DESIGN OF MINIATURE SPECIMENS FOR CALIBRATION OF DUCTILE FRACTURE CRITERIA

NÁVRH MINIATURNÍCH TĚLES PRO KALIBRACI KRITÉRIÍ TVÁRNÉHO PORUŠOVÁNÍ

MASTER'S THESIS

DIPLOMOVÁ PRÁCE

AUTHOR

AUTOR PRÁCE

Bc. Patrik Salvét

SUPERVISOR

VEDOUCÍ PRÁCE

**doc. Ing. František Šebek,
Ph.D.**

BRNO 2023

Assignment Master's Thesis

Institut: Institute of Solid Mechanics, Mechatronics and Biomechanics
Student: **Bc. Patrik Salvét**
Degree program: Engineering Mechanics and Biomechanics
Branch: Engineering Mechanics
Supervisor: **doc. Ing. František Šebek, Ph.D.**
Academic year: 2022/23

As provided for by the Act No. 111/98 Coll. on higher education institutions and the BUT Study and Examination Regulations, the director of the Institute hereby assigns the following topic of Master's Thesis:

Design of miniature specimens for calibration of ductile fracture criteria

Brief Description:

The ductile fracture of ductile metallic materials needs to be studied with respect to various industrial sectors. However, there is not always enough material available, therefore, it is needed to recourse to the testing of miniature specimens. These may have various shapes with respect to the nature of ductile fracture criteria calibration.

Master's Thesis goals:

1. Survey on testing of miniature specimens taking into consideration the ductile fracture.
2. Design of miniature specimens for testing on developed uniaxial testing device.
3. Numerical simulations of respective tests with respect to the calibration of ductile fracture criteria on basis of given data.
4. Assessment of obtained results and recommendation for future work.

Recommended bibliography:

GORJI, M. B. and D. MOHR. Micro-tension and micro-shear experiments to characterize stress-state dependent ductile fracture. Acta Materialia, vol. 131, pp. 65-76, DOI:10.1016/j.actamat.2017.03.034, 2017.

KIM, J. S. and H. HUH. Evaluation of the material properties of an OFHC copper film at high strain rates using a micro-testing machine. Experimental Mechanics, vol. 51, pp. 845-855, DOI:10.1007/s11340-010-9395-6, 2011.

LI, L., G. NGAILE and T. HASSAN. A novel hybrid heating method for mechanical testing of miniature specimens at elevated temperature. Journal of Micro and Nano-Manufacturing, vol. 5, issue 2, pp. 1-5, DOI:10.1115/1.4035954, 2017.

LI, L., Y.-Ch. CHAN, G. NGAILE and T. HASSAN. A novel gripper for multiaxial mechanical testing of microtubes at elevated temperatures. Review of Scientific Instruments, vol. 91, issue 5, pp. 1-12, DOI:10.1063/5.0007150, 2020.

VAN PETEGEM, S., A. GUITTON, M. DUPRAZ, A. BOLLHALDER, K. SOFINOWSKI, M. V. UPADHYAY and H. VAN SWYGENHOVEN. A miniaturized biaxial deformation rig for in situ mechanical testing. Experimental Mechanics, vol. 57, pp. 569-580, DOI:10.1007/s11340-016-0244-0, 2017.

RAHMAN, F., G. NGAILE and T. HASSAN. Development of scanning electron microscope-compatible multiaxial miniature testing system. Measurement Science and Technology, vol. 30, issue 10, pp. 1-17, DOI:10.1088/1361-6501/ab1ca6, 2019.

RAHMAN, F., G. NGAILE and T. HASSAN. Optimized stereo digital image correlation setup for miniature round specimen: framework development and implementation. Optics and Lasers in Engineering, vol. 144, pp. 1-14, DOI:10.1016/j.optlaseng.2021.106555, 2021.

Deadline for submission Master's Thesis is given by the Schedule of the Academic year 2022/23

In Brno,

L. S.

prof. Ing. Jindřich Petruška, CSc.
Director of the Institute

doc. Ing. Jiří Hlinka, Ph.D.
FME dean

ABSTRACT

Numerical simulations have been rapidly progressing in recent years due to an increasing computational capacity. Finite element method has a great potential to partially replace and complement experiments, which are expensive, time consuming, and often difficult to perform. One of the major applications of numerical simulations is the prediction and simulation of material behavior. This thesis deals with the calibration and comparison of various phenomenological ductile fracture criteria dependent on stress triaxiality and third invariant of the deviatoric stress tensor, which can be implemented in finite element method to predict crack propagation. The ductile fracture criteria have been calibrated for aluminium alloy 2024-T351 using macroscopic samples. The calibration was done in MATLAB by approximating the calibration points with the ductile fracture criterion using the particle swarm optimization. Hookes's law, a new recently proposed plasticity model, and an uncoupled ductile fracture model calibrated by the macroscopic samples have been implemented into Abaqus/Explicit to design four miniature specimens for an already designed tensile testing device. The designed miniature specimens capture various stress states in the fracture initiation zone, including uniaxial tension, shear stress, and plane strain. Based on a combination of experimental measurements and numerical simulations of these samples, the ductile fracture criteria can be calibrated to determine the suitability of miniature samples for the prediction of ductile fracture initiation and propagation.

KEYWORDS

Aluminium alloy, calibration of material parameters, ductile fracture, fracture initiation, miniature specimens, model of plasticity, numerical simulation.

ABSTRAKT

Numerické simulace se v posledních letech s rostoucí výpočetní kapacitou výrazně rozšiřují. Metoda konečných prvků má velký potenciál k tomu, aby částečně nahradila a doplnila experimenty, které jsou drahé, zdoluhavé a často obtížně proveditelné. Jedno z hlavních využití numerických simulací je predikce a simulace chování materiálu. Tato diplomová práce se zabývá kalibrací a porovnáním různých fenomenologických kritérií tvárného porušování závislých na triaxialitě napětí a třetím invariantu tenzoru deviátoru napětí, které lze implementovat do metody konečných prvků k predikci růstu trhliny. Tato kritéria tvárného porušení byla kalibrována pro slitinu hliníku 2024-T351 s využitím makroskopických vzorků. Kalibrace byla provedena v MATLABU aproximací kalibračních bodů kritériem tvárného porušování s využitím optimalizační metody hejna částic. Hookův zákon, nový nedávno publikovaný model plasticity a nesvázaný model tvárného porušování kalibrovány pomocí makroskopických vzorků byly implementovány do Abaqusu/Explicit za účelem navrhnutí čtyř miniaturních vzorků pro již sestavené zkušební tahové zařízení. Navržené miniaturní vzorky zachycují různé typy napjatosti v místě iniciace trhliny zahrnující jednoosou napjatost, smykovou napjatost a rovinnou deformaci. Kombinací experimentů a numerických simulací těchto vzorků lze provést kalibraci kritérií tvárného porušování za účelem stanovení vhodnosti miniaturních vzorků pro predikci iniciace a šíření tvárného lomu.

KLÍČOVÁ SLOVA

Slitina hliníku, kalibrace materiálových parametrů, tvárný lom, iniciace lomu, miniaturní vzorky, model plasticity, numerická simulace.

BIBLIOGRAPHIC CITATION

SALVET, Patrik. *Návrh miniaturních těles pro kalibraci kritérií tvárného porušování* [online]. Brno, 2023. Dostupné také z: <https://www.vutbr.cz/studenti/zav-prace/detail/146390>. Diplomová práce. Vysoké učení technické v Brně, Fakulta strojního inženýrství, Ústav mechaniky těles, mechatroniky a biomechaniky. Vedoucí práce František Šebek.

DECLARATION

I hereby declare that I have written this master's thesis on my own, under the supervision of doc. Ing. František Šebek, Ph.D., using the literature included in the list of references.

Brno, 23.05.2023

.....

Bc. Patrik Salvét

ACKNOWLEDGEMENT

I would like to thank my family for their support during my studies and doc. Ing. František Šebek, Ph.D., for his guidance throughout the writing of this thesis and his valuable advice.

CONTENTS

1	Introduction	11
1.1	Motivation.....	11
1.2	Formulation of the problem situation	11
1.3	Problem formulation and solution	12
1.4	Goal of the thesis	12
2	State of the art.....	13
2.1	Ductile fracture mechanism	13
2.2	Size effect	15
2.3	Miniature specimen testing methods	16
3	Stress state	19
3.1	Stress and strain variables	19
3.2	Characterization of the stress state.....	22
3.3	Geometrical representation of the stress state.....	26
4	Simple overview of material modelling	28
4.1	Numerical simulations	28
4.2	Plasticity.....	30
4.2.1	Yield criteria	30
4.2.2	Flow rules	31
4.2.3	Hardening rules	31
4.3	Damage parameter	33
4.4	Fracture models.....	34
5	Material models	37
5.1	Model of elasticity	37
5.2	Constitutive law	37
5.3	Yield criterion	38
5.4	Ductile fracture criteria	42
5.4.1	Modified Mohr–Coulomb criterion	42
5.4.2	Ganjani fracture criterion	43
5.4.3	KHPS2	43
5.4.4	Lou–Huh fracture criterion.....	45
6	Calibration	46
6.1	Calibration of the ductile fracture criteria.....	46
6.2	Influence of initial guess and minimized residuum formulation	51
7	Specimen design using numerical simulations	53
8	Experimental program.....	62
8.1	Aluminium alloy EN AW 2024-T351	62
8.2	Test apparatus	62
8.3	Specimen preparation	63
8.4	Experiments	64
8.4.1	Experiments of the notched specimens	65
8.4.2	Experiments of the shear specimens.....	66

8.4.3	Experiments of the plane strain specimens	66
8.4.4	Experiments of the uniaxial specimens.....	67
8.4.5	Summary of the experiments	68
8.4.6	Small punch test.....	68
Conclusion and suggestions for future studies		71
References		73
List of used abbreviations and symbols		80
List of figures.....		83

1 INTRODUCTION

1.1 MOTIVATION

Ductile fracture is a common failure mechanism that causes significant complications in many engineering industries. Materials fracture when the forces acting on the material exceed its load-bearing capacity. Most metals used in civil engineering, transportation, military industry, etc. exhibit ductile behavior to some degree, therefore, ductile fracture prediction has been a very important topic for decades. A better understanding of material behavior would allow us to further reduce the weight of structures while maintaining their reliability. Structure optimization allows companies to produce cheaper products and maintain their cost competitiveness. The optimization process is widely used in the automotive and aerospace industries, where the reduced weight of the vehicle allows for faster travel and reduces fuel consumption. Furthermore, many disasters associated with bridge collapses, aeroplane, and ship crashes could be prevented by a better understanding of the fracture mechanism.

Ductile fracture is caused by nucleation, growth, and coalescence of voids that already exist within the material or nucleate during plastic deformation. The ductile fracture is assumed to occur when the ductility is exhausted. The critical value of strain required for rupture varies depending on the stress state, which can be characterized using various stress-related parameters, such as stress triaxiality, third invariant of deviatoric stress tensor, or Lode angle. The fracture strain for different stress states can be obtained experimentally or numerically. The experiments can be performed on macroscopic or microscopic samples.

Miniature testing methods have roots in the nuclear industry, where the material was too dangerous to handle in large quantities. Thus, it was important to find a way to determine the properties of a material from a small amount of material without risking excessive irradiation. The number of possible miniature testing methods was later extended and began to be utilized in various fields of application. Although miniature testing methods require less material, it should be noted that they also have limitations and disadvantages, which are described further in the thesis. The main limitations are related to a size effect and problematic sample preparation.

Although experiments are the most reliable source of information, they are expensive and time-consuming. Therefore, experiments are often complemented by numerical simulations, which have been progressively developing in recent years. Many ductile fracture criteria have been proposed on a basis of various physical concepts. They must first be verified and calibrated before being used to solve practical problems. They must also be suitable for numerical implementation with a minimum number of material parameters that must be calibrated. Not all of the criteria are equal, but with accurate numerical models, we can quickly and easily analyse the safety and optimise geometry of complex structures. [1].

1.2 FORMULATION OF THE PROBLEM SITUATION

Material parameters of material models are generally calibrated using standardized macroscopic specimens. However, the experiments performed on these specimens require a large amount of material, as each experiment is performed several times to reduce the result deviation. Sometimes only a limited amount of material is available, for example when the material is scarce or when working with irradiated material. The advantage of experiments

performed on small specimens is that they allow the mechanical properties to be characterized using a small volume of material. In addition to the typical mechanical characteristics obtained from the stress–strain curve, miniature testing methods can also be used for fatigue, creep, or fracture analysis.

The experiments performed on miniature specimens are very promising for estimating the remaining life of structures, as they require a minimal amount of material and the repair process after material removal is either unnecessary or simple, unlike macro-tests which significantly disrupt the structure. The samples required for macro-experiments are often very difficult or even impossible to extract, which further increases the need for miniature specimen experiments.

However, studies have shown that experiments conducted on extremely small specimens are significantly affected by the so-called size effect. The experimental results affected by the size effect no longer represent the bulk of the material. It is important to know the threshold at which the results are invalidated by this phenomenon, as incorrectly calibrated material parameters can lead to unexpected component failure.

1.3 PROBLEM FORMULATION AND SOLUTION

The problem is to design simple and easily manufacturable miniature specimens that cover a wide range of stress states and can be used to evaluate the applicability of miniature specimens for the prediction of ductile fracture.

To investigate the applicability of miniature specimens for the calibration of ductile fracture criteria, it is necessary to design several specimens that capture various stress states such as shear, uniaxial tension, plane strain, etc. For their design, the ductile fracture criteria, as well as other material models must already be calibrated and implemented in Finite Element Method (FEM). The calibration of the ductile fracture criteria is carried out by approximating the experimental points from macro-tests with the criterion equation, from which the material parameters are obtained. Then, experimental fracture tests are used to determine the displacement at which fracture initiation occurs. By simulating the miniature experiments and extracting the values of η , ξ and $\bar{\epsilon}_p$ at this displacement, the ductile fracture criteria can be calibrated using miniature specimens. Finally, its application for macro-samples or comparison with a criterion calibrated using macro-samples is required to determine the effect of miniaturization.

1.4 GOAL OF THE THESIS

- Research on the topic of miniature specimen testing for ductile fracture prediction.
- Design of miniature specimens for experiments on an already designed uniaxial tensile device.
- Numerical simulation of the experiments using provided data.
- Calibration of the ductile fracture criteria.
- Evaluation of the results.
- Recommendations for further work.

2 STATE OF THE ART

2.1 DUCTILE FRACTURE MECHANISM

Fracture can be defined as separation of a material into two or more pieces by the action of stress. This phenomenon occurs when the material is loaded beyond its ultimate strength and loses its load-bearing ability. Based on the crack growth mechanism, the fracture can be divided into brittle or ductile. The main difference between the brittle and the ductile fracture is in the magnitude of plastic deformation. Ductile materials exhibit an appreciable plastic deformation before separation, in contrast to brittle materials where the fracture occurs suddenly without warning and is accompanied by rapid crack propagation. The plastic deformation of ductile materials is slow and sometimes gives a warning before the final rupture, allowing preventive measures to be taken. Another advantageous characteristic of ductile materials is the amount of energy required for rupture, which is significantly greater for ductile materials than for brittle materials. This property is utilized in components such as dampers. [2], [3], [4], [5].

The most common and simplest experiment to determine the type of fracture is the tensile test. The type of fracture can be distinguished by the appearance and shape of the fracture surface. Brittle materials are characterized by a shiny fracture surface and the crack cross-sectional area does not exhibit significant necking. This feature is generally observed in high-strength materials. The fracture strain of brittle materials is less than 5 %. Even materials that normally exhibit ductile behaviour can become brittle under certain conditions. The most common cause of this shift is a change in temperature. Many materials exhibit ductile behaviour at regular or elevated temperatures and brittle behaviour at low temperatures. From a macroscopic point of view, ductile failure generally occurs following these steps: necking, formation of small cavities, crack formation, cup and cone fracture. [2], [3], [6].

Three typical stages of the ductile fracture mechanism from a microscopic point of view according to literature [7] are void initiation, growth, and coalescence. These three stages are described in more detail below.

A. Void initiation

The initiation of ductile fracture starts with the formation of micro-voids, which either already exist within the material or nucleate during deformation at inclusions and second-phase particles. The voids nucleate at inclusions and second-phase particles due to a mechanical weakness in these locations compared to the remaining areas. The mechanical properties of the material are therefore significantly affected by the amount of impurities. The voids do not initiate at all particles simultaneously, even if the material contains only one type of second-phase particles. They generally nucleate at larger particles first, although this is also influenced by the shape of the particle, its orientation, and by the strength of the particle-matrix bond. Micro-voids that nucleated first grow, while other voids continue to nucleate at smaller particles during the continuous fracture process. If the material contains several types of second-phase particles, the voids usually appear first at a particular particle type and later in the process at another particle type. Not every particle initiates voids, but they may still indirectly influence the fracture process by affecting the flow characteristics of the matrix. The state of stress affects the strain at which the voids nucleate. The voids

nucleate at lower strains with increasing stress triaxiality and second-phase particle size. The strain at which the voids nucleate can be influenced by a modification of the cohesive particle-matrix bond strength. It has been shown that particle-matrix decohesion occurs first along the axis of applied stress in the region where the hydrostatic tensile stress reaches its maximum value. In the case of tensile experiments, this typically occurs in the centre of the neck. [6], [7].

In addition to the void initiation caused by the matrix-particle interface decohesion described above, void initiation can also be caused by a fracture of the second-phase particle. In this case, the fracture is confined to the particular second-phase particle, although there are cases where the cracks are observed to run some distance into the matrix. [7], [8].

B. Void growth

Once the voids nucleate, the porosity increases and develops by plastic deformation and by coalescence of cavities. The cavities cannot grow without plastic deformation. The void growth is assumed to be caused by the motion of dislocations. Stress triaxiality plays an important role in determining both the void growth rate and the void shape. It has also been proven that strain hardening of the matrix suppresses void growth. [7], [8].

C. Void coalescence

The final stage of the ductile fracture process is the void coalescence. In this stage, the formed cavities coalesce with each other in a flat direction in the centre of the neck. The connected cavities form a crack that is generally perpendicular to the direction of applied tensile stress. The internal crack propagates and causes separation of the material. [6], [7].

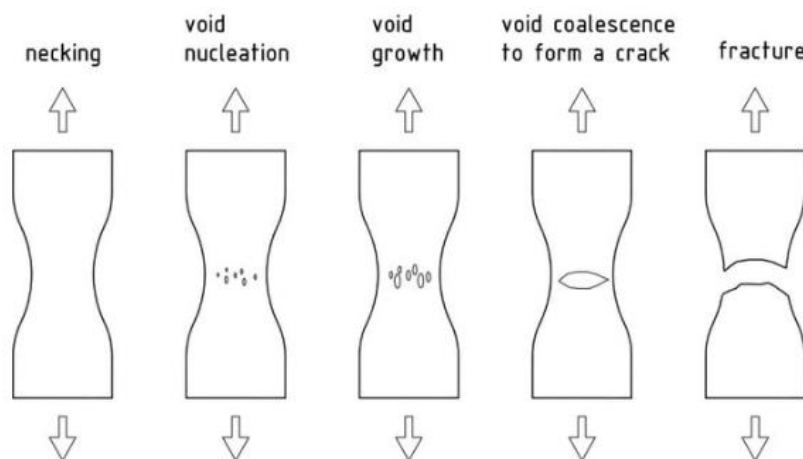


Fig. 1 Stages of the ductile fracture process [9]

Dimples caused by formation and coalescence of micro-voids can be observed on the surface of the fracture. After failure, the cross-section is distorted, reduced, and in some materials, such as steels, shear lips forming a cup and cone shape can be observed at the lateral part of the cracks. The cup and cone fracture is called by the shape of the fracture surface and is caused by shear stress at the edges in the final stage of the crack. However, the cup and cone fracture surface is not typical for all metals. The shape and angle of the fracture surface is material dependent, for example, aluminium cracks develop at an angle of 45° to the applied force and exhibit a relatively smooth surface even at the edges. The micro-mechanism of the ductile fracture process can be seen in Fig. 1. [3], [6].

2.2 SIZE EFFECT

When the size of a material is reduced to a micro-scale, the workpiece often consists of only a few grains in the deformation zone, which causes the material to behave differently than macro-scale parts. This phenomenon is known as the size effect. It is an important phenomenon in micro-forming processes. The size effect impacts material properties, material deformation, fracture behavior, damage accumulation mechanism, and makes conventional models and methods no longer applicable in the analysis of micro-scale specimens. The size effect results from a considerable decrease in the number of grains in the deformation zone. Individual grain plays a more significant role in the deformation process. The material behaviour is affected not only by the grain size, but also by the orientation of each individual grain, their location, properties, and by the specimen size. There are two different types of size effects, called the grain size effect and the geometry size effect. The grain size effect occurs when the grain size of the material changes, while the specimen dimensions and its features remain the same. The geometry size effect is observed when the grain size of the material remains constant as the specimen size changes. [10], [11], [12], [13].

Fu et al. [12] conducted tensile tests on copper sheets and observed that fracture stress, fracture strain, and the number of micro-voids on the fracture surface decreased with decreasing thickness-to-grain-size ratio. Another study on thin metal sheets was carried out by Raulea et al. [14], who obtained similar results and reported that the yield strength and maximum strength of thin metal sheets decrease with decreasing number of grains over the thickness. Raulea et al. [14] also noticed that for grain sizes larger than the thickness of the specimen, the value of the yield strength appears to increase with increasing grain size. [11], [14].

In macro-forming processes, the ratio between surface grains and inner grains is extremely small, and the contribution of the surface grains to material properties can be neglected. However, as the sheet thickness decreases, the surface grains significantly influence the material properties. The decreasing flow stress with increasing miniaturization can be explained by a surface layer model. The surface grains are less restricted than the inner grains, leading to lower hardening and lower resistance against deformation and rotation, resulting in lower flow stress. It is also easier for micro-voids to coalesce and for cracks to grow throughout the thickness in micro-scaled materials. Based on the surface layer model, the flow stress of a material can be expressed as follows [10], [11], [13], [14], [15]

$$\sigma = \eta_s \cdot \sigma_s + (1 - \eta_s) \cdot \sigma_i, \quad (2.1)$$

where

$$\eta_s = \frac{N_s}{N_w}. \quad (2.2)$$

σ is the flow stress. N_w represents the number of grains in the whole material. σ_s and N_s denote the flow stress of surface grains and the number of surface grains, respectively. σ_i represents the flow stress of inner grains. η_s is the ratio of surface grains to total number of grains in the material. η_s is also known as a size factor. [15].

Wang et al. [15] performed various tensile and compression tests on specimens with different geometrical sizes and microstructures and reported that the stress triaxiality generally increases with the ratio of surface grains η_s under compression deformation. He also observed that at positive stress triaxiality, the fracture strain and energy are much lower than at negative stress triaxiality regardless of the specimen shape and grain size. [15].

Based on the surface layer model, Lai et al. [13] proposed a new constitutive model to express the material flow stress–strain relationship. In this model, the internal layer of the workpiece is treated as a polycrystalline material, whereas the surface grains are treated as a single crystal. Fig. 2 illustrates the ratio of surface to inner grains for macro and micro scaled materials. [10], [13], [15].

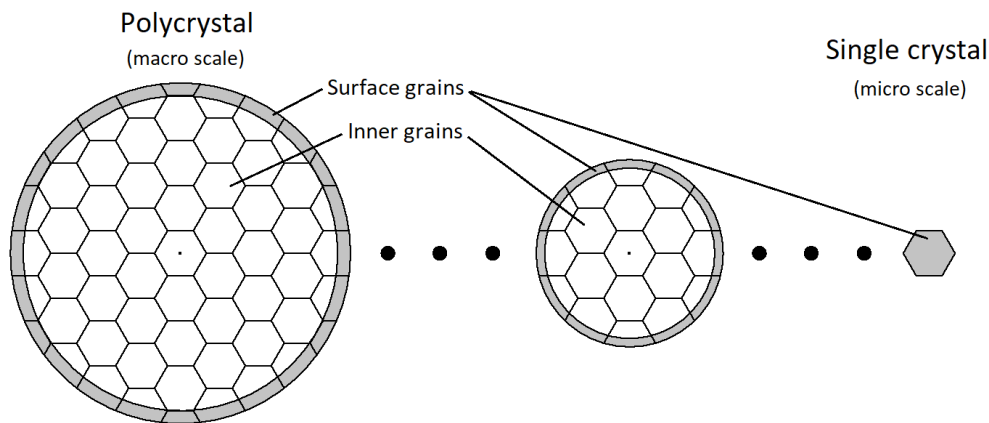


Fig. 2. Distribution of grains with decreasing geometrical size [13]

In the design process of the miniature specimens, the material was considered as an isotropic homogeneous solid without consideration of the size effect. The specimens were designed in the same way as when working with macroscopic samples. The main difference between fracture locus calibrated using macroscale samples and the proposed miniature samples is expected to be caused by the size effect, manufacturing imperfections, and residual stresses arising during the gripping process.

2.3 MINIATURE SPECIMEN TESTING METHODS

Miniature specimen testing methods can be used to characterize the mechanical properties of the material. Conventional macro-scale tests have been standardized to have specified dimensions and their ratios. However, the methods for testing miniature specimens have not yet been standardized, leading to different testing methods and specimen designs. [16], [17], [18].

There are many complications in the testing process of miniaturized specimens associated with specimen geometry, preparation methods, measuring devices, etc. Significant attention must be dedicated to surface preparation, which can affect the test results. In experimental testing, many experiments are often performed with samples of the same geometry, and the results are statistically evaluated for better reliability. Ductility is affected by the shape and size of the specimen features; hence, it is necessary to have geometrically identical samples in order to statistically evaluate the results and eliminate scatter in the data. This geometric similarity is more difficult to achieve with miniature specimens. The test results can also be affected by the size effect mentioned in the previous sub-chapter. This effect becomes more significant if the sample thickness is only 6–10 times larger than the average grain size. If the thickness is smaller than this, the test results no longer accurately reflect the properties of the bulk material. The small dimensions of these specimens do not allow the use of standard extensometers for strain measurement. Thus, non-contact type extensometers are used to measure the displacement. The non-contact extensometers include line scan cameras, laser interferometry, digital speckle pattern interferometry, digital

image correlation, etc. Another complication is associated with gripping. The specimens have a limited grip section and often require the development of special gripping devices. Common miniaturized testing methods can be categorized into tests based on scaling down the conventional specimen size (tensile, fatigue, impact, and fracture toughness tests), tests using disk sized specimens (disk bending tests, small punch tests), and ball indentation tests. [16], [18], [19].

The most commonly used testing method for miniaturized specimens to determine material properties is the uniaxial tensile test. Material properties obtained by the tensile tests include yield strength, ultimate tensile strength, and elongation. The specimens generally have a rectangular or cylindrical cross-section. The tensile testing process of miniaturized specimens is almost identical to the conventional one for macro samples. The difference is in gripping and displacement measurement. The tensile devices must also be able to ensure a very slow feed rate. The advantage of the tensile testing method is that it allows to achieve different stress states in the fracture initiation location by varying the geometry and features of the specimen, as it is utilized in this thesis. Uniaxial tension, plane strain, shear stress, etc. are examples of possible stress states that can be achieved. The specimen is gripped and driven at a constant speed until rupture. Force–displacement curves are obtained from the experiment. Miniature tensile specimens usually have a dog-bone shape that can be notched. A brief overview of possible sample geometries used in miniature tests is shown in Fig. 3. [19].

2D Digital Image Correlation (DIC) is only capable of measuring strains and displacement on the surface, hence it is mainly used for sheet metal testing. This is generally not an issue in tensile testing of miniature samples, as the specimens have mostly a flat dog-bone shape.

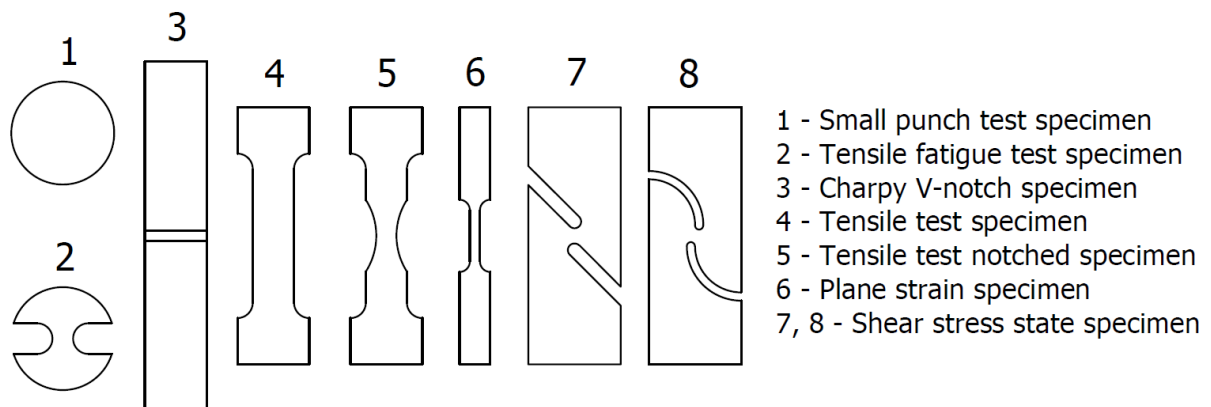


Fig. 3 Basic overview of flat miniature specimen geometries

Another common miniaturize testing method is called a Small Punch Test (SPT). It is a versatile testing technique used to determine the material behaviour of thin samples. This method was primarily developed to determine the mechanical properties of irradiated materials in nuclear power plants. It was later extended to investigate tensile, creep, fatigue, and fracture properties. It is a blanking operation in which a cylindrical pin shears through the centre of a small disk-type specimen clamped between a die and a holder at a constant speed. A similar stress–strain curve to the tensile test is obtained. They both contain an initial linear elastic region, a plastic region, a maximum strength, and exhibit a decrease in force until rupture. Although SPT and tensile tests provide similar material characteristics, they are not directly related. Empirical and analytical equations are used to establish

the relationship between the SPT and other conventional tests. This testing method is minimally affected by surface roughness. The SPT testing device is shown in Fig. 4. [17], [20], [21].

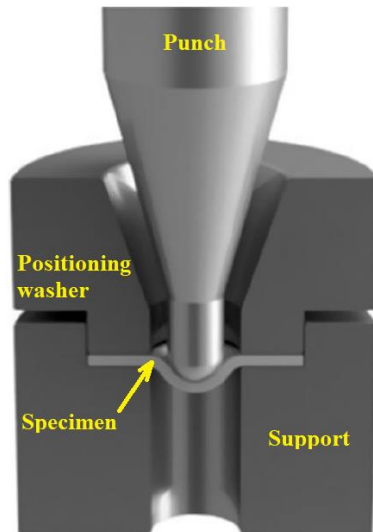


Fig. 4 SPT setup [20]

Fracture experiments can also be performed on butterfly specimens. Experiments with these specimens allow to capture a wide range of stress triaxialities and Lode parameters with only a single specimen geometry by varying the loading angle. The geometry along with different loading angles is shown in Fig. 5. The specimens have two shoulders connected by a narrow transition in the middle. The thickness at the transition location is reduced to concentrate the deformation to the centre of the sample. [22].

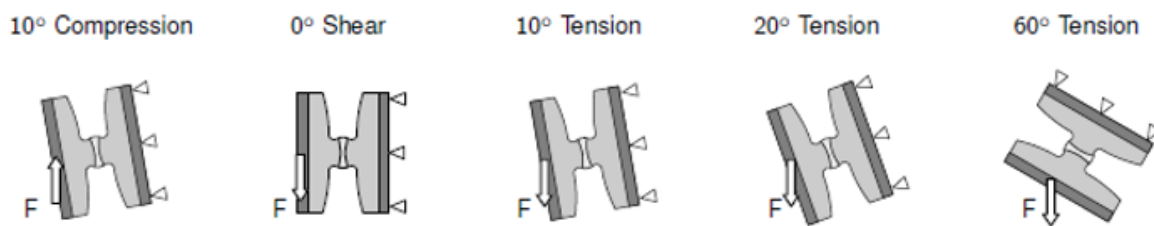


Fig. 5 Butterfly specimens [22]

3 STRESS STATE

3.1 STRESS AND STRAIN VARIABLES

To define the material models, such as plasticity or fracture criteria, it is necessary to introduce the below-mentioned parameters. The three-dimensional stress state of a material is defined by a Cauchy stress tensor, which is written as

$$\underline{\sigma} = \begin{bmatrix} \sigma_x & \tau_{xy} & \tau_{xz} \\ \tau_{xy} & \sigma_y & \tau_{yz} \\ \tau_{xz} & \tau_{yz} & \sigma_z \end{bmatrix}, \quad (3.1)$$

where σ and τ are normal and shear components of the stress tensor. The stress tensor consists of two components, the hydrostatic (mean) stress and the deviatoric stress. Principal stress coordinate system can be obtained by rotation of the coordinates. In the principal stress coordinate system, the shear stresses are set to zero, leaving only the diagonal components in the stress tensor. The characteristic equation of the Cauchy stress tensor is written as [23]

$$\sigma^3 - I_1\sigma^2 + I_2\sigma - I_3 = 0, \quad (3.2)$$

where I_1 , I_2 and I_3 are three invariants of the stress tensor. They are independent of the coordinate system. The invariants in the principal coordinate system are determined by the following equations. [23].

$$I_1 = \sigma_x + \sigma_y + \sigma_z \quad (3.3)$$

$$I_2 = \sigma_x\sigma_y + \sigma_x\sigma_z + \sigma_y\sigma_z \quad (3.4)$$

$$I_3 = \sigma_x\sigma_y\sigma_z \quad (3.5)$$

By solving the characteristic equation (3.2), three roots called the principal stresses $\sigma_I, \sigma_{II}, \sigma_{III}$ are obtained. These three principal stresses act on three mutually perpendicular surfaces. They can be ordered by magnitude, where $\sigma_1 > \sigma_2 > \sigma_3$. The plastic behavior of the material is generally considered to be independent of the hydrostatic stress component and is only affected by the deviatoric part of the stress tensor. The deviatoric stress tensor is obtained by subtracting the hydrostatic stress from the Cauchy stress tensor. The deviatoric stress tensor is expressed as [23], [24], [25]

$$\underline{S} = \begin{bmatrix} \sigma_x - \frac{1}{3}I_1 & \tau_{xy} & \tau_{xz} \\ \tau_{xy} & \sigma_y - \frac{1}{3}I_1 & \tau_{yz} \\ \tau_{xz} & \tau_{yz} & \sigma_z - \frac{1}{3}I_1 \end{bmatrix}. \quad (3.6)$$

The principal direction and the characteristic equation of the deviatoric stress tensor are obtained in a completely analogous way as in the previous process. It should be noted that the hydrostatic part of the Cauchy stress tensor is not affected by the rotation of the coordinate

system. The principal direction of the stress coincides with the principal direction of the deviatoric stress. The characteristic equation of the deviatoric stress tensor, which has three roots representing the principal deviatoric stresses S , is written as [25]

$$S^3 - J_1 S^2 - J_2 S - J_3 = 0. \quad (3.7)$$

The three invariants of the deviatoric stress tensor J_1 , J_2 and J_3 in the principal coordinate system are expressed as [25]

$$J_1 = S_1 + S_2 + S_3 = 0, \quad (3.8)$$

$$J_2 = -(S_1 S_2 + S_2 S_3 + S_3 S_1) = \frac{1}{2}(S_1^2 + S_2^2 + S_3^2), \quad (3.9)$$

$$J_3 = S_1 S_2 S_3, \quad (3.10)$$

where S_1 , S_2 and S_3 are diagonal parts of the deviatoric stress tensor in a principal coordinate system. Note that J_1 , which represents the sum of the normal stresses, is zero. The second principal invariant of the deviatoric stress tensor J_2 is used in many theories of plasticity including the von Mises theory of plasticity. This parameter is also useful in other fields like non-linear continuum mechanics. The second principal invariant of the deviatoric stress tensor is positive for all stress states and can also be expressed in terms of principal stresses as follows [25], [26]

$$J_2 = \frac{1}{6}[(\sigma_1 - \sigma_2)^2 + (\sigma_2 - \sigma_3)^2 + (\sigma_3 - \sigma_1)^2]. \quad (3.11)$$

The deviatoric invariants can be expressed using the invariants of the Cauchy stress tensor as [25]

$$J_2 = \frac{1}{3}(I_1^2 - 3I_2), \quad (3.12)$$

$$J_3 = \frac{1}{27}(2I_1^3 - 9I_1 I_2 + 27I_3). \quad (3.13)$$

It is necessary to introduce strain variables to calculate damage of a structure. Total strain can be decomposed into elastic and plastic parts, as written in Eq. (3.14). The material initially exhibits elastic behavior up to the yield stress.

$$\underline{\varepsilon} = \underline{\varepsilon}^e + \underline{\varepsilon}^p \quad (3.14)$$

$\underline{\varepsilon}^e$ and $\underline{\varepsilon}^p$ are elastic and plastic strain tensors, respectively. The elastic strain tensor is history independent, reversible and does not cause any permanent deformation. In the elastic zone, once the stress is removed, the elastic deformation disappears, and the material returns to its original shape. In contrast to plastic deformation, which is permanent and occurs when the material reaches yield stress. Plastic deformation is caused by a movement of dislocations. The stress-strain relationship is linear only for elastic deformations, which are expressed by a generalized Hooke's law in three mutually perpendicular directions as [27]

$$\varepsilon_x^e = \frac{1}{E}[\sigma_x - \mu_p(\sigma_y + \sigma_z)], \quad (3.15)$$

$$\varepsilon_y^e = \frac{1}{E} [\sigma_y - \mu_p(\sigma_x + \sigma_z)], \quad (3.16)$$

$$\varepsilon_z^e = \frac{1}{E} [\sigma_z - \mu_p(\sigma_x + \sigma_y)], \quad (3.17)$$

where ε_x^e , ε_y^e , ε_z^e are elastic strains of the elastic strain tensor. μ_p is Poisson's ratio and E represents the Young's modulus. The Young's modulus is a material constant that determines the slope of the stress–strain diagram in the elastic zone.

General stress–strain curve obtained from tensile test of ductile material is shown in Fig. 6. The proportional limit indicates a point up to which the stress is proportional to the strain. The proof stress is a stress required to produce 0.2 % of plastic strain. Deformation of the material during the tensile test is evenly distributed up to the ultimate stress, after which further deformations are concentrated in the necking zone. [27].

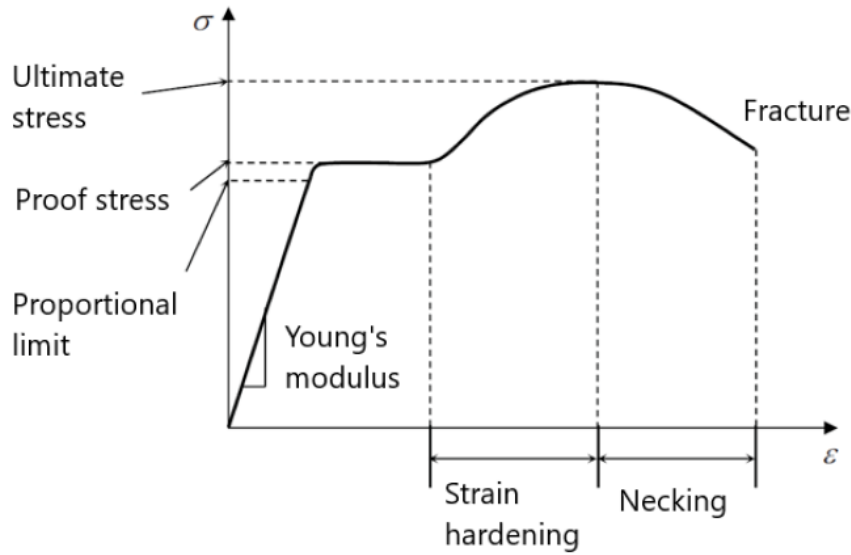


Fig. 6 General stress–strain diagram of ductile materials [27]

Plastic deformation does not exhibit a linear relationship between stress and strain and can only be calculated by integrating the stress rate over the past loading history. Incremental plastic strain must be calculated to determine the stress when the material is in the plastic zone. During plastic deformation, the material hardens. As a result of the material hardening, higher stress is required to induce further plastic deformations. [27].

The plastic strain tensor is composed of shape-changing (deviatoric) and volume-changing (volumetric) components. The deviatoric and volumetric strain matrixes are represented in a similar way to the stress tensor matrixes. The volumetric strain is expressed as a sum of diagonal elements of the plastic strain tensor. This operation is also called the trace of the matrix, written as $tr(\underline{\varepsilon}^p)$. The mean strain is calculated analogously to the mean stress of the Cauchy stress tensor as $\frac{1}{3}tr(\underline{\varepsilon}^p)$. The equation of the plastic strain tensor is formulated as [28]

$$\underline{\varepsilon}^p = \frac{1}{3}tr(\underline{\varepsilon}^p)\underline{I} + \underline{e}^p, \quad (3.18)$$

where $\underline{\varepsilon}^p$ is plastic strain tensor. \underline{I} is identity matrix and \underline{e}^p denotes deviatoric plastic strain tensor. When the material is considered incompressible, the volumetric part of the plastic strain tensor is zero ($tr(\underline{\varepsilon}^p) = 0$). The Eq. (3.18) then gives $\underline{\varepsilon}^p = \underline{e}^p$. [29].

Plastic deformation parameters are used in fracture models. The plastic deformation is caused by the movement of dislocations within the material. According to the ductile fracture criteria, a material fails when its ductility is exhausted, which occurs when the equivalent plastic strain reaches a critical value. The equivalent plastic strain accumulates during plastic flow. Since plastic deformation is an irreversible process, the value of the equivalent plastic strain can only increase throughout the process and is always positive. The equivalent plastic strain is expressed as an integral of the equivalent plastic strain rate over loading time. It is mathematically written as [30], [31]

$$\bar{\varepsilon}^p = \int_0^t \dot{\bar{\varepsilon}}^p dt, \quad (3.19)$$

where the equivalent plastic strain rate $\dot{\bar{\varepsilon}}^p$ is defined as follows [31]

$$\dot{\bar{\varepsilon}}^p = \sqrt{\frac{2}{3}(\underline{\dot{\varepsilon}}^p : \underline{\dot{\varepsilon}}^p)}. \quad (3.20)$$

$\underline{\dot{\varepsilon}}^p$ is plastic strain rate tensor. It is important to emphasize that this strain expression is valid only for an isotropic incompressible material with no volume change during plastic deformation. [32].

The critical value of the equivalent plastic strain $\bar{\varepsilon}^p$ at which the material fails is called fracture strain $\bar{\varepsilon}_f$. The value of the fracture strain depends on stress state parameters, such as stress triaxiality and normalized third invariant of the deviatoric stress tensor, which are defined in the subsequent sub-chapter. The fracture strain for a given material and loading path can be determined experimentally or estimated by numerical simulations that have implemented ductile fracture criteria. [30].

3.2 CHARACTERIZATION OF THE STRESS STATE

The stress state of an isotropic material can be geometrically represented in a three-dimensional principal stress space (illustrated in Fig. 7). Recall that the orientation of the principal stress space coordinates corresponds to the orientation where the shear stresses are zero. There are several coordinate systems in the principal stress space. The first is a Cartesian coordinate system with the principal stresses ($\sigma_I, \sigma_{II}, \sigma_{III}$) taken as axes. The second is a cylindrical coordinate system ($\sigma_m, \bar{\sigma}, \theta$), where the z-axis takes equal angles with respect to the principal stress axes. The third is a spherical coordinate system ($\bar{\sigma}, \eta, \theta$). [24], [33], [34], [35].

Lode coordinates can be constructed using three parameters p, q, r defined as [34]

$$p = -\sigma_m = -\frac{1}{3}tr(\underline{\sigma}) = -\frac{\sigma_1 + \sigma_2 + \sigma_3}{3}, \quad (3.21)$$

$$q = \bar{\sigma} = \sqrt{\frac{3}{2}\underline{s} : \underline{s}} = \sqrt{\frac{1}{2}[(\sigma_1 - \sigma_2)^2 + (\sigma_2 - \sigma_3)^2 + (\sigma_3 - \sigma_1)^2]}, \quad (3.22)$$

$$r = \left(\frac{9}{2} \underline{S} : \underline{S} : \underline{S} \right)^{\frac{1}{3}} = \left[\frac{27}{2} \det(\underline{S}) \right]^{\frac{1}{3}} = \left[\frac{27}{2} (\sigma_1 - \sigma_m)(\sigma_2 - \sigma_m)(\sigma_3 - \sigma_m) \right]^{\frac{1}{3}}. \quad (3.23)$$

The mean stress σ_m is positive in tension, while the parameter p is positive in compression. \underline{S} is the deviatoric stress tensor. [33].

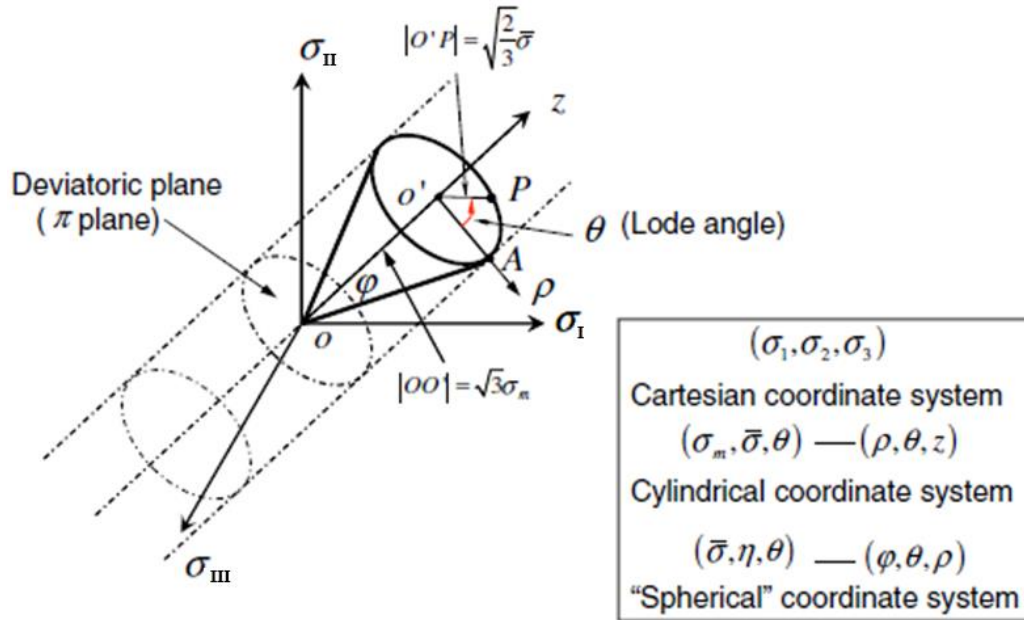


Fig. 7 Haigh–Westergaard stress space [33]

Each point on the z -axis in Fig. 7 corresponds to a hydrostatic stress state. If the loading is purely hydrostatic, the loading path travels along the z -axis, where $\sigma_1 = \sigma_2 = \sigma_3$ and the magnitude is equal to the mean stress σ_m . The hydrostatic part of the stress state is represented by a parameter p . The distance between a point representing the current stress state and the hydrostatic axis in a plane perpendicular to the hydrostatic axis is related to parameter q . [24], [35].

When working with fracture models, it is necessary to introduce stress triaxiality η . Stress triaxiality is a dimensionless pressure dependence parameter that is considered to be a key parameter controlling the fracture strain of a material. It can be expressed as a ratio of hydrostatic stress to von Mises equivalent stress. [34].

$$\eta = \frac{-p}{\bar{\sigma}} = \frac{\sigma_m}{\bar{\sigma}} = \frac{\sqrt{2}}{3} \cotan \varphi, \quad (3.24)$$

where $\bar{\sigma}$ denotes equivalent stress. The range of stress triaxiality is $-\infty \leq \eta \leq \infty$. φ is coordinate in the spherical coordinate system in Fig. 7. There are an infinite number of stress states for a given stress triaxiality. Each stress state corresponds to a point on the surface of the cone in the Haigh–Westergaard space. Therefore, it is important to introduce an additional parameter to distinguish these different stress states. The parameter is called Lode angle θ . The Lode angle can be expressed through normalized third invariant of the deviatoric stress tensor as follows [1], [29], [33], [35], [36]

$$\cos(3\theta) = \xi = \left(\frac{r}{q}\right)^3 = \frac{27}{2} \frac{J_3}{\bar{\sigma}^3}. \quad (3.25)$$

The Lode angle ranges $0 \leq \theta \leq \pi/3$. The range of the normalized third invariant of the deviatoric stress tensor is $-1 \leq \xi \leq 1$. The Lode angle can be normalized to range $-1 \leq \bar{\theta} \leq 1$ by using the following equation. [34].

$$\bar{\theta} = 1 - \frac{6}{\pi} \theta = 1 - \frac{2}{\pi} \arccos(\xi) \quad (3.26)$$

$\bar{\theta} = 1$ corresponds to axisymmetric tension. $\bar{\theta} = 0$ corresponds to generalized shear or plane strain and $\bar{\theta} = -1$ represents axisymmetric compression or equi-biaxial tension. If the material undergoes a combined multiaxial stress state, $\bar{\theta}$ varies between the above-mentioned values. In some literature, the Lode angle is substituted by Azimuth angle θ_A to describe the Lode dependence. The relationship between the Lode angle and the Azimuth angle is formulated as follows [1], [33], [34]

$$\bar{\theta} = -\frac{6}{\pi} \theta_A, \quad (3.27)$$

$$\theta = \theta_A + \frac{\pi}{6}. \quad (3.28)$$

Azimuth angle ranges $-\pi/6 \leq \theta_A \leq \pi/6$. Plane stress condition relates the parameters η , ξ and $\bar{\theta}$ as follows [37]

$$\xi = \cos\left[\frac{\pi}{2}(1 - \bar{\theta})\right] = -\frac{27}{2} \eta \left(\eta^2 - \frac{1}{3}\right). \quad (3.29)$$

The values of stress triaxiality and normalized Lode angle of conventional specimens used for fracture criteria calibration are given in Table 1.

The Lode angle dependence can also be described by Lode parameter μ . The Lode parameter ranges $-1 \leq \mu \leq 1$ and characterizes the position of σ_2 in relation to σ_1 and σ_3 . Note that $\mu = -1$ when $\sigma_1 > \sigma_2 = \sigma_3$, $\mu = 0$ when $\sigma_2 = (\sigma_1 + \sigma_3)/2$ and $\mu = 1$ when $\sigma_1 = \sigma_2 > \sigma_3$. It distinguishes the stress state between tension, shear, and compression. The Lode parameter is expressed as [22], [29], [35]

$$\mu = \frac{2\sigma_2 - \sigma_1 - \sigma_3}{\sigma_1 - \sigma_3}. \quad (3.30)$$

The relationship between the Lode parameter and the Lode angle is given as [36]

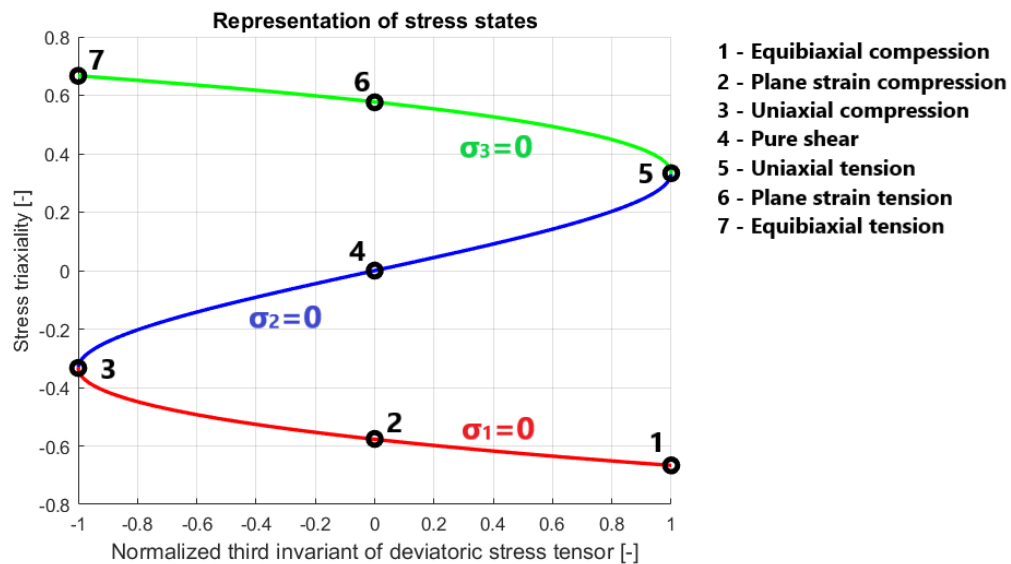
$$\tan(\theta) = \frac{\sqrt{3}(\mu + 1)}{3 - \mu}. \quad (3.31)$$

The representation of various stress states in the plane of stress triaxiality and normalized third invariant of the deviatoric stress tensor is shown in Fig. 8.

Table 1 η and ξ values of typical specimens used for fracture criteria calibration [38]

Specimen type	Analytical expression for stress triaxiality	Normalized third invariant of deviatoric stress tensor
Smooth round bars, tension	$\frac{1}{3}$	1
Notched round bars, tension	$\frac{1}{3} + \sqrt{2} \ln\left(1 + \frac{a}{2R}\right)$	1
Plane strain, tension	$\frac{\sqrt{3}}{3}$	0
Flat grooved plates, tension	$\frac{\sqrt{3}}{3} \left[1 + 2 \ln\left(1 + \frac{t}{4R}\right)\right]$	0
Torsion or shear	0	0
Cylinders, compression	$-\frac{1}{3}$	-1
Equi-biaxial plane stress tension	$\frac{2}{3}$	-1
Equi-biaxial plane stress compression	$-\frac{2}{3}$	1
Plane strain, compression	$-\frac{\sqrt{3}}{3}$	0
Notched round bars, compression	$-\left[\frac{1}{3} + \sqrt{2} \ln\left(1 + \frac{a}{2R}\right)\right]$	-1

*In the analytical expressions of stress triaxiality, R is the radius of a notch or a groove, a is the radius of a round bar at the notch, t is the thickness of a flat grooved plate at the groove. [38].

Fig. 8 Representation of various stress states in the plane of η and ξ [36]

The relationship between parameters η , μ , $\bar{\sigma}$ and principal stresses $(\sigma_1, \sigma_2, \sigma_3)$, can be formulated by the following equations. [39].

$$\sigma_1 = \left(\eta + \frac{(3 - \mu)}{3\sqrt{\mu^2 + 3}} \right) \bar{\sigma} \quad (3.32)$$

$$\sigma_2 = \left(\eta + \frac{2\mu}{3\sqrt{\mu^2 + 3}} \right) \bar{\sigma} \quad (3.33)$$

$$\sigma_3 = \left(\eta + \frac{(3 + \mu)}{3\sqrt{\mu^2 + 3}} \right) \bar{\sigma} \quad (3.34)$$

The dependence of μ and η for plane stress can be obtained by setting one of the principal stresses to zero. [39].

The dependence of normalized third invariant of deviatoric stress tensor, normalized Lode angle, Azimuth angle and Lode parameter on stress triaxiality is plotted in Fig. 9.

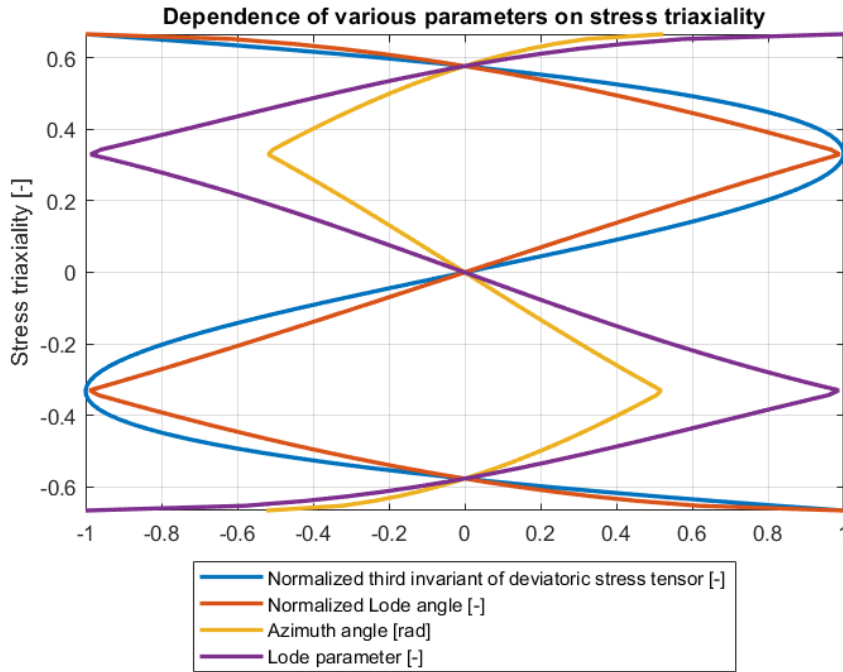


Fig. 9 Dependence of ξ , $\bar{\theta}$, θ_A , μ parameters on stress triaxiality η for plane stress

3.3 GEOMETRICAL REPRESENTATION OF THE STRESS STATE

A general stress state, represented in the Haigh–Westergaard space (Fig. 7) by the vector \overrightarrow{OP} , can be decomposed into a hydrostatic $\overrightarrow{OO'}$ and a deviatoric $\overrightarrow{O'P}$ component. The hydrostatic part is perpendicular to the deviatoric plane, and the deviatoric part lies in the deviatoric plane. The deviatoric plane is any plane perpendicular to the hydrostatic axis (z-axis), where all the principal stresses are equal ($\sigma_I = \sigma_{II} = \sigma_{III}$). Deviatoric plane passing through the origin is called π -plane. The magnitudes of the vectors $\overrightarrow{OO'}$ and $\overrightarrow{O'P}$ are linearly related to the hydrostatic and equivalent stress, respectively, and are expressed as follows [22], [30], [39]

$$|\overrightarrow{OO'}| = \frac{\sqrt{3}}{3} I_1 = \sqrt{3} \sigma_m, \quad (3.35)$$

$$|\overrightarrow{O'P}| = \sqrt{2J_2} = \sqrt{\frac{2}{3}} \bar{\sigma}. \quad (3.36)$$

Projection of the deviatoric principal stress onto the deviatoric (octahedral) plane is plotted in Fig. 10. The vectors in Fig. 10 are expressed as [1], [22]

$$|\overrightarrow{O'L}| = \sqrt{\frac{3}{2}} s_1, \quad (3.37)$$

$$|\overrightarrow{O'M}| = \sqrt{\frac{3}{2}} s_2, \quad (3.38)$$

$$|\overrightarrow{O'N}| = \sqrt{\frac{3}{2}} s_3. \quad (3.39)$$

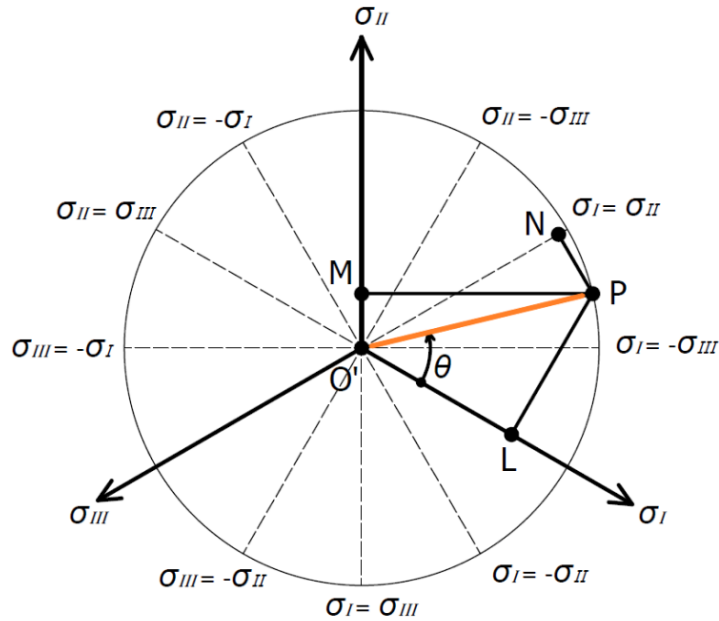


Fig. 10 Geometrical representation of the deviatoric stress in the deviatoric plane

The Lode angle is an angle between the deviatoric projection of the principal axis and the projection of stress tensor into the deviatoric plane as shown in Fig. 10. [22], [36].

The planes parallel to the π -plane contain six segments in which the ordering of the principal stresses is different. The contours in these planes for an isotropic material have the same shape in each of the segments. The advantage of this property is that only one segment shape needs to be calculated to model the surface of any yield criterion. Other segments are obtained by reflection around the stress axes. [30].

4 SIMPLE OVERVIEW OF MATERIAL MODELLING

4.1 NUMERICAL SIMULATIONS

Numerical simulations can be used to predict material behaviour and evolution of crack propagation. To do so, dynamic explicit codes must be employed, as implicit codes are unable to simulate crack propagation due to a convergence issue. There are many material models that need to be calibrated and implemented into the software to predict crack propagation. Model of elasticity, plasticity model, ductile fracture criteria and damage evolution rules are examples of such models. In order to validate these criteria to predict crack formation, it is necessary to perform experimental calibration tests. Although the results obtained from properly calibrated numerical simulations can predict crack formation, it is recommended to verify the numerical simulations using experiments for better reliability. [29], [38].

The first step in the numerical simulation process is to determine the behaviour of the material. Model of elasticity utilized to predict the material behavior in the initial elastic zone can be isotropic, orthotropic, or anisotropic. Then a constitutive (hardening) law, which describes the relationship between stress and plastic strain must be defined. The hardening law can be isotropic, kinematic, or combined. It describes the behaviour of a yield surface expressed by a yield criterion, which is another material model that needs to be implemented into the software. It is necessary to describe the direction of plastic strain increment defined by the flow rule, which can be associated or non-associated. [29], [40].

Models dealing with damage accumulation and crack propagation must also be employed. Ductile fracture criteria form an envelope that defines the fracture strain for each individual stress state. Various ductile fracture criteria have been developed over the years. The first criteria were dependent on the first principal stress. Recent ductile fracture criteria are dependent on stress triaxiality and normalized third invariant of the deviatoric stress tensor. It is important to address the non-proportional loading during the testing process. To do so, damage evolution rules are implemented into the numerical simulations to extend the fracture models for non-proportional loading paths. The damage evolution rules are using a damage parameter that represents the amount of damage done to a material. The value of the damage parameter increases with increasing equivalent plastic strain. The relationship between the damage parameter and the equivalent plastic strain can be linear or non-linear. When the damage parameter reaches a critical value, a material failure is declared. Once the material failure is declared, the mesh is adjusted to reflect the crack formation. There are several possible methods to model the crack propagation in FEM, such as cohesive zone insertion, extended finite element method or element deletion technique, which is the most common one due to its easy implementation. The element deletion technique reduces the stress in the critical elements to zero by setting the strength and stiffness to a very low value. The element deletion technique was also used in this thesis to model crack propagation. The flowchart of numerical ductile fracture simulation is shown in Fig. 11. [29], [30], [36].

The mentioned material models contain material parameters that must be calibrated by experimental tests. The elastic material parameters can be obtained by tensile test, indentation test, or ultrasonic impulse method based on the speed of ultrasonic wave propagation through the material. The hardening parameters are calibrated by approximating

the stress–plastic strain curve given by tensile tests using a hardening equation, such as Swift hardening law, Ramberg–Osgood hardening law, etc. The calibration can be done by an inverse trial and error parameter determination procedure by which the experimentally obtained stress–strain curve is fitted. However, this is not the only way to obtain the material parameters of the hardening law. There are many variations of more sophisticated inverse optimization methods or analytical and numerical computational methods. [38], [41], [42], [43].

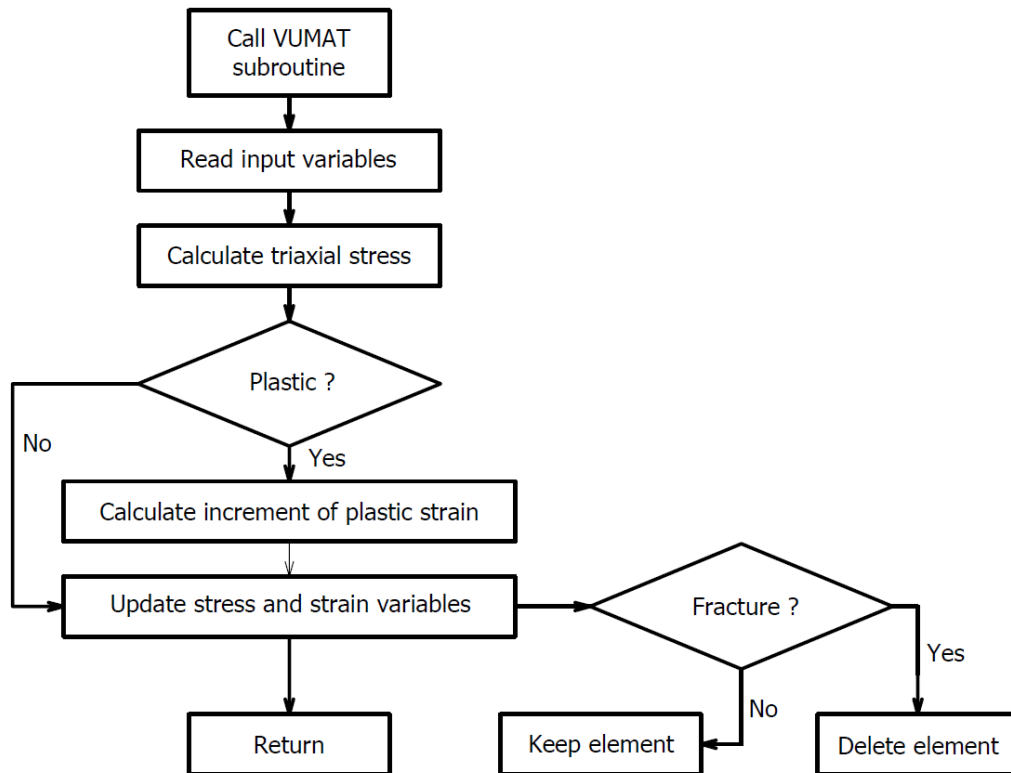


Fig. 11 Flowchart of the ductile fracture simulation process [36]

To calibrate the fracture criteria, it is necessary to have samples capturing various stress states. The fracture model is generally calibrated by a hybrid experimental and numerical method. A wide range of stress states can be obtained by performing experiments covering uniaxial tension, plane strain, compression, shear stress state, etc. The specimens with these specific stress states are designed using numerical simulations. The average values of stress triaxiality and normalized third invariant of the deviatoric stress tensor are extracted from a predicted fracture initiation point. The fracture envelope is dependent on the stress triaxiality and normalized third invariant of the deviatoric stress tensor (or Lode parameter) and can be displayed in three-dimensional space with η , ξ and equivalent plastic strain $\bar{\epsilon}_p$ taken as axes. The envelope is obtained by approximating the experimental points using the fracture criterion formulation. The fitting can be done by the trial-and-error method or by minimizing the relative error function, for example by using the least squares method, particle swarm optimization, bee swarm optimization, etc. [36], [43].

Another approach to determine the material parameters of the fracture models consists of using machine learning assistance. This approach enables to identify values of material parameters without extracting the stress state evolution from numerical simulations of calibration samples. The stress state parameters can also be determined from experiments; however, this approach is difficult to carry out. Therefore, the numerically determined stress

state is preferred and is considered a general approach. The results of the experimental-numerical method can be affected by an incorrectly selected fracture element, which may vary depending on the material models used. It also requires performing a numerical simulation of each individual specimen involved in the calibration process. These calculations can be time consuming, as the mesh in the fracture region must be fine. The neural network method uses a set of parameters that are extracted from the force–displacement response as input to the training model. It can be trained based on force–displacement measurements of a single sample, although the accuracy increases with increasing number of specimens used in the training data set. It simplifies the calibration process by replacing damage evolution and fracture model calibration with a neural network. It should be noted that currently the neural network calibration is not superior and has approximately the same accuracy as the conventional calibration method. Models with a large number of material parameters present a challenge for the machine learning technique. [44].

4.2 PLASTICITY

Plasticity is associated with formation of permanent deformations. For most ductile materials, the plastic strain at the moment of fracture is much greater than the elastic strain. When the material is under stress, it starts to deform. Initially, the deformation is elastic, but after reaching a threshold value, which is given by yield stress (illustrated in Fig. 6), the deformation becomes permanent, and the stress–strain relationship is no longer linear. For that reason, a new constitutive equation must be used to describe the behaviour of the material, as Hooke’s law is no longer applicable for plastic deformations. One of the theories used to describe the plastic behaviour of materials is called the deformation theory of plasticity. It is an older theory that is consistent with experiments only in the case of monotonic proportional loading and does not respect the loading history. Later, a more sophisticated theory of plasticity, called the incremental plasticity theory was developed. The loading history affects the mechanical properties of a material that is plastically deformed. Therefore, the incremental theory of plasticity is formulated in an incremental fashion to describe the plastic behaviour of materials. The incremental plasticity theory consists of three main components, which are the yield criterion, a flow rule, and a hardening rule. [30], [45], [46], [47].

4.2.1 YIELD CRITERIA

A yield criterion forms a surface in the stress space that encloses a region where the material behaviour is elastic. When the current stress state is at the surface, the deformation is plastic. It should be noted that the current stress state cannot exceed the yield envelope. It drags it in the case of kinematic hardening or inflates it in the case of isotropic hardening. In the classical metal plasticity theory, the surface of the yield criteria are aligned parallel to the hydrostatic axis in the principal stress space. It was believed that yielding of metals is insensitive to mean hydrostatic stress. The influence of hydrostatic pressure was neglected in the classical von Mises theory, and it was assumed that the flow stress is independent of the third invariant of the stress deviator. However, recent experiments have shown that the constitutive description of the material should take into account the effect of pressure as well as the effect of the third deviatoric stress invariant (or Lode angle parameter). There are many yield criteria, the most used ones for ductile materials are the Tresca theory (maximum shear stress theory) and the von Mises theory (distortion energy theory). They differ in the shape of the yield surface and in the equation for the equivalent stress. The yield condition is generally expressed as [30], [38], [47], [48]

$$f(\underline{\sigma}, \sigma_y(\bar{\varepsilon}^p)) = \bar{\sigma} - \sigma_y(\bar{\varepsilon}^p) = 0, \quad (4.1)$$

where f represents a yield function, which can be visualized in Haigh–Westergaard stress space as an envelope. σ_y is current yield stress. The value of yield stress σ_y changes once the equivalent stress exceeds initial yield stress. [47].

4.2.2 FLOW RULES

The flow rule expresses the relationship between the plastic strain increment and the actual stress and its stress increment during plastic flow. The flow rule is generally written as [30]

$$d\underline{\varepsilon}^p = d\lambda \frac{\partial Q}{\partial \underline{\sigma}}, \quad (4.2)$$

where $d\underline{\varepsilon}^p$ is plastic strain tensor increment. $d\lambda$ is equivalent plastic strain increment (also known as plastic multiplier increment) and Q is plastic potential. If $Q = f$, then the flow rule is called associated. The partial derivative $\partial f / \partial \underline{\sigma}$ is a vector in Haigh–Westergaard space whose normal is perpendicular to the yield surface. This means that the plastic strain increment is perpendicular to the yield surface in contrast to the stress increment, whose direction is perpendicular to the yield surface and coincides with the plastic strain increment only in elastic deformations. This satisfies the condition of incompressibility of the material during plastic deformation. Stress and plastic strain increment of the associated flow rule is shown in Fig. 12. [38], [47].

In the case of the non-associated flow rule, the plastic potential is not equal to the yield function. The non-associated flow rule uses two separate functions for the yield and plastic potential. This approach allows the elastic limit and the plastic strain rate direction to be described independently, enabling a more accurate prediction of material behaviour, and increasing the agreement between simulations and experiments. [49].

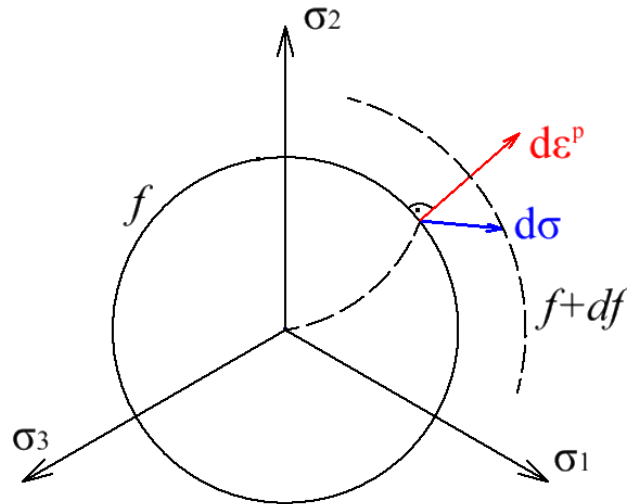


Fig. 12 Representation of the stress and strain increment of the associated flow rule

4.2.3 HARDENING RULES

The hardening rule describes the behaviour of the yield surface during plastic deformation. Hardening is characterized by the steepness of the stress–strain diagram during plastic

deformations. The resistance of the material with increasing stress can be smaller (in the case of material weakening), or greater in the case of material hardening. The current stress state during plastic deformation remains on the yield surface, so that the elastic zone is immediately available after unloading. The hardening rules can be classified into the following four categories: isotropic, kinematic, combined, and anisotropic. [30], [40], [47].

In the case of isotropic hardening, the size of the instantaneous yield condition represented by the cylinder radius (Fig. 13) expands evenly in all directions when the elastic threshold is reached. The origin of the cylinder remains the same during the loading process. The isotropic hardening is commonly used for monotonic loading but is unable to describe phenomena such as the Bauschinger effect. Hence, this model is not suitable for cycling loading. [40], [47], [50].

The kinematic hardening law is mostly utilized in the case of a cycling loading study. The size of the initial yield surface remains the same, but the elastic threshold translates as shown in Fig. 13. The yield surface remains parallel to the octahedral plane. [47], [50].

The combined hardening rule uses both isotropic and kinematic hardening models and is capable of simulating cyclic hardening and softening, which would not be possible by using only one of the above-mentioned hardening models. Both the combined and the kinematic models are capable of describing the Bauschinger effect. [40].

In metals that deform plastically, the mechanical response depends not only on their current stress state but also on the history of deformation; this phenomenon is captured by the Bauschinger effect. In 1881, J. Bauschinger published a paper comparing the kinematic and the isotropic models with experimental results. In this paper, the specimens were loaded in tension beyond elastic deformation and subsequently loaded in the reverse direction. He observed that after loading in the reverse direction, the plastic deformation began at a lower stress than predicted by the isotropic model. The kinematic model reflected the experiments more accurately. This phenomenon occurs in most polycrystalline metals. The hysteresis loop predicted by the isotropic hardening (dashed line) and the loop presented by Bauschinger (continuous line) is plotted in Fig. 14. [45], [47].

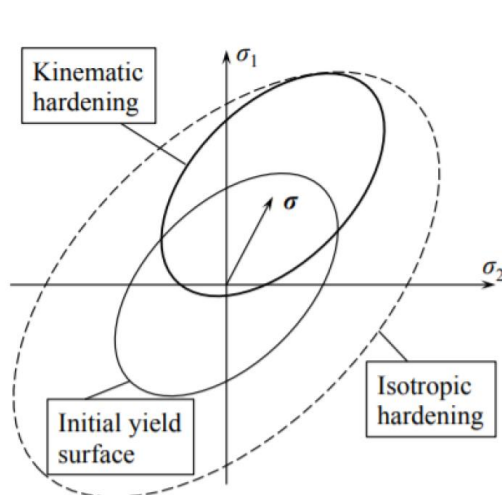


Fig. 13 Kinematic and isotropic hardening [50]

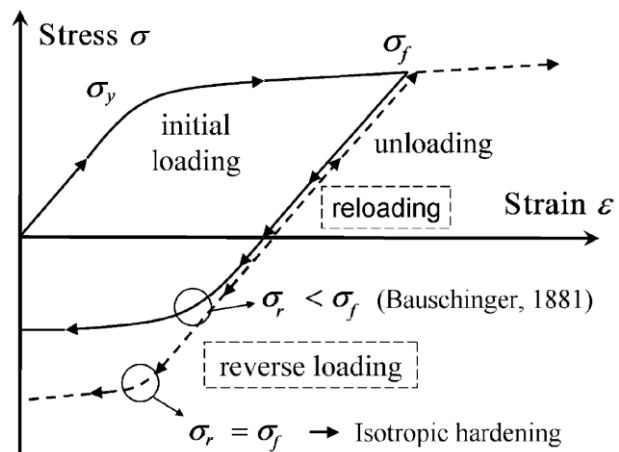


Fig. 14 Bauschinger effect [51]

4.3 DAMAGE PARAMETER

Because the damaging process depends on the loading history, it is necessary to introduce a damage variable that considers this phenomenon. Many models do not include this variable in their equations; therefore, a separate damage variable must be used to count towards the fracture initiation. [1], [52].

The calculation methods of the damaging process can be divided into coupled and uncoupled categories. The uncoupled methods assume that the damage of the structure does not influence material properties, in other words, the constitutive equations are not coupled with the damage parameter. The uncoupled constitutive equations lead to stress and strain errors and incorrectly predict fracture modes due to insufficient damage-induced weakening and unrealistic strengthening in the later stage of plastic deformation. They also model fracture as a sudden drop in the stress–strain curve due to a decrease in material stiffness. However, in reality, damage within the solid is caused by cavities that affect both the stress and strain distribution, and the material exhibits continuous degradation. For the most accurate prediction of material failure, it is recommended to use coupled constitutive equations in which the damage is associated with the material strength. [1], [53], [54].

In ductile materials, rupture is caused by nucleation, coalescence, and growth of voids induced by plastic deformation. Based on this theory, Kachanov [55] proposed a continuum damage variable that represents the surface density of the voids. Later, a complementary theory to fracture mechanics was formulated which describes the evolution of this variable and its influence on the mechanical properties of the material, such as the elastic modulus. This theory is called continuum damage mechanics (CDM). This approach enables to approximate macro-scale damage using a micro-mechanic's damage variable, allowing the use of conventional specimen testing methods to measure the average degradation of the material. A common feature of CDM is averaging the effect of damage over a volume of material. The damage variable can be evaluated by a strain equivalence principle or by energy equivalence principle. Damaging process is associated with a progressive deterioration of the material, which can be measured by a decrease in strength, stiffness, toughness, etc. [54], [56], [57].

In the model introduced by Kachanov [55], the damage variable D represents a reduction of effective resisting area due to a presence of voids within the material. The damage variable, assuming isotropic deterioration of the material, is expressed as [54], [56]

$$D = 1 - \frac{\tilde{A}}{A}, \quad (4.3)$$

where \tilde{A} and A are an effective resisting area and the original cross-sectional resisting area, respectively. The damage parameter takes values from 0 to 1. $D = 0$ when the material is undamaged, the material fails when the damage parameter reaches a critical value $D = 1$. [54], [56].

In the strain equivalence hypothesis, the damaged material has a similar constitutive behaviour to the undamaged virgin material. Under this assumption, the stress is replaced by an effective stress $\tilde{\sigma}$, which is given as follows [54], [56]

$$\tilde{\sigma} = \sigma \frac{A}{\tilde{A}} = \frac{\sigma}{1 - D}. \quad (4.4)$$

The damage variable can also be expressed through degradation of the elastic modulus using the following equation. [54].

$$D = 1 - \frac{\tilde{E}}{E} \quad (4.5)$$

Where \tilde{E} is the effective Young's elastic modulus of a damaged material. This allows to indirectly measure damage of a solid by monitoring the evolution of the Young's modulus with increasing strain. Young's modulus has been observed to decrease with increasing damage. There are many other expressions of the damage variable, although it has been experimentally shown that the most convenient way to calculate damage is by monitoring the evolution of the elastic modulus. [53], [54], [56].

In uncoupled plasticity models, the damage is calculated as an integral of a weighing function with respect to the equivalent plastic strain. The damage is then incorporated into the yield function. Relationship between the damage parameter and the equivalent plastic strain can be linear or non-linear. The linear dependence works well for monotonic loading paths, however, for more complex loading paths, a nonlinear dependence should be used instead. The cumulative damage model is written as [1], [33], [36]

$$D(\bar{\varepsilon}_p) = \int_0^{\bar{\varepsilon}_f} \frac{d\bar{\varepsilon}_p}{f(\eta, \xi)}. \quad (4.6)$$

The weighing function $f(\eta, \xi)$ determines the damage accumulation rate at the current combination of damage and stress state. $\bar{\varepsilon}_f$ is the equivalent fracture strain, which can be directly determined by an optical measurement system during an experiment carried out to fracture or by numerical simulations. Stress triaxiality and normalized third invariant of the deviatoric stress tensor are functions of the equivalent plastic strain. These two functions (η, ξ) are determined by numerical simulations. Their values are averaged throughout the loading process. The average values are calculated using the following equations. [1], [33], [38].

$$\eta_{av} = \frac{1}{\bar{\varepsilon}_f} \int_0^{\bar{\varepsilon}_f} \eta(\bar{\varepsilon}_p) d\bar{\varepsilon}_p \quad (4.7)$$

$$\xi_{av} = \frac{1}{\bar{\varepsilon}_f} \int_0^{\bar{\varepsilon}_f} \xi(\bar{\varepsilon}_p) d\bar{\varepsilon}_p \quad (4.8)$$

The parameters are averaged because the stress state is constantly evolving during plastic deformation. The fracture locus, which is constructed using an average values of η and ξ is utilized as a reference envelope even for more complex loading paths. Although the coupled criteria are more accurate, the results provided by the uncoupled approach are satisfactory enough for most engineering problems. The uncoupled approach, including averaging η and ξ , was used for the fracture prediction in this thesis. [38], [44].

4.4 FRACTURE MODELS

The objective of a fracture model is to predict rupture of a workpiece. The fracture criteria form a 3D fracture envelope in the space of stress triaxiality, normalized third invariant of the deviatoric stress tensor and equivalent plastic strain, under which the damage

is accumulated for a given loading path. The onset of the fracture is predicted when the loading path intersects the fracture envelope (when the damage parameter reaches its critical value). The criteria are also able to simulate the crack propagation path when implemented in the FEM. The calibration of ductile fracture criteria requires several samples covering a wide range of stress states. Points characterized by the strain and stress parameters η_{av} , ξ_{av} and $\bar{\epsilon}_f$ are then fitted by a function of the fracture criterion to obtain an envelope that bounds a region under which the fracture should not occur. Most criteria also specify a cut-off area beyond which no damage is accumulated. The cut-off surface is generally defined for lower or negative stress triaxiality. [33], [58], [59].

As mentioned in the previous sub-chapter, the phenomenological criteria can be divided into uncoupled and coupled, allowing the yield surface of the material to be modified by a damage-induced density change. Although the coupled criteria predict the onset of fracture more accurately, the uncoupled phenomenological models are still preferred for industrial applications due to simplicity and fewer material constants that must be calibrated. [36], [60].

One of the first ductile fracture criterion was proposed by Cockroft and Latham [61]. It was based on the observation that the ductile fracture tends to occur in the area of maximum tensile stress. The fracture in the criterion is governed by the maximum principal stress integrated over the plastic strain path and is expressed as follows [36], [62]

$$\int_0^{\bar{\epsilon}_f} \sigma_1 d\bar{\epsilon}_p = C_{c-L}. \quad (4.9)$$

Rice and Tracey [63] analysed void growth and proposed a criterion dependent on the stress triaxiality as [62]

$$\int_0^{\bar{\epsilon}_f} 0,283e^{\left(\frac{3}{2}\eta\right)} d\bar{\epsilon}_p = C_{R-T}. \quad (4.10)$$

Brozzo et al. [64] modified the Cockroft and Latham [61] criterion to consider the effect of mean stress on the equivalent plastic strain to fracture. The criterion is formulated as follows [62]

$$\int_0^{\bar{\epsilon}_f} \frac{2\sigma_1}{3(\sigma_1 - \sigma_m)} d\bar{\epsilon}_p = C_B. \quad (4.11)$$

Another modification of the Cockroft and Latham [61] criterion was done by Oh et al. [65]. The criterion is dimensionless and is expressed as [36]

$$\int_0^{\bar{\epsilon}_f} \frac{\sigma_1}{\bar{\sigma}} d\bar{\epsilon}_p = C_{Oh}. \quad (4.12)$$

Criterion proposed by Ko-Huh et al. [66] is expressed as follows [36]

$$\int_0^{\bar{\epsilon}_f} \frac{\sigma_1}{\bar{\sigma}} (1 + 3\eta) d\bar{\epsilon}_p = C_{K-H}. \quad (4.13)$$

C are material constants (critical values). Fracture occurs when the material reaches a critical value of C . Later, more sophisticated and complex criteria were introduced, such as the one proposed by Bai and Wierzbicki, which is given as [38]

$$\bar{\varepsilon}_f = \left[\frac{1}{2} (D_1 e^{-D_2 \eta} + D_5 e^{-D_6 \eta}) - D_3 e^{-D_4 \eta} \right] \bar{\theta}^2 \quad (4.14)$$

$$+ \frac{1}{2} (D_1 e^{-D_2 \eta} - D_5 e^{-D_6 \eta}) \bar{\theta} + D_3 e^{-D_4 \eta}.$$

D_1, \dots, D_6 are material constants. Examples of other ductile fracture criteria are modified Mohr–Coulomb, Ganjiani, Lou–Huh, and KHPS2, which are described in more detail later in the thesis.

5 MATERIAL MODELS

5.1 MODEL OF ELASTICITY

The material behaviour in the elastic deformation zone was modelled by Hooke's law. The material was considered isotropic. The elastic material parameters of the aluminium alloy 2024-T351 are specified in the following table.

Table 2 Elastic material parameters and density [67]

Young's modulus E [MPa]	Poisson's ratio μ_p [-]	Density ρ [kg·m ⁻³]
72500	0.34	2770

The material characteristics listed in Table 2 were provided by the supervisor along with the calibrated constitutive law and plasticity model. They were not experimentally investigated in this work. The elastic and constitutive law material parameters can also be found in the literature [67] and [29], where the properties of the same bulk material from which the samples were manufactured have been investigated in detail. The density was calculated using equation $\rho = M/V$, where M is the weight of the material and V is the volume. Young's modulus was estimated by a uniaxial tensile test. The Poisson's ratio μ_p has been calculated as a function of Young's modulus E , density ρ and wave velocity v . The wave velocity was measured using an ultrasonic thickness gauge OLYMPUS 38DL PLUS with a 5 MHz contact transducer M110. The equation by which the Poisson's ratio was calculated is given as follows [29]

$$v = \sqrt{\frac{E}{\rho} \cdot \frac{(1 - \mu_p)}{(1 + \mu_p)(1 - 2\mu_p)}}. \quad (5.1)$$

5.2 CONSTITUTIVE LAW

The stress–strain curve is obtained by a uniaxial tensile test. The curve can be calculated for true or engineering strains that relate to an undeformed cross-sectional area using the first Piola–Kirchhoff stress tensor. The engineering strains and stresses can be recalculated into true values up to the necking point using the following equations. [67].

$$\varepsilon = \ln(1 + e) \quad (5.2)$$

$$\sigma = s(1 + e) \quad (5.3)$$

Where σ is true stress, ε is true strain, s and e refer to engineering stress and strain. The experimentally obtained stress–strain curve of the tensile test and the hardening parameters for aluminium alloy 2024-T351 were taken from literature [67]. The true stress–strain curve was fitted by Swift hardening law using the Least Squares Method (LSM). The Swift hardening law is expressed as follows [34]

$$\sigma = K(\varepsilon_0 + \varepsilon_p)^n, \quad (5.4)$$

where K and n are strength coefficient and strain hardening exponent, respectively. ε_0 represents the initial (reference) yield strain and ε_p is plastic component of the true strain. The approximated flow curve by the Swift hardening law for aluminium alloy 2024-T351 is plotted in Fig. 15. [29], [34].

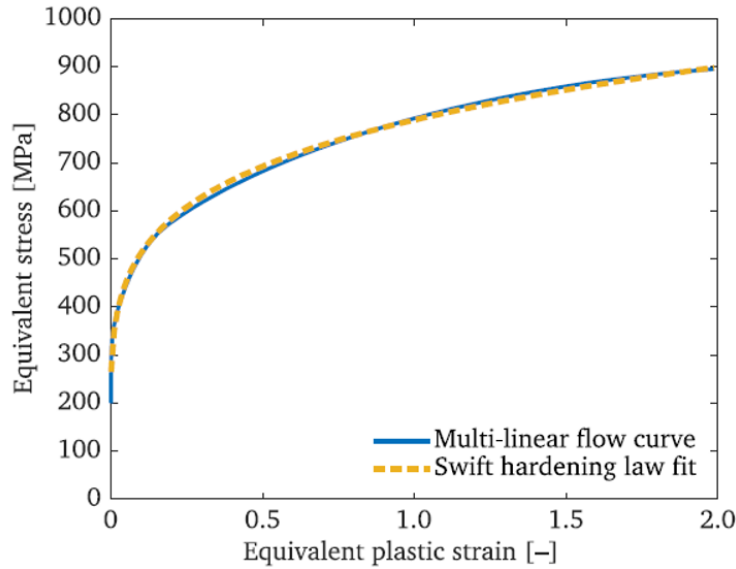


Fig. 15 Fitted flow curve [29]

The material parameters of the Swift hardening law are given in Table 3.

Table 3 Material parameters of the Swift hardening law [29]

Reference strain [-]	Strength coefficient [MPa]	Strain hardening exponent [-]
0.0031	788.60	0.1888

5.3 YIELD CRITERION

An accurate model of plasticity is necessary for a correct prediction of material behaviour. Without a reliable plasticity model that is consistent with experiments, it would be impossible to predict the onset and propagation of the fracture, since the fracture models are related to the plasticity function. In a study by Vobejda et al. [68], experiments on aluminium alloy 2024-T351 were performed and compared with numerical simulations using the von Mises plasticity model. In that study, the numerical simulations were not consistent with the experimental results. There were errors in the predictions of force–displacement and torque–twist angle responses. The largest scatter in the results was for shear dominant experiments. Thus, another model of plasticity had to be sought to eliminate these discrepancies. [68].

The Tresca and von Mises plasticity models were defined using an associated flow rule. The strain increment is perpendicular to the yield surface in the case of associated flow rule, as described in more detail in sub-chapter 4.2.2. This can be too restrictive; hence, in some studies, a non-associated flow rule in which the strain increment is not identical to the normal of the yield surface was used instead. In this thesis, an isotropic version

of plasticity model calibrated for aluminium alloy 2024-T351 and published by Vobejda et al. [68], was preferred over the conventional von Mises and Tresca criteria due to its better compliance with the experiments. It is a flexible convexity ensured yield criterion with a non-associated flow rule. It solves the problem of significant error in the results for the shear stress state by defining a lower yield stress for a given state of stress. The model can also be extended to anisotropy. However, this would lead to only a negligible increase in accuracy at the cost of a more complex function. The yield function contains material parameters by which the model is calibrated for a given material. [68].

The employed plasticity model has already been calibrated in literature [68] by conducting the following experiments: tensile tests of smooth cylindrical specimens, tensile tests of cylindrical specimens with various notches, tensile tests of flat plates for plane strain, tensile and torsion tests of notched tubes, compression tests of cylindrical specimens, and upsetting tests of cylindrical specimens with notches. These experiments were able to capture a sufficiently wide range of stress states. [68].

Unlike the Tresca and von Mises criteria, which have a fixed hexagonal and circular shape, the locus of the adopted plasticity model can exhibit various shapes that are dependent on seven material parameters $m, k_a, k_b, c, n_{TC}, n_\xi$ and c_{rel} . The radius of the yield function and plastic potential in the deviatoric plane of the Haigh–Westergaard stress space can be plotted using the following equation. [68].

$$r = \sqrt{\frac{2}{3}} \sigma_y \cdot k \quad (5.5)$$

Where σ_y is yield stress, which is determined experimentally. Yielding occurs when the equivalent stress reaches this value. k is a correction function that ensures convexity of the yield locus. The correction function is defined as follows [68]

$$k = \frac{\sqrt{F(\alpha)F(\beta)}}{1 - c_{rel}}, \quad (5.6)$$

where $c_{rel} = c$ when $c \neq 0$ and $n_{TC} = 0$. c_{rel} together with other material parameters are described in more detail in the original article [68]. n_{TC} is another material parameter. When the yield stress in tension is greater than the yield stress in compression, n_{TC} is 1, conversely, if the yield stress in compression is greater, n_{TC} is 0. The equation for calculating the material parameter c is written as [68]

$$\begin{aligned} c &= 1 - \frac{\sigma_{yT}}{\sigma_{yC}} & \text{for } n_{TC} = 0, \\ c &= 1 - \frac{\sigma_{yC}}{\sigma_{yT}} & \text{for } n_{TC} = 1, \end{aligned} \quad (5.7)$$

where σ_{yT} and σ_{yC} is yield stress in tension and compression, respectively. The functions $F(\alpha)$ and $F(\beta)$ are calculated as follows [68]

$$F(\alpha) = 1 - k_a a_m \left(\frac{1 + k_b b_m}{1 + k_b b_m \alpha^{\frac{1}{m}}} \right)^m \alpha, \quad (5.8)$$

$$F(\alpha) = 1 - k_a a_m \left(\frac{1 + k_b b_m}{1 + k_b b_m \beta^{\frac{1}{m}}} \right)^m \beta, \quad (5.9)$$

where k_a and k_b are material parameters that take values from 0 to 1. They were introduced as multiples of the material parameters a_m and b_m to increase the flexibility of the locus. They are calculated as follows [68]

$$a_m = \frac{1 + k_b b_m}{19 + k_b b_m}, \quad (5.10)$$

$$b_m = \frac{41m}{54 + 13m}. \quad (5.11)$$

α and β are functions of the third invariant of deviatoric stress tensor defined as [68]

$$\alpha = 1 - \xi^2, \quad (5.12)$$

$$\beta = 1 - \xi^2 + f(c) \left(\frac{1 + (-1)^{n_{rc}} \xi}{2} \right)^{n_{\xi} + 2}, \quad (5.13)$$

where n_{ξ} is material parameter and $f(c)$ denotes relation function expressed as follows [68]

$$f(c) = \frac{2c - c^2}{\left[(k_a a_m)^{\frac{1}{m}} (1 + k_b b_m) - (2c - c^2)^{\frac{1}{m}} k_b b_m + 0^{k_a} \right]^m}. \quad (5.14)$$

$0^{k_a} = 1$ when $k_a > 0$ and $0^{k_a} = 0$ when $k_a = 0$, this parameter was introduced to prevent division by zero. Finally, the yield function and the plastic potential in the stress space can be expressed as [68]

$$f = \frac{\sqrt{3J_2}}{\sqrt{F(\alpha)F(\beta)}} (1 - c_{rel}). \quad (5.15)$$

Geometrical representation of the yield locus in the deviatoric plane for different values of k_a is plotted in Fig. 16. Note that the yield locus is dependent on seven material parameters. The figure shows only the effect of material parameter k_a . By changing other parameters, the shape of the locus can vary significantly. The yield locus is convex for any combination of k_a and k_b , however the convexity is not ensured when $c \neq 0$. Therefore, in such a case, the curvature expressed by the following equation should be checked. [68].

$$\kappa = \frac{r^2 + 2 \left(\frac{dr}{d\theta} \right)^2 - r \frac{d^2 r}{d\theta^2}}{\left(r^2 + \left(\frac{dr}{d\theta} \right)^2 \right)^{\frac{3}{2}}} \quad (5.16)$$

The yield function as described in this thesis is independent of hydrostatic pressure; however, the criterion can be extended by this variable. The hydrostatic pressure dependence

of the extended criterion can be linear, elliptical, and power-law. The adopted plasticity model was in accordance with the experimental results, in contrast to the von Mises' model, which in many experiments overestimated both the torque–twist angle and the force–displacement responses. Nevertheless, the employed model of plasticity is only suitable for monotonic loading as it lacks a kinematic hardening formulation. This is not an issue for the numerical simulation of the experiments in this thesis as all samples were loaded monotonically until rupture. [68].

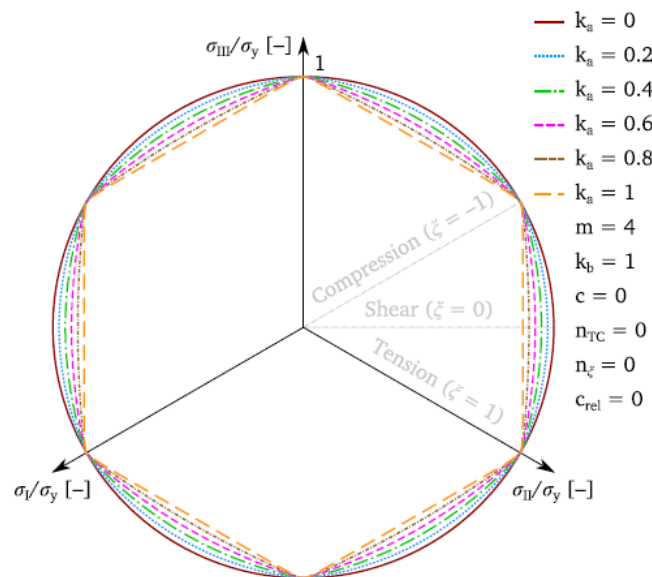


Fig. 16 Yield locus in the deviatoric plane [68]

The material parameters of the plasticity model in the original article [68] were calibrated to obtain similar stress–strain responses from numerical simulations as from experiments. These calibrated material parameters for aluminium alloy 2024-T351 are listed in Table 4. The indices y correspond to yield function and the indices p correspond to plastic potential. [68].

Table 4 Material parameters of the plasticity model for aluminium alloy 2024-T351 [68]

m_y [-]	$k_{a,y}$ [-]	$k_{b,y}$ [-]	c_y [-]	$n_{TC,y}$ [-]	$n_{\xi,y}$ [-]	$c_{rel,y}$ [-]
4	1	0.8	0	0	0	0
m_p [-]	$k_{a,p}$ [-]	$k_{b,p}$ [-]	c_p [-]	$n_{TC,p}$ [-]	$n_{\xi,p}$ [-]	$c_{rel,p}$ [-]
4	0	0	0	0	0	0

The presented model is suitable for implementation into FEM without any modification, as it does not contain any singular points. This model is not directly implemented in Abaqus/Explicit; therefore, it was necessary to use the user subroutine VUMAT. An explicit version of Abaqus had to be utilized because the implicit version is not capable of solving problems using the element deletion technique, which was used for fracture modelling. In the explicit version of any FEM, the responses in step (N) are calculated from the responses in step (N – 1). In each step, the following equation is checked. [68].

$$F^{(N)} = f_y(\underline{\sigma}) - \sigma_y(\bar{\varepsilon}_p^{(N-1)}), \quad (5.17)$$

where f_y is yield function according to Eq. (5.15), The deformation is elastic when $F^{(N)} < 0$ and elastic-plastic if $F^{(N)} \geq 0$. When the deformation is elastic, the behaviour of the material is governed by Hooke's law described in sub-chapter 5.1. Conversely, when the deformation is plastic, the behaviour of the material is governed by the plasticity function together with the flow rule and the hardening law. Plasticity is computed in an incremental fashion due to its nonlinearity. [68].

5.4 DUCTILE FRACTURE CRITERIA

Four of the following fracture criteria (modified Mohr–Coulomb, Ganjiani, KHPS2, and Lou–Huh) have been calibrated by macroscopic samples in this thesis. The calibrated KHPS2 criterion, along with the presented models of elasticity and plasticity, were used to design four miniature specimens described in chapter 7.

5.4.1 MODIFIED MOHR–COULOMB CRITERION

The Mohr–Coulomb criterion is a phenomenological criterion that was originally formulated for brittle materials such as rocks, concrete, and ceramics. Later, the original criterion was modified by Bai–Wierzbicki [33] to predict the fracture onset of ductile materials. The modified Mohr–Coulomb criterion in the $\bar{\varepsilon}_p, \eta, \bar{\theta}$ space is expressed as follows [33], [62]

$$\bar{\varepsilon}_f = \left\{ \frac{K}{c_2} \left[\sqrt{\frac{1+c_1^2}{3}} \cos\left(\frac{\bar{\theta}\pi}{6}\right) + c_1 \left(\eta + \frac{1}{3} \sin\left(\frac{\bar{\theta}\pi}{6}\right) \right) \right] \right\}^{-\frac{1}{n}}. \quad (5.18)$$

The criterion contains a total of four material parameters (K, n, c_1, c_2), but only two parameters (c_1, c_2) must be calibrated by experiments carried out up to fracture. The Swift hardening parameters K and n can be determined from the same tests that were performed to obtain the c_1 and c_2 values. The parameter c_1 , also referred to in the literature as a friction coefficient, affects the pressure dependence of the fracture locus, while the parameter c_2 , also called shear resistance, controls the height of the locus without influencing its shape. Both parameters range from 0 to positive values. Since the criterion contains only a few material parameters, it can be easily calibrated even by the trial-and-error method. Nevertheless, the downside of this simplicity is lower accuracy of the fracture prediction. [33], [37].

It has been shown that below a certain stress triaxiality threshold, damage does not accumulate, and the equivalent fracture strain approaches infinity. The modified Mohr–Coulomb criterion predicts that damage does not accumulate when the upcoming equation is satisfied. [33].

$$\sqrt{\frac{1+c_1^2}{3}} \cos\left(\frac{\bar{\theta}\pi}{6}\right) + c_1 \left(\eta + \frac{1}{3} \sin\left(\frac{\bar{\theta}\pi}{6}\right) \right) \leq 0 \quad (5.19)$$

The cut-off plane appears automatically when Eq. (5.18) is plotted as a consequence of the modified Mohr–Coulomb model.

5.4.2 GANJIANI FRACTURE CRITERION

Ganjiani's fracture criterion is another fracture model that has been calibrated. It is a simple phenomenological criterion with only two material parameters calibrated by fracture tests. It was proposed recently by Ganjiani [69]. The criterion, along with many others, is a function of stress triaxiality and normalized Lode angle. These two parameters play an important role in the ductile fracture mechanics, as shown by several studies. The proposed model for proportional loading is stress based and is given as follows [70]

$$\frac{\bar{\sigma}_f^{ref}}{\bar{\sigma}_f} = 1 + c_\eta \ln\left(\frac{1 + \eta}{1 + \eta^{ref}}\right) - c_\theta (\bar{\theta} - \bar{\theta}^{ref})^2, \quad (5.20)$$

where c_η and c_θ are material parameters calibrated by experiments performed up to fracture. The index ref indicates the test that is used to determine the material parameters of the function. From Eq. (5.20), the equivalent fracture strain can be derived as [70]

$$\bar{\varepsilon}_f = \left[1 + c_\eta \cdot \ln\left(\frac{1 + \eta}{1 + \eta^{ref}}\right) - c_\theta (\bar{\theta} - \bar{\theta}^{ref})^2 \right]^{\frac{1}{n}} (\varepsilon_0 + \bar{\varepsilon}_f^{ref}) - \varepsilon_0. \quad (5.21)$$

The cut-off stress triaxiality can be calculated by setting Eq. (5.20) to zero. By doing so, the following equation is obtained, from which the cut-off stress triaxiality η_c can be easily expressed. [70].

$$\ln\left(\frac{1 + \eta_c}{1 + \eta^{ref}}\right) = \frac{1}{c_\eta} [c_\theta (\bar{\theta} - \bar{\theta}^{ref})^2 - 1] \quad (5.22)$$

Note that any of the criteria can be transferred from the $\bar{\varepsilon}_p, \eta, \bar{\theta}$ space to $\bar{\varepsilon}_p, \eta, \xi$ space by Eq. (3.26), as done in this thesis. The material constant c_η determines the stress triaxiality dependence of the fracture locus, while the constant c_θ determines the Lode angle dependence. The fracture strain can be made independent of the Lode angle by setting c_θ equal to zero. The material parameters c_η and c_θ can only be positive when the cut-off plane is required to be convex. [68], [69], [70].

5.4.3 KHPS2

The third ductile fracture criterion that has been calibrated is an uncoupled phenomenological criterion recently published by Šebek et al. [67]. It contains more material parameters than the previous two criteria, making it more versatile. It is a modification of a hyperbolic KHPS criterion proposed by Kubík et al. [71]. The main difference between the modified and the original version is that the foci of rectangular (or equilateral) hyperbolas are quadratic functions of the normalized third invariant of the deviatoric stress tensor, in contrary to KHPS, where the dependence is only linear. The modified version is more versatile and flexible. The criterion, like the others, is dependent on the stress triaxiality and normalized third invariant of the deviatoric stress tensor. Function of the equivalent fracture strain is expressed as follows [58], [72], [73]

$$\bar{\varepsilon}_f = \left[\frac{1}{2} \left(\frac{G_4}{\langle \eta - \eta_c \rangle} + \frac{G_5}{\langle \eta - \eta_c \rangle} \right) - \frac{G_6}{\langle \eta - \eta_c \rangle} \right] \xi^2 + \frac{1}{2} \left(\frac{G_4}{\langle \eta - \eta_c \rangle} - \frac{G_5}{\langle \eta - \eta_c \rangle} \right) \xi + \frac{G_6}{\langle \eta - \eta_c \rangle}, \quad (5.23)$$

where G_4, G_5 , and G_6 are material constants. $\langle \dots \rangle$ are Macaulay brackets. $\langle x \rangle = (x + |x|)/2$ is an example of Macaulay bracket notation. η_c denotes the cut-off stress triaxiality beyond which the damage does not accumulate. The cut-off stress triaxiality is a parabolic function that can be expressed as [58], [72]

$$\eta_c = -\left(G_3 + \frac{G_1 - G_3}{2} - G_2\right)\xi^2 - \frac{G_1 - G_3}{2}\xi - G_2, \quad (5.24)$$

where G_1, G_2 and G_3 are additional material constants that define the distance of a cut-off plane in the stress triaxialities. Specifically, G_1 at $\xi = 1$, G_2 at $\xi = 0$ and G_3 at $\xi = -1$. In addition, the material parameters G_4, G_5 and G_6 influence the vertices of rectangular hyperbolas at $\xi = 1$, $\xi = -1$ and $\xi = 0$, respectively, and must be positive. The effect of each material constant is illustrated in Fig. 17. [29], [73].

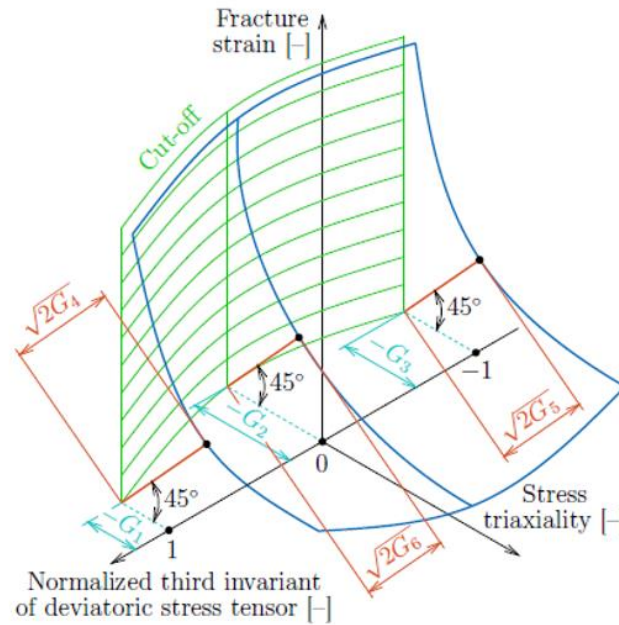


Fig. 17 Graphical representation of material constants of the KHPS2 criterion [67]

To correctly calibrate the criterion, two types of constraints must be met. The first constraint $\eta_c - \eta_{av} < 0$ ensures the fracture strain to be positive. The second constraint, expressed by the following equation, guarantees that the curvature of the cut-off plane is positive in Cartesian coordinates, which ensures the convexity of the cut-off plane. [29], [67], [72].

$$\kappa = \frac{\frac{d^2\eta_c}{d\xi^2}}{\left(1 + \left(\frac{d\eta_c}{d\xi}\right)^2\right)^{\frac{3}{2}}} = \frac{-(G_1 - 2G_2 + G_3)}{\left(1 + \left(|G_1 - 2G_2 + G_3|\xi + \frac{G_1 - G_3}{2}\right)^2\right)^{\frac{3}{2}}} > 0 \quad (5.25)$$

The cut-off plane is convex when the following equation is satisfied as the denominator is always positive in Eq. (5.25). [67].

$$\frac{d^2\eta_c}{d\xi^2} = -(G_1 - 2G_2 + G_3) > 0 \quad (5.26)$$

Although the criterion contains six material parameters that need to be calibrated, the calibration is easy as each of the three vertices shown in Fig. 17 are affected by only two material parameters, and the individual vertices do not affect each other.

5.4.4 LOU-HUH FRACTURE CRITERION

The last calibrated fracture criterion was proposed by Lou et al. [74]. It is based on the microscopic mechanism of ductile fracture, which consists of nucleation, growth, and coalescence of voids. Lou et al. [74] proposed the criterion in the following form [74], [75]

$$\left(\frac{2}{\sqrt{\bar{\theta}^2 + 3}}\right)^{c_1} \left(\left|\frac{f(\eta, \bar{\theta}, C)}{f(1/3, -1, C)}\right|\right)^{c_2} \bar{\varepsilon}_f = C_3. \quad (5.27)$$

This is consistent with the next equation, that was obtained by modifying and transferring the function (5.27) into the $\bar{\varepsilon}_p, \eta, \xi$ space. The calibration and plotting was done using the function of equivalent fracture strain in the following form [67]

$$\bar{\varepsilon}_f = C_3 \left(\frac{2}{\sqrt{3 \left[1 + \tan^2 \left(-\frac{1}{3} \arcsin[\xi] \right) \right]}} \right)^{-c_1} \times \left(\frac{3}{1 + 2C_4 + 3C_5} \left(\eta + C_4 \frac{\sqrt{3} - \tan \left(-\frac{1}{3} \arcsin[\xi] \right)}{3 \sqrt{1 + \tan^2 \left(-\frac{1}{3} \arcsin[\xi] \right)}} + C_5 \right) \right)^{-c_2}, \quad (5.28)$$

where C_1, C_2, C_3, C_4 and C_5 are five material constants that must be calibrated by experiments. The cut-off stress triaxiality is formulated as [67], [75]

$$\eta_c = -C_4 \frac{\sqrt{3} - \tan \left(-\frac{1}{3} \arcsin[\xi] \right)}{3 \sqrt{1 + \tan^2 \left(-\frac{1}{3} \arcsin[\xi] \right)}} - C_5. \quad (5.29)$$

Material parameter C_1 models the influence of normalized maximum shear stress on the coalescence of voids. The effect of stress triaxiality on the void growth is modelled by a parameter C_2 . Parameter C_3 represents the fracture strain $\bar{\varepsilon}_f$ in a stress state equal to uniaxial tension. This parameter does not affect the shape of the fracture locus. The parameter C_4 influences the dependence of the cut-off stress triaxiality on the Lode parameter and the parameter C_5 represents the height in stress triaxiality of the cut-off plane. [74], [75].

Correctly, the material parameters C_1 and C_2 should not be constant during the deformation process. However, for simplicity of evaluation, it is acceptable to consider them constant throughout the deformation. [74].

6 CALIBRATION

6.1 CALIBRATION OF THE DUCTILE FRACTURE CRITERIA

The material parameters determine the shape, height, and cut-off values of the fracture locus. Calibration is done by adjusting their values so that the envelope approximates the experimental points. The ductile fracture models were initially calibrated in MATLAB using the LSM, which was performed by command `lsqnonlin`. Although the LSM can be used to determine the material parameters, it is not the most appropriate method for this task, as it often finds only local minima. Finding the global minimum using this method is not certain and can be time consuming; therefore, a more suitable artificial intelligence method called the Particle Swarm Optimization (PSO) was used instead. The PSO is not as sensitive to local minima, making it a more powerful tool in the search for global minimum. It was inspired by a stochastic behaviour of animal groups, such as birds and fishes, in search of food. During this task, each member of the swarm varies its search pattern based on its own and others' learning experience. The PSO algorithm uses particles with velocities. The solution is found by moving each individual particle in steps through space. In every step, the objective function of each particle is evaluated. Based on the evaluation, the velocity of each particle is adjusted. The particles are to some degree bound to the best location they have found, and also to the best location any swarm member has found so far. The PSO requires to define several parameters such as swarm size, topology, inertia weight, etc. These parameters determine the ability to escape local optimization, and thus distinguish between global and local search. The PSO was combined with another optimization method called `fmincon` in MATLAB environment. This additional function was called after the completion of the PSO algorithm to find the best possible solution. The `fmincon` function is used to find a minimum of a nonlinear multivariable function. Flowchart of the PSO algorithm is shown in Fig. 18. [76], [77], [78], [79].

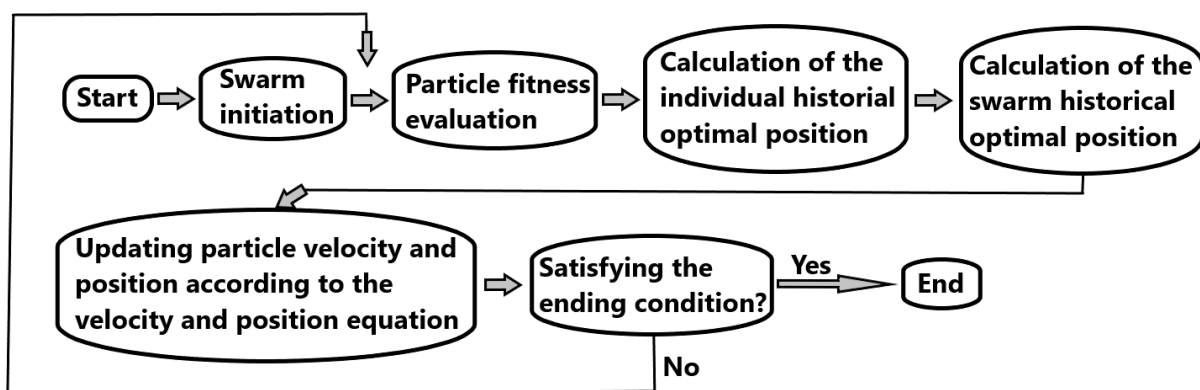


Fig. 18 Flowchart of the particle swarm optimization algorithm [77]

The calibration points used for the fracture locus calibration are listed in Table 5. These calibration values were taken from a study by Vobejda et al. [68].

Table 5 Calibration points from macroscopic specimens [68]

Specimens	Stress triaxiality η [-]	Normalized third invariant of deviatoric stress tensor ξ [-]	Fracture strain $\bar{\epsilon}_f$ [-]
Tensile specimen with R13 notch	0.583	1.000	0.206
Tensile specimen with R6.5 notch	0.745	1.000	0.153
Tensile specimen with R4 notch	0.917	1.000	0.115
Tubular tensile specimen with R4 notch	0.623	0.031	0.154
Torsional specimen	0.001	0.003	0.244
Tension of flat plate specimen	0.543	0.279	0.133
Cylindrical upsetting specimen	-0.295	-0.975	0.417
Notched upsetting specimen	-0.270	-0.942	0.588

The constants of the fracture criteria calibrated by the PSO are given in Table 6–9.

Table 6 Calibrated parameters of the modified Mohr–Coulomb fracture criterion

c_1 [-]	c_2 [MPa]
0.0974	336.2089

Table 7 Calibrated parameters of the Ganjiani fracture criterion

c_η [-]	c_θ [-]	η^{ref} [-]	ξ^{ref} [-]	$\bar{\epsilon}_f^{ref}$ [-]
0.2535	0.0548	0.001	0.003	0.244

Table 8 Calibrated parameters of the KHPS2 fracture criterion

G_1 [-]	G_2 [-]	G_3 [-]	G_4 [-]	G_5 [-]	G_6 [-]
-0.1472	1.1495	2.1284	0.0901	0.9446	0.2814

Table 9 Calibrated parameters of the Lou–Huh fracture criterion

C_1 [-]	C_2 [-]	C_3 [-]	C_4 [-]	C_5 [-]
-1.3845	587.5897	0.1077	3.5721	593.1541

The calibrated ductile fracture criteria in the space of $\bar{\epsilon}_p, \eta, \xi$ are plotted in Fig. 19. The circles, squares, triangles, and diamonds in the graphs represent calibration points that were used to fit the envelope. The values of these points are listed in Table 5. The blue surface plots the equivalent plastic strain boundary envelope. The purple surface displays the cut-off plane. The black line represents the projection of the plane stress curve onto the boundary equivalent plastic strain envelope. Finally, the red lines show the constant values of ξ at $\xi = -1$, $\xi = 0$ and $\xi = 1$.

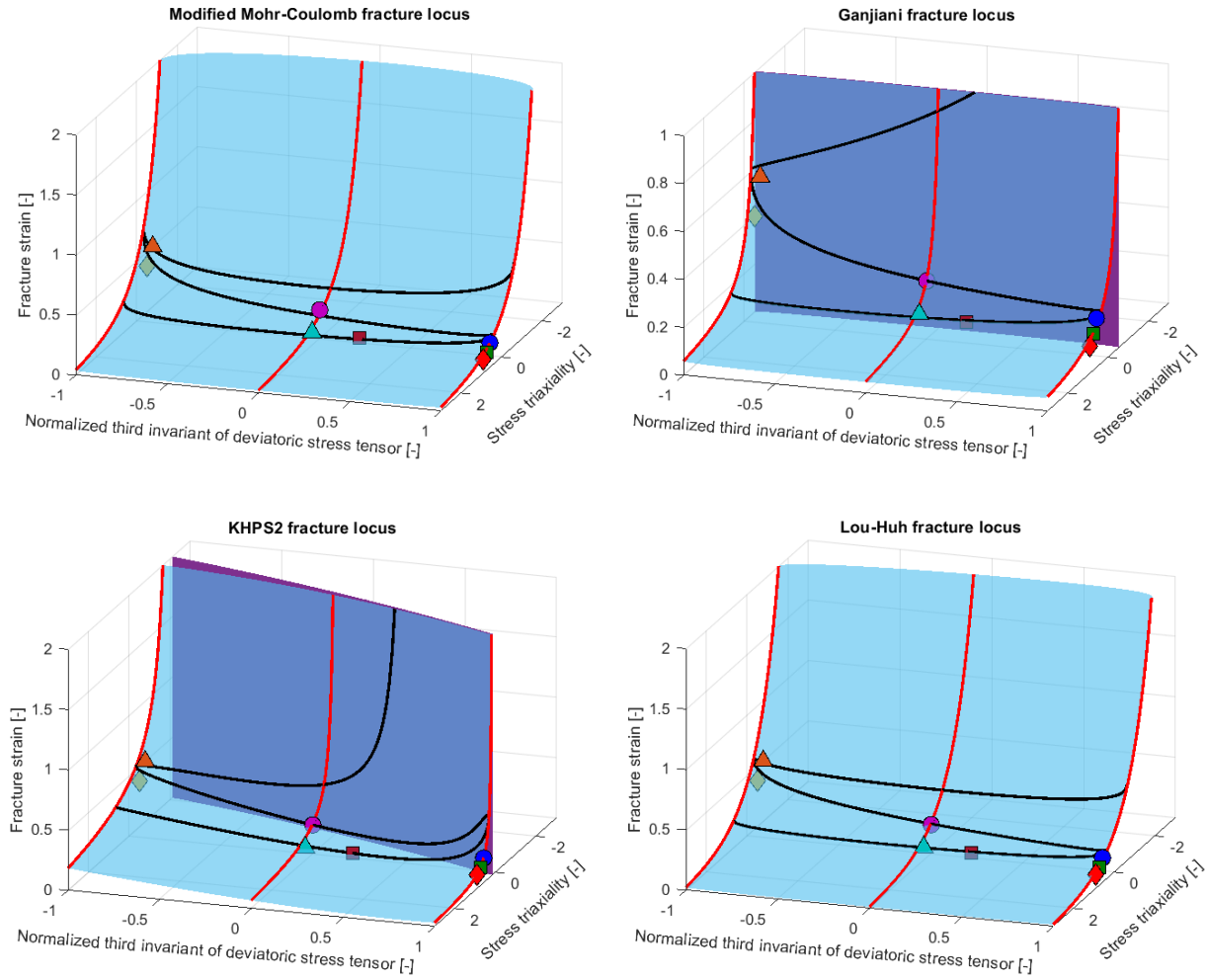


Fig. 19 Calibrated ductile fracture criteria

The specimens are represented by markers as follows

- | | |
|---|--|
| ● Torsional specimen | ● Tensile specimen with R13 notch |
| ■ Tensile specimen with R6.5 notch | ■ Tension of flat plate specimen |
| ◆ Tensile specimen with R4 notch | ◆ Cylindrical upsetting specimen |
| ▲ Notched upsetting specimen | ▲ Tubular tensile specimen with R4 notch |

The deviations in the approximation between the calibration points and the fracture locus are listed in Table 10. The errors were calculated as follows [67]

$$\frac{|\hat{\epsilon}_f - \bar{\epsilon}_f|}{\hat{\epsilon}_f} \cdot 100, \quad (6.1)$$

where $\hat{\epsilon}_f$ is a fracture strain of calibration point and $\bar{\epsilon}_f$ is a fracture strain value given by the calibrated ductile fracture envelope for the same values of ξ and η as the calibration points.

Table 10 Calibration errors of the macroscopic samples

Specimen	Modified Mohr-Coulomb error [%]	Ganjiani error [%]	KHPS2 error [%]	Lou-Huh error [%]
Tensile specimen with R13 notch	0.83	14.11	0.30	9.43
Tensile specimen with R6.5 notch	15.69	2.15	1.55	3.95
Tensile specimen with R4 notch	32.74	20.86	1.72	16.74
Tubular tensile specimen with R4 notch	25.17	15.01	0.31	12.54
Torsional specimen	19.88	0	0.07	2.41
Tension of flat plate specimen	7.69	5.61	0.40	6.56
Cylindrical upsetting specimen	28.30	22.65	22.00	24.75
Notched upsetting specimen	21.12	20.88	16.09	18.14
Sum (Total error)	151.41	101.26	42.43	94.52

The best approximation accuracy was achieved by the KHPS2 criterion, which was also used for the design of miniature specimens. The modified Mohr–Coulomb criterion has the worst accuracy of the four criteria, which is not surprising as it consists of only two material parameters calibrated by fracture tests. Additional material parameters generally make the envelope more flexible but harder for manual calibration; however, when using a more sophisticated approximation method such as the LSM, artificial bee swarm optimization or particle swarm optimization, the difficulty of calibrating each of the criteria is approximately the same. The error of the Ganjiani and Lou–Huh criteria is very similar; however, the Ganjiani criterion predicted the cut-off plane much more reasonably than the Lou–Huh criterion, even though it contains only two material parameters calibrated by fracture experiments, in contrary to the Lou–Huh criterion, which has five. The Mohr–Coulomb and Lou–Huh criteria calibrated by the PSO method predicted unrealistically low cut-off values that are inconsistent with experiments in studies. A reasonable cut-off values of these models can be achieved at the expense of a larger approximation error. Note that the calibration error of the torsional specimen in the Ganjiani criterion is 0. This fracture model requires the use of a reference experimental point, which is approximated precisely. The choice of a reference point affects the total calibration error as well as the error of each individual specimen. Each individual specimen (in Table 5) was tested as a reference sample. The most satisfactory results were achieved with the torsional specimen as a reference test. Testing different specimens as a reference sample is time consuming and reduces the advantage of the criterion of using only two material parameters. The steepness of the Ganjiani and KHPS2 criteria is greater compared to the modified Mohr–Coulomb and Lou–Huh models. The modified Mohr–Coulomb and Lou–Huh models also predicted significantly lower values of fracture strain with increasing stress triaxiality than the other two criteria.

All the criteria had difficulties with the upsetting tests approximation at $\xi \approx -1$. The significant error of these two upsetting specimens is due to the large difference in fracture strain between the two samples, while being located close to each other in the η, ξ plane. The fracture envelope is not flexible enough to further reduce the calibration error. The error of any individual specimen as well as the total calibration error can be further reduced

by changing the weight of specific samples in the minimized residuum formulation. This operation can lead to greater freedom of the envelope for the remaining calibration points. It was utilized in the calibration of KHPS2 and Lou–Huh criteria to reduce the total calibration error at the expense of a small increase in the error of specific samples. This approach was not used for the Ganjani and modified Mohr–Coulomb criterion because it reduced the overall error only slightly, while significantly increased the error of some specimens. The weight in the calibration function of the KHPS2 and Lou–Huh criteria was modified only for the cylindrical upsetting and notched upsetting specimens as it exhibited the largest reduction in the total calibration error and kept the calibration error of each individual specimen within a reasonable range. This was determined using the trial-and-error method. Table 11 shows a comparison of the KHPS2 and Lou–Huh calibration errors using calibration points with equal weights and weighted points while using the same particle swarm function.

Table 11 Comparison of the calibration error

Specimen	Unweighted KHPS2 error [%]	Weighted KHPS2 error [%]	Unweighted Lou–Huh error [%]	Weighted Lou–Huh error [%]
Tensile specimen with R13 notch	0.28	0.30	8.58	9.43
Tensile specimen with R6.5 notch	0.95	1.55	2.67	3.95
Tensile specimen with R4 notch	3.08	1.72	12.67	16.74
Tubular tensile specimen with R4 notch	7.42	0.31	12.55	12.54
Torsional specimen	2.20	0.07	11.10	2.41
Tension of flat plate specimen	9.09	0.40	9.28	6.56
Cylindrical upsetting specimen	21.06	22.00	22.17	24.75
Notched upsetting specimen	15.88	16.09	18.83	18.14
Sum (Total error)	59.96	42.43	97.85	94.52

This approach works better for some criteria than others. The calibration error of KHPS2 was reduced by 17.5 %. The use of the weighting approach for the Lou–Huh criterion is questionable, as the differences are minor, and the total error was reduced by only 3 %. It should be noted that the cut-off plane of the Lou–Huh criterion was located at distant negative stress triaxialities, regardless of whether the weighted or unweighted approach was used.

The side and top view of Fig. 19, which provides a better overview of the experimental point topology with respect to the plane stress curve is displayed in Fig. 20 and 21. The lines in Fig. 20 represent the projection of the plane stress curve onto the $\eta - \bar{\epsilon}_p$ plane (projection of the black lines from Fig. 19 onto the $\eta - \bar{\epsilon}_p$ plane). The curve is computed by Eq. (3.29). The projection of the experimental points, plane stress curve, and cut-off values onto the $\xi - \eta$ plane is shown in Fig. 21. Only the Ganjani and the KHPS2 cut-off values are within a reasonable range. The cut-off plane of the Lou–Huh criterion is located in the high negative stress triaxialities and thus could not be displayed in Fig. 21 without significant compression of the remaining plots.

The calibration error of the KHPS2 criterion in the original article of Vobejda et al. [68], is approximately 52.79 %. Comparison of the KHPS2 criterion calibrated in the original article and in this thesis is plotted in Fig. 22.

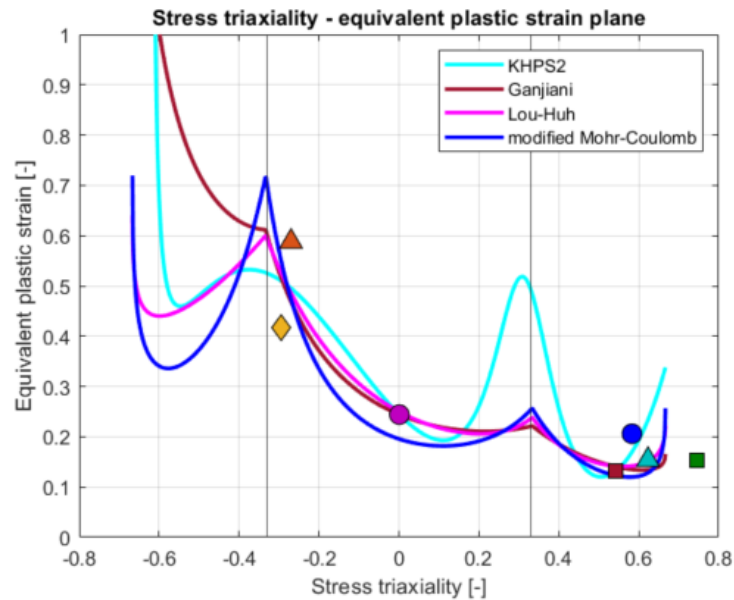


Fig. 20 Location of calibration points in stress triaxiality – equivalent plastic strain plane

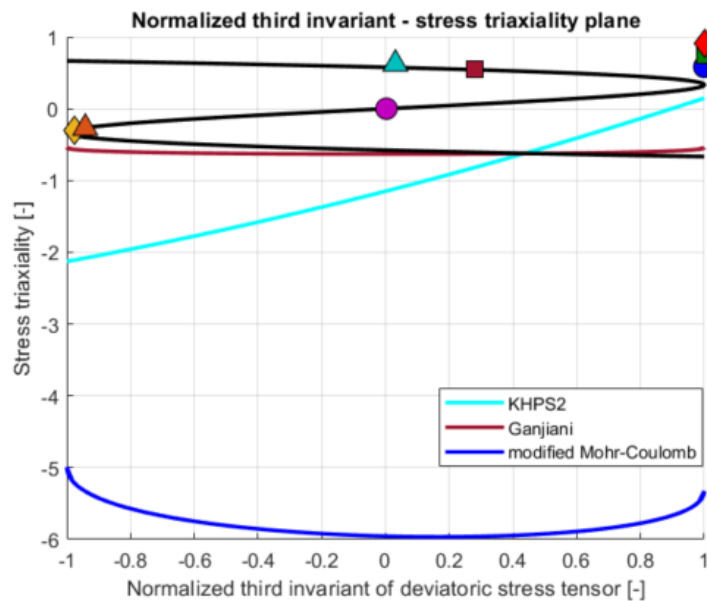


Fig. 21 Location of calibration points and cut-off stress triaxiality in $\xi - \eta$ plane

6.2 INFLUENCE OF INITIAL GUESS AND MINIMIZED RESIDUUM FORMULATION

The final material parameters and thus the calibration accuracy obtained by the optimization algorithm are often dependent on the initial estimate of the material parameters entering the minimized function. The initial guess is particularly important for algorithms that

are sensitive to local minima, such as the LSM. In the case of the LSM, the resultant material parameters calculated by the optimization function are then generally set as new initial values, and the calculation is repeated until a minimum is reached. It is recommended to repeat this procedure with several different first estimates, which often provide different results. The most satisfactory result is then used in the fracture strain function for numerical simulations. The PSO led to the same results in most cases regardless of the initial material parameter guesses, as long as their initial values and boundary conditions were set reasonably. Therefore, the steps mentioned for the LSM were no longer necessary and served primarily for verification purposes only. It should be noted that the behaviour of the LSM and PSO algorithms are highly dependent on the nature of the minimized function.

The results also depend on the minimized residuum formulation, which is usually used in the following form

$$f_m = \sum_{i=1}^n (\hat{\varepsilon}_{f_i} - \bar{\varepsilon}_{f_i})^2. \quad (6.2)$$

Note that the fracture strain difference is squared. It provides a relatively uniform distribution of errors between the calibration points. If the function is not quadratic, but an absolute value is used instead, the total calibration error can be further reduced, however, the approximation changes in interpolation of several specific samples, leaving other samples with a large calibration error. For that reason, it is not suitable for calibration of the models, although it provides the lowest overall error, which was 34.6 % for the KHPS2 criterion. This calibration is plotted in Fig. 22 and is labelled as non-quadratic. The various sample weights described in sub-chapter 6.1 were created by adjusting the power of specific samples in Eq. (6.2).

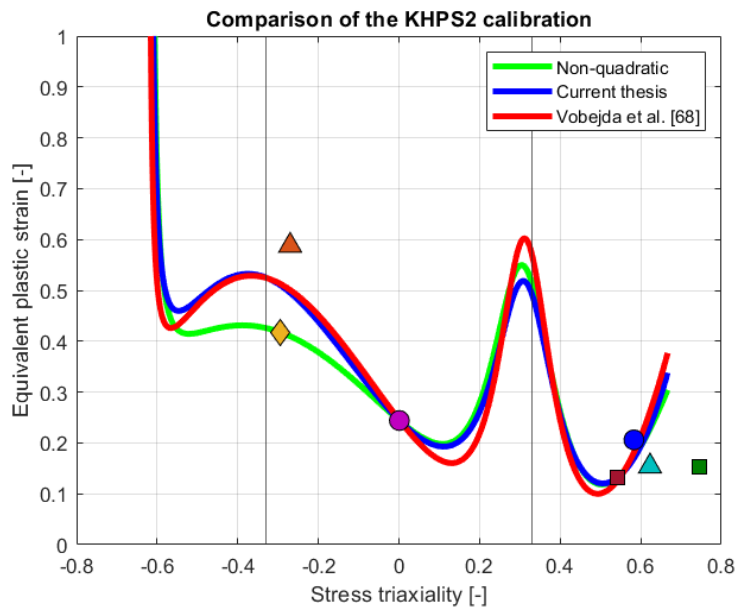


Fig. 22 Comparison of the KHPS2 calibration

7 SPECIMEN DESIGN USING NUMERICAL SIMULATIONS

Four specimens, called uniaxial tension specimen, notched R4 specimen, plane strain specimen, and shear specimen, were designed using the material models presented in the previous chapters. Numerical simulations were used to calculate the values of η and ξ of the specimens. These two parameters were extracted from the estimated fracture initiation location or a conventionally defined location and averaged throughout the numerical simulation using Eq. (4.7) and (4.8). This chapter deals with the specimen design and numerical simulations of the experiments.

The goal was to design specimens representing uniaxial tension ($\xi = 1, \eta = 1/3$), shear ($\xi = 0, \eta = 0$), plane strain ($\eta = \sqrt{3}/3, \xi = 0$), and a specimen with $\xi = 1$ and the largest possible value of η . The samples were intended to be tested on an already constructed tensile testing device for miniature specimens. Since the testing device had already been constructed, the samples had to be adjusted to fit into the testing apparatus. Therefore, the maximum force required for rupture and the maximum dimensions were significantly restricted. The designed specimens had to rupture up to a load of 775 N. The specimen length was restricted to 22 mm. The maximum width and thickness were limited to 10 mm and 0.5 mm, respectively. The samples had to be easily manufacturable, which further complicated the design process, especially for the shear specimen. For the shear and plane strain specimens, a compromise between the ideal stress state in the predicted fracture initiation location and manufacturability had to be sought.

Note that the designed specimens have only a close to zero or positive values of stress triaxiality and normalized third invariant of deviatoric stress tensor. Negative values of η are achieved by compression tests, which were not doable on the testing device. These four specimens are not sufficient to properly calibrate the entire fracture locus because none of the specimens are located in an area with ξ close to -1 . Fracture models calibrated using only these four samples cannot be compared to the ductile fracture models calibrated by macroscopic samples to investigate the differences between the criteria calibrated by micro and macro samples. Thus, a SPT was additionally used to cover the missing stress state. The SPT uses a miniature sample with initial values in the critical location of $\eta = 2/3$ and $\xi = -1$. This test was done by Šebek et al. [72].

The numerical simulations were conducted using Abaqus/Explicit. The material models presented in chapter 5 were implemented in a VUMAT subroutine provided by the supervisor, which was called externally before the calculations. Only one of the fracture models was used in the VUMAT subroutine, which was the KHPS2 criterion. The material was considered a homogeneous isotropic continuum with isotropic hardening. Because explicit numerical codes require a very small time step, the time and mass scalings were used in all numerical simulations to speed up the computational process. The simulation time was 0.1 s and mass scaling with a target time increment of $5 \cdot 10^{-7}$ s was applied. The time and mass scalings can affect the results when their values are chosen incorrectly. To avoid influencing the results, an increase in kinetic energy caused by the scaling was checked. Fig. 23 shows a comparison of kinetic to internal energy during numerical simulation of one of the miniature specimen tests. In the figure, ALLKE represents the kinetic energy, and ALLIE corresponds to the internal energy of the whole model. Another feature used to reduce computational time and simplify the geometry were symmetric boundary conditions. All specimens were meshed using eight-node linear brick elements with reduced

integration formulation (C3D8R). The geometry and dimensions of the specimens to obtain a certain stress state were designed using a trial-and-error method. Although there are more sophisticated but more complicated geometry optimization methods. Nevertheless, the potential of this approach would not be fully exploited in this thesis, as most specimens had to be modified far from ideal due to manufacturing difficulties. When the manufacturability is not an issue, which is for most macro-scaled specimens, the optimization methods can of course determine ideal geometry dimensions faster and more reliably than the trial-and-error method.

Note that in Fig. 23 the internal energy is linearly increasing up to a certain point, after which it begins to oscillate around a constant value. The linear energy increase stops when the first elements of the sample are being removed. The removal of elements to simulate fracture propagation also reduces the mass of the sample. Therefore, it is important to have a fine mesh in the fracture zone to prevent excessive mass loss when using the element deletion technique.

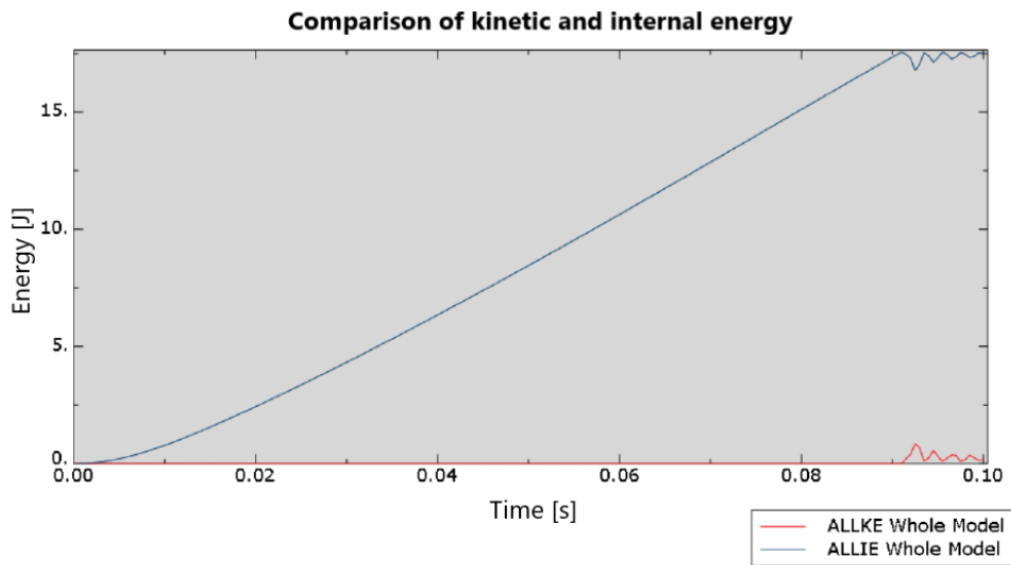


Fig. 23 Comparison of kinetic and internal energy during numerical simulation

Drawings of the designed specimens are shown in Fig. 24–27. The averaged η and ξ values of these samples extracted from numerical simulations are given in Table 12. These parameters have been averaged using trapezoidal numerical integration in MATLAB (function trapz).

Table 12 Average values of η and ξ given by numerical simulations

Specimen	Averaged stress triaxiality η [-]	Averaged normalized third invariant of the deviatoric stress tensor ξ [-]
Uniaxial tension	0.362	0.983
Notched R4	0.409	0.962
Plane strain	0.566	0.093
Shear stress	-0.020	-0.078

Since the values of stress triaxiality and normalized third invariant of the deviatoric stress tensor in the table have been determined numerically, they are not exact but represent only estimation of the actual values. Their accuracy is mainly influenced by material models used to calculate the stress state in the nodes and mesh. Nevertheless, the mesh was constructed thoroughly to minimize computational errors. The material models, with the exception of the ductile fracture models, have already been calibrated for aluminium alloy 2024-T351 in the VUMAT subroutine provided by the supervisor.

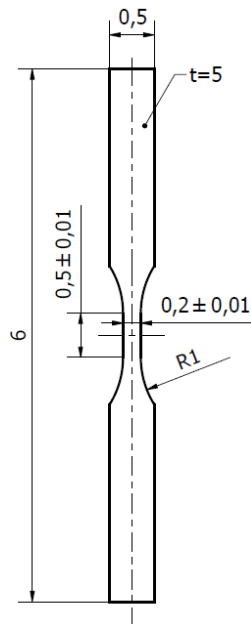


Fig. 24 Plane strain specimen

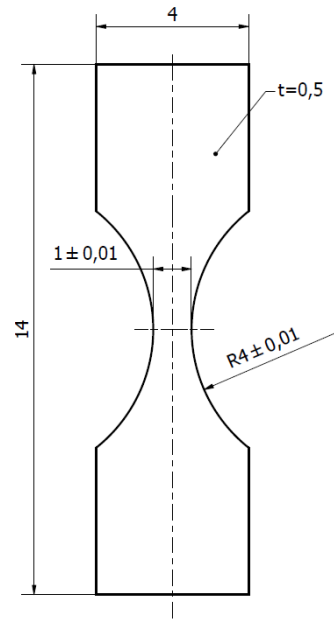


Fig. 25 Notched R4 specimen

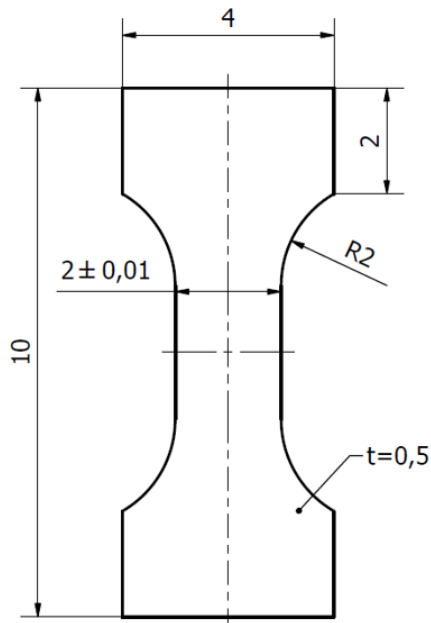


Fig. 26 Uniaxial tension specimen

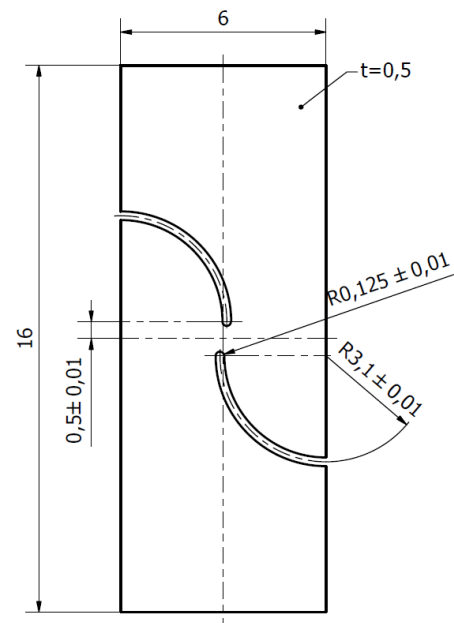


Fig. 27 Shear specimen

In many studies, the stress state is mostly mapped using round bars. Experiments with these axisymmetric specimens can capture a broader range of stress triaxialities for $\xi \approx 1$ than flat

samples. Some researchers have been able to obtain a value of η greater than 1 while keeping ξ equal to 1 using round bars. The highest possible value of η obtained in this thesis while keeping $\xi \approx 1$ using flat notched dog-bone specimens is only 0.4. Experiments of axisymmetric specimens consist of tension tests of smooth and notched round bars, torsion, and compression tests. Despite many limitations of the plane strain and shear specimens, the stress parameters of the designed specimens are satisfactory and comparable to the results provided in studies, such as [33], [80], [81], where the same material aluminium alloy 2024-T351 was used. Compression tests can be performed using smooth and notched round bars, which could not be performed on the designed testing device. The stress triaxialities with $\xi = 0$ can also be mapped using flat grooved specimens. Nevertheless, this state of stress has already been mapped by the shear and plane strain samples. Moreover, these samples would be very difficult to manufacture.

When designing the specimens, the influence of each individual dimension on η and ξ was investigated first. In the case of a notched R4 specimen, for which the goal was to obtain a high value of η while maintaining ξ close to 1, the stress triaxiality increased with increasing thickness, hence the thickness was set to 0.5 mm. This was the upper thickness limit for which the specimens were designed. The length and width had a negligible effect on the η and ξ values. Therefore, the main parameters left to calibrate were the radius of the notch and the width in the notch area. Many numerical simulations with different values of these two dimensions have been performed to obtain an extensive set of results. The most satisfactory samples were selected for further numerical simulations with different values of the less important dimensions, such as length and width. However, these dimensions in the case of the notched R4 specimen affected the η and ξ only slightly, if at all. The other specimens were designed in a similar way. Great emphasis was devoted to the maximum fracture force, which was limited to 775 N. It was mainly a problem when designing the plane strain specimen. The width of the plane strain sample for a thickness of 0.2 mm was limited to only 5 mm due to force limitation. A lower thickness than this would be too fragile. The plane strain was difficult to obtain because the width and thickness were limited. In addition, the initially designed plane strain specimen had to be modified due to manufacturing complexity. The adjusted specimen has almost double the value of ξ . Nevertheless, the biggest compromise was made in the case of a shear specimen.

The initially proposed shear specimen had narrow grooves on both sides of the specimen in the transitional area between the through grooves R3.1. The lateral grooves were created to relocate the crack initiation site to a location with a shear stress state by reducing the thickness and creating a stress concentrator. The same approach has also been taken in some studies, such as [34] and [35]. However, this geometric feature had to be removed as it would be too complicated to manufacture. Although the fracture initiation site of the new shear specimen predicted by the FEM is not directly in the node with shear stress state, the specimen is still used to investigate shear because a stress state close to shear is present in most of the cross-sectional area through which the crack propagated. The originally proposed shear specimen before modification is shown in Fig. 28.

Due to symmetry, only one-eighth of the uniaxial tension, notched R4 and plane strain specimens was modelled. One symmetry condition was used in the case of a shear specimen. To further reduce computational time, a coarser mesh was used outside the fracture zone of the models. The mesh was coarsened with increasing distance from the critical region using the bias tool. The size of the elements in the fracture zone for each proposed specimen was as follows: uniaxial tension specimen $0.020 \times 0.009 \times 0.014$ mm, notched R4 specimen $0.016 \times 0.007 \times 0.016$ mm, plane strain specimen $0.031 \times 0.004 \times 0.006$ mm, and shear specimen $0.004 \times 0.010 \times 0.025$ mm.

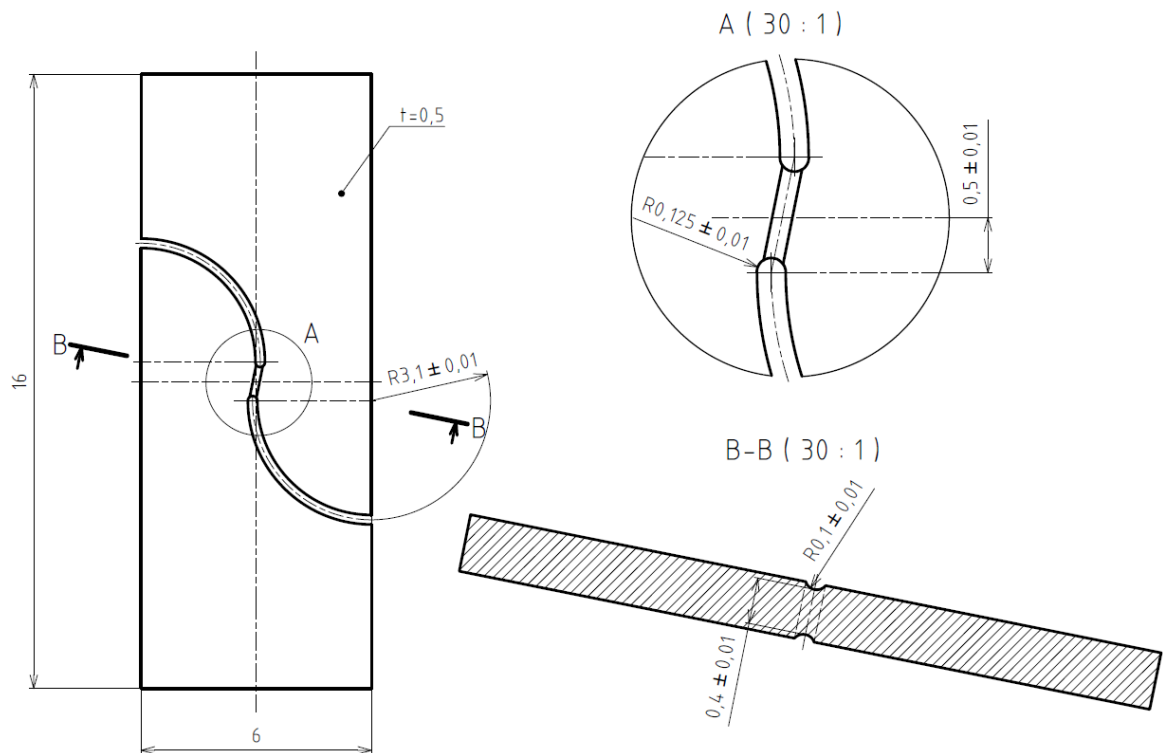


Fig. 28 Initially proposed shear specimen

The symmetry surfaces along with the predicted fracture initiation site and the nodes from which the η and ξ parameters were extracted are plotted in Fig. 29–32 for all specimens. The figures also display the detail of the elements in the critical region.

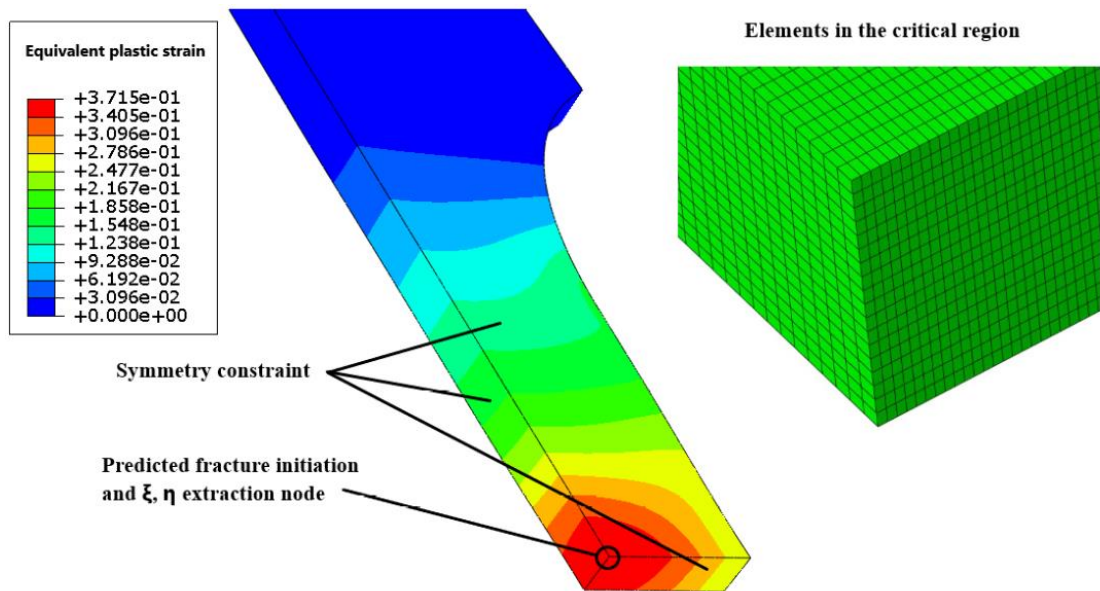


Fig. 29 Model of the uniaxial tension specimen

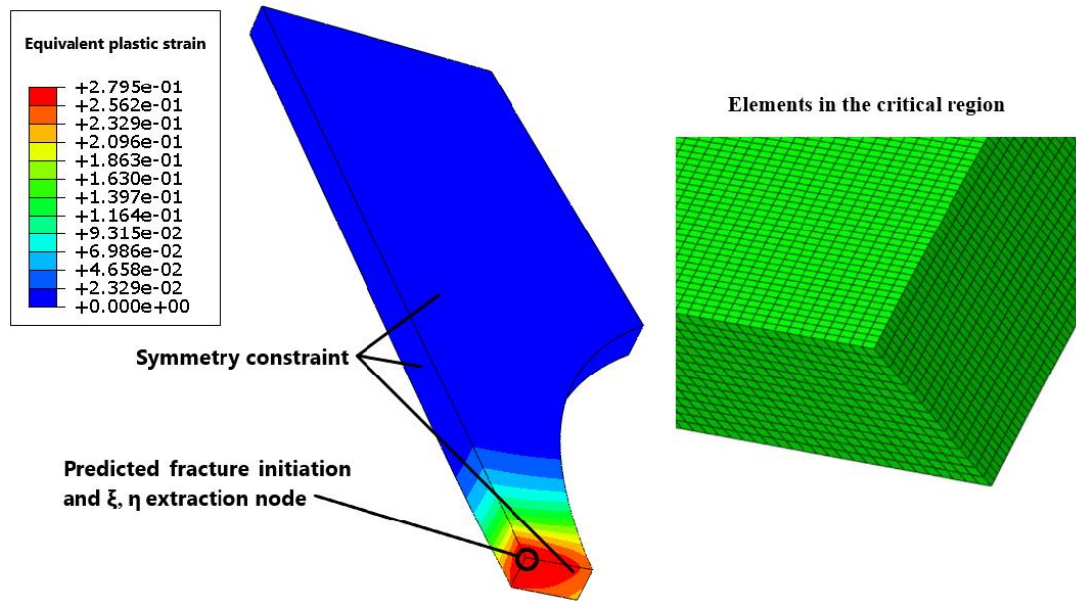


Fig. 30 Model of the notched R4 specimen

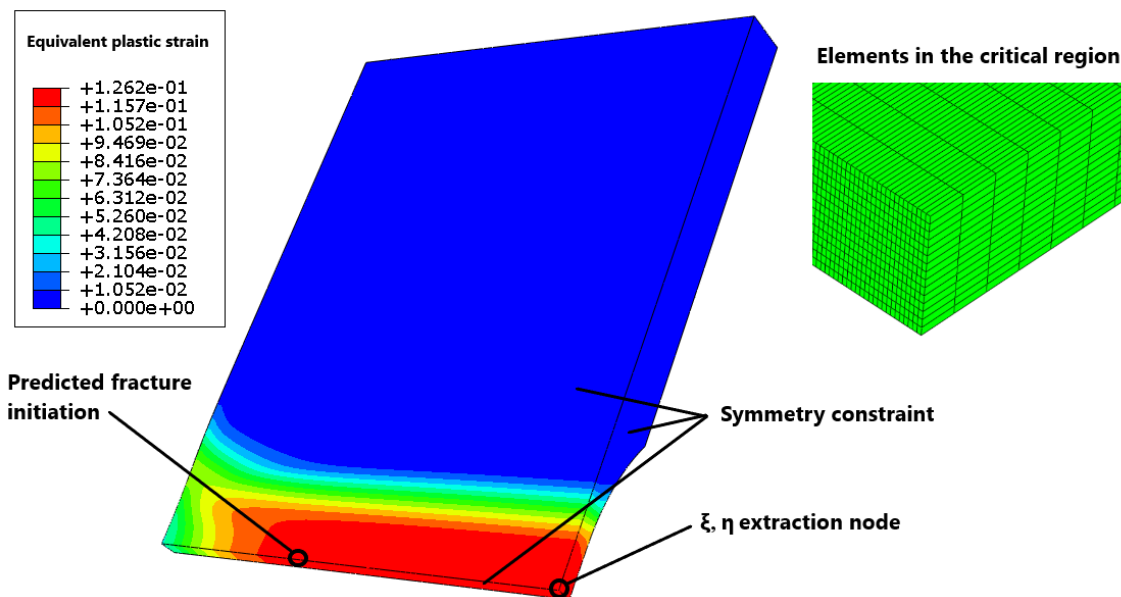


Fig. 31 Model of the plane strain specimen

The contours display an equivalent plastic strain distribution in a step prior to fracture initiation.

At the beginning of the design process, the entire geometry was modelled without any symmetry conditions to determine the location of fracture initiation and propagation, which would not be as intuitive using only part of the model. Only the geometries with the most satisfactory results were recalculated using symmetry conditions and finer mesh to increase precision. It should be noted that a mesh sensitivity analysis was conducted. The simulations were initially performed with various mesh sizes to compare the results and ensure a sufficiently fine mesh.

In the case of the uniaxial tension specimen, the fracture modelled by the FEM using the previously described material models initiated in the centre of the sample. The fracture initiated in the centre even in the case of the notched R4 specimen, although the notch formed a stress concentrator on the surface. It is due to a higher stress triaxiality in the centre of the specimen, which reduced the critical value of equivalent plastic strain required for element failure. Nevertheless, the fracture can also initiate on the surface when the notch is sharper. The critical element of the plane strain specimen was expected to be located in the centre of the sample. Numerical simulations predicted the fracture to initiate near the edges and propagate towards the centre, eventually breaking the edges. This behaviour was also observed by simulating the experiment with plane strain and flat notched specimens from various studies. Lou et al. [80] observed a similar fracture initiation site from numerical simulations of a plane strain sample using different material models. The η and ξ values were extracted from the centre of the specimen, as in the vast majority of studies, although the FEM predicted the onset of fracture at a different location. The fracture initiation location of flat samples, as predicted by numerical simulation, is inconsistent with experiments conducted by numerous researchers, including Li et al. [34], who observed the onset of fracture in the centre of the specimens. The predicted fracture initiation location and η , ξ extraction node also differed for the shear specimen. Detail of these two locations is shown in Fig. 32.

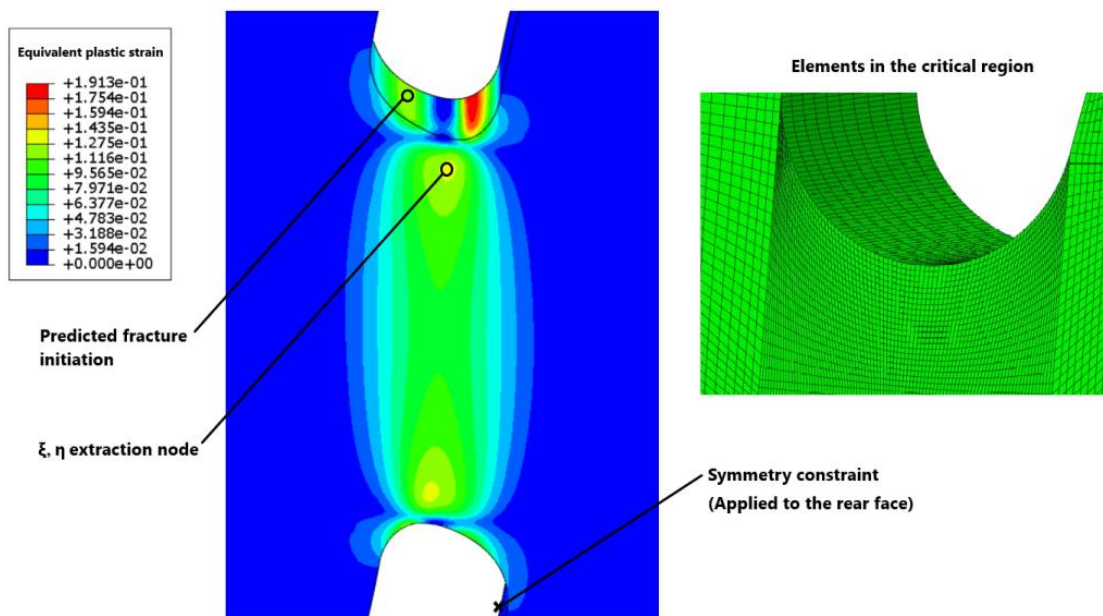


Fig. 32 Model of the shear specimen

The location at which the numerical simulations predicted the onset of fracture for the shear specimen does not exhibit a shear stress state regardless of the specimen dimensions. Therefore, some researchers have created an additional lateral groove on the sides, as illustrated in Fig. 28, to relocate the fracture initiation site. Others, including Li et al. [34], and Quach et al. [36] have extracted the η and ξ values from the centre of the shear specimen. A similar approach was used in this thesis; however, the parameters were not obtained from the centre of the sample, but from a node marked as an extraction node in Fig. 32. The node from which the stress state parameters were extracted was closer to reaching its critical value of equivalent plastic strain at the time of fracture initiation than the node

at the centre of the specimen, as shown in Table 13. Some researchers, such as Zhang et al. [81] have also used this location of the shear specimen to calibrate the material parameters.

Table 13 Parameters at different locations of the shear specimen

Label	Stress triaxiality η [-]	Normalized third invariant ξ [-]	Equivalent plastic strain $\bar{\epsilon}_p$ [-]	Fracture strain $\bar{\epsilon}_f$ [-]
1	0.553	0.280	0.122	0.122
2	-0.589	-0.133	0.191	0.483
3	-0.004	-0.018	0.131	0.248
4	-0.001	-0.005	0.094	0.246
5	-0.014	-0.059	0.099	0.256
6	-0.013	-0.056	0.089	0.255
7	-0.015	-0.064	0.093	0.257

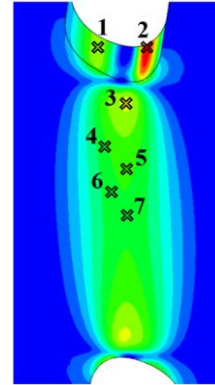


Fig. 33 Shear specimen

The stress triaxiality, normalized third invariant and equivalent plastic strain in Table 13 represent values at the moment of crack initiation. These are instantaneous values, not averages. The fracture strain represents a critical value of equivalent plastic strain at which the elements are deleted in the element deletion technique. Points 3 to 7 in Table 13 show that the values of η and ξ at various locations, through which the crack was predicted to propagate, are similar and close to the shear stress state. The contours in Fig. 33 show the distribution of $\bar{\epsilon}_p$.

The η and ξ parameters were not constant throughout the loading process. Evolution of these two parameters with increasing equivalent plastic strain is plotted in Fig. 34 and 35. The averages of the parameters (listed in Table 12) in the graphs are used to calibrate the ductile fracture criteria.

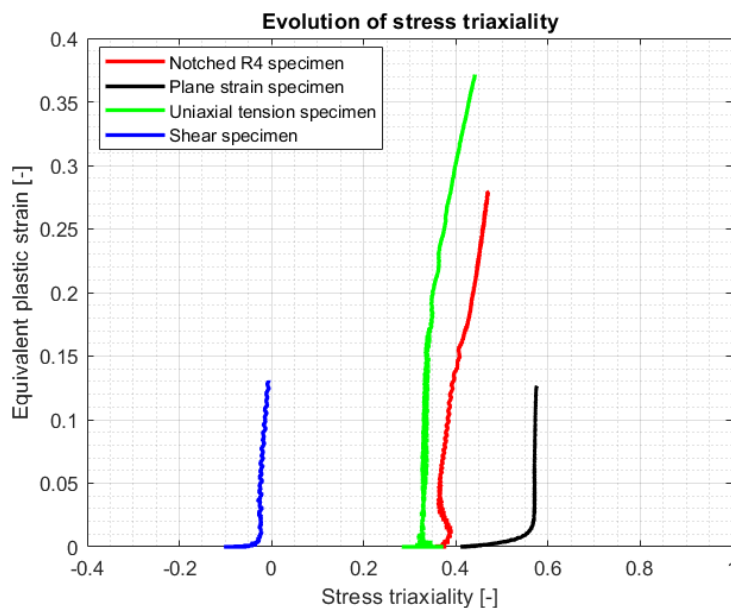


Fig. 34 Evolution of stress triaxiality

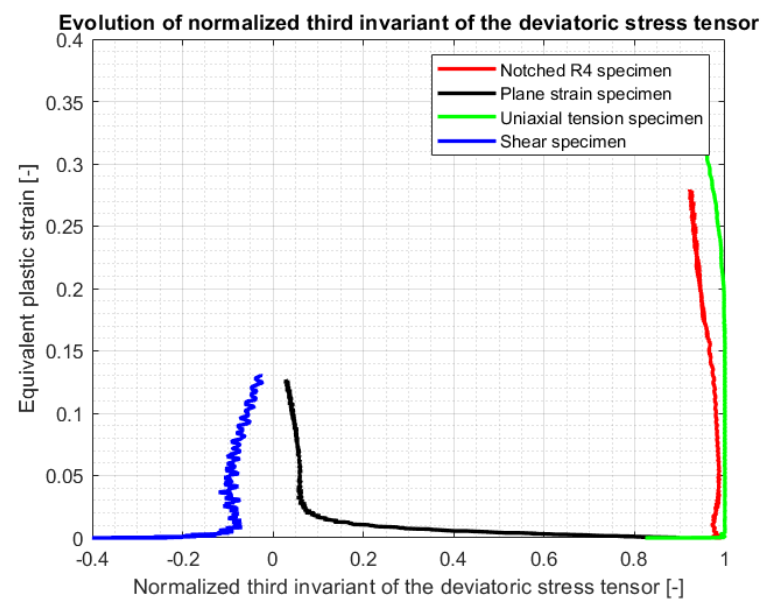


Fig. 35 Evolution of normalized third invariant of the deviatoric stress tensor

8 EXPERIMENTAL PROGRAM

8.1 ALUMINIUM ALLOY EN AW 2024-T351

Material EN AW 2024-T351 is the most widely used aluminium alloy with copper and magnesium as main additives. It is a modified variation of the EN AW 2017 alloy, which it is gradually replacing in many engineering applications. This aluminium alloy is also known as duralumin. Its main application is in the aerospace industry due to its high strength-to-weight ratio, but it is also used in other fields such as automotive, medical, military, etc. It has good fatigue resistance, fracture toughness, strength and is easy to machine. However, it has poor chemical and corrosion resistance, which can be increased by an additional coating. Its weldability is complicated. The material is referred to as AlCu4Mg1 in the ISO standard and 3.1355 in the DIN EN standard. The heat treatment corresponds to T351. The material was solution heat-treated, stress relieved, and naturally aged. The chemical composition of the supplied material has already been investigated in [73]. It was measured using glow discharge optical emission spectroscopy on a Spectrumat GDS 750. The chemical composition is listed in Table 14. [82], [83], [84], [85].

Table 14 Chemical composition of the supplied material [73]

Chemical composition weight %								
Cu	Mg	Mn	Si	Fe	Zn	Ti	Cr	Ni
4.30	1.71	0.52	0.07	0.25	0.01	0.04	0.00	0.00

8.2 TEST APPARATUS

The test apparatus for the designed miniature specimens is shown in Fig. 36. It was designed for testing of small flat samples in tension. Its main components are stepper motor, force transducer, support construction, guide rods, gripping clamps, telecentric lens, and camera for DIC. The specimens were clamped between two jaws, which were tightened by a screw. The samples were held in the grips through friction. The lower grip was attached to HBM S2M/1000N force transducer and remained stationary throughout the experiment. The measurement range of the force transducer was up to 1000 N. The upper grip was driven by a two-phase MDrive 23 Plus stepper motor with microstepping and guided by the guide rods. A screw mechanism was used to convert rotary motion of the drive into translational motion of the grips. The maximum force was dependent on the supply voltage. It was limited to 775 N. The upper force limit of the designed specimens was 500 N to ensure rupture of the specimens using this device. All components were attached to a robust tool steel support construction. The test apparatus was controlled by a program written in Python, which allowed the samples to be loaded by displacement at a constant speed. The program was linked with the Alpha 2.1.27 DIC software developed by X-Sight. This connection enabled to start the DIC and force measurement simultaneously with the same sampling frequency. A CMOS camera FLIR Blackfly® S with the telecentric lens AZURE-6505THM was used for the DIC measurements. The camera was positioned at the rear and mounted

on a plastic holder printed by a 3D printer. Lightning was provided by a CLD-01 light source. [86], [87].

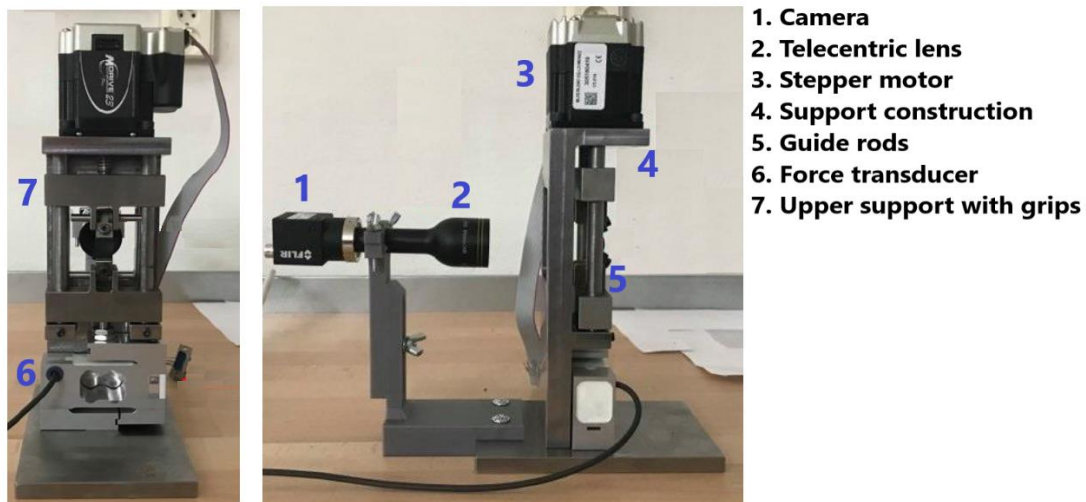


Fig. 36 Test apparatus [86]

8.3 SPECIMEN PREPARATION

The material for the samples was supplied by Ferropol as a cold-rolled plate. The plate was cut into smaller pieces using a water jet. The material was then milled to the required contour with an increased thickness for each specimen type. In the case of the shear sample, the grooves R3.1 were subsequently cut using a wire electrical discharge machine (EDM) CHMER G32S. The semi-finished samples were then cut to the specified thickness using the EDM. All the specimens were produced from the same metal plate to ensure identical microstructure of the samples. The orientation of the specimens relative to the rolling (L) axis is shown in Fig. 37. The manufactured specimens are shown in Fig. 38. The specimens, except for the plane stain specimen, already had a high contrast speckle pattern on the face surfaces after EDM. Therefore, the speckle pattern had to be applied only to the plane stain specimens.

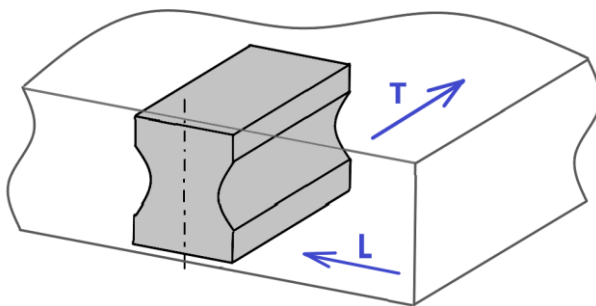


Fig. 37 Orientation of the samples relative to the rolling direction

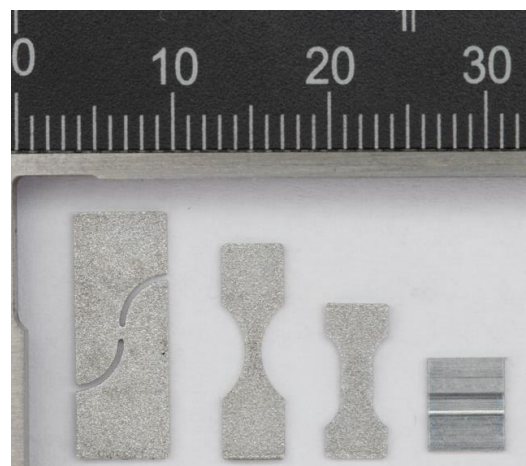


Fig. 38 Designed specimens

The grain size was approximately 0.2 mm in the L direction and 0.05 mm in the T direction. The estimated number of grains in these directions for each specimen are listed in Table 15.

Table 15 Estimated number of grains

Specimen	Estimated number of grains in the L direction	Estimated number of grains in the T direction
Uniaxial tension	10	9
Notched R4	5	9
Plane strain	1	100
Shear stress	30	9

The results are expected to be influenced to some extent by the size effect, particularly for the plane strain specimen, as it contains only a single grain in the L direction. In general, the size effect becomes significant when the samples have less than 10 grains over the thickness. [19].

8.4 EXPERIMENTS

First, DIC calibration was performed. The DIC was calibrated only once, and the same setting was used for all experiments. The accuracy of the force transducer was checked before the experiments using a plate of known weight. In addition, the guide rods have been lubricated for smoother motion. The thickness of each specimen was measured with a micrometer prior to the experiments as the thickness of the specimens had a large scatter and differed significantly from the designed dimension. The specimens were then gripped in the test apparatus. The handles could rotate around a transverse axis relative to the loading direction. Therefore, increased attention was paid during gripping to avoid damaging the samples during this process. Subsequently, a line probe was added in the X-Sight Alpha software to the centre of the specimen with a different gauge length for each specimen. Then, the lightning intensity was adjusted. All specimens were loaded until rupture at a constant rate of 0.05 mm/min, which was close to the minimum speed allowed by the testing device.

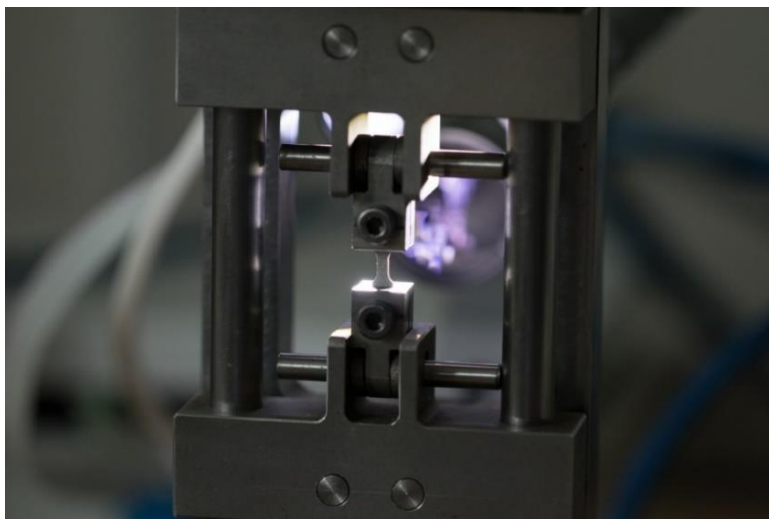


Fig. 39 Detail of the test apparatus

8.4.1 EXPERIMENTS OF THE NOTCHED SPECIMENS

A total of ten experiments with the notched specimens were performed. However, only nine of the measurements were used for the evaluation of the results. One experiment was excluded due to its high discrepancy from the remaining responses. The average thickness was 0.463 mm. The experimentally measured force–displacement curves are shown in Fig. 40 together with the averaged response. The displacement in the figure refers to the displacement of the DIC probe placed in the centre of the specimen with a gauge length of 2 mm. The experiments were simulated in Abaqus/Explicit using the average thickness. The mesh size, time scaling, mass scaling, and material parameters used were the same as in the design process. This also applies to shear, plane strain, and uniaxial specimen simulations. The response obtained from the simulation is plotted in the same figure as the experimental measurements. The displacement in the simulation was taken from the same location where the probe was positioned during the experiments. The simulation was carried out without implementing the ductile fracture criteria and the force–displacement curve was plotted up to the averaged experimentally determined fracture displacement, which was 0.137 mm.

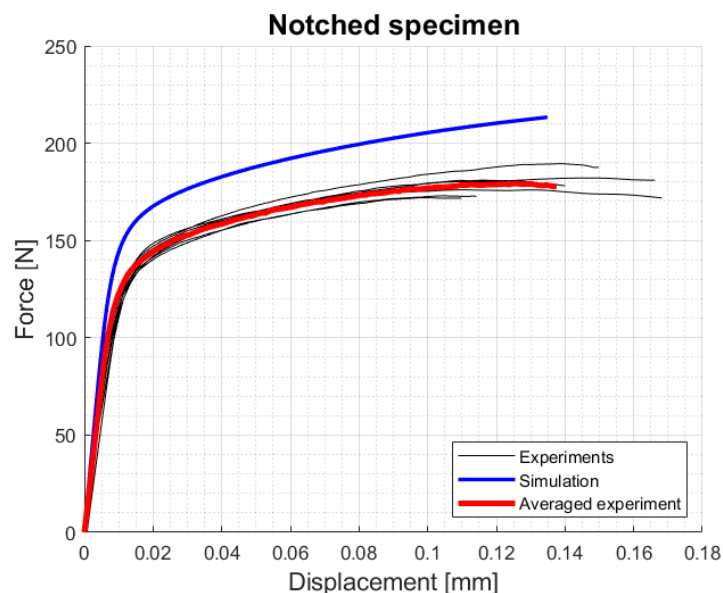


Fig. 40 Force–displacement responses of the notched specimens

The experimentally measured force had only a minor scatter in the data. The yield stress, elastic, and plastic behaviours of each specimen were also similar. However, the displacement at which the specimens ruptured varied significantly. It ranged from 0.11 to 0.17 mm. The difference between simulations and experiments was large, although the elastic and plastic material parameters of the plate sheet from which the specimens were fabricated have been investigated in the past. However, the material parameters used were investigated for a different grain direction, which plays an important role in the force–displacement response. Therefore, before extracting the calibration points for the ductile fracture criteria calibration from the numerical models, it would be required to recalibrate the material parameters to match the experimentally obtained responses. The elastic and plastic behaviour obtained from the simulation and experiments is similar; however, they differ significantly in the yield stress, which was predicted to be higher by the numerical simulations.

8.4.2 EXPERIMENTS OF THE SHEAR SPECIMENS

The shear specimens were measured and evaluated in the same way as the notched specimens. A total of ten measurements with the shear specimens were performed, of which one with the largest deviation was excluded from the evaluation. The average thickness was 0.465 mm. The gauge length of the DIC probe was 6 mm. The measured responses along with the averaged and simulated responses are plotted in Fig. 41.

The measured force–displacement evolution was similar for all experiments. However, the fracture displacement varied significantly between samples, as in the case of the notched specimens. The fracture displacement ranged from 0.20 to 0.27 mm, with an average of 0.23 mm. The numerical simulations again highly overestimated the force response. In this case, the elastic behaviour and the yield stress were similar to the experiments. However, the simulation predicted greater plastic hardening than was observed in reality.

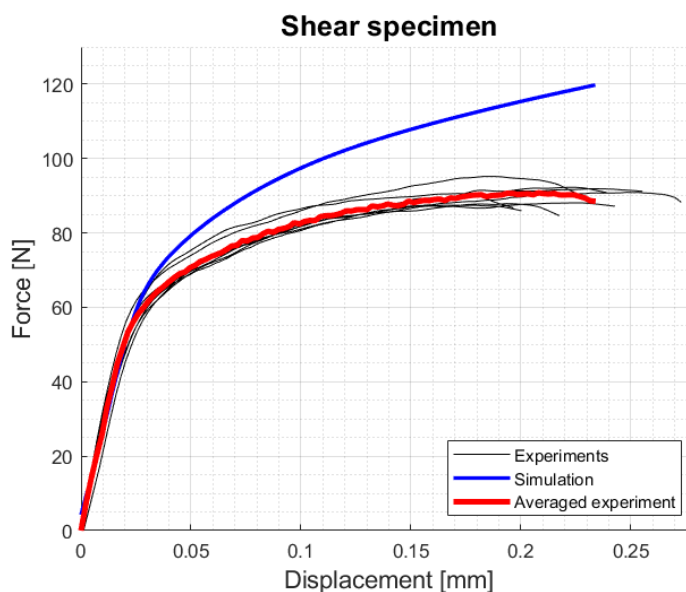


Fig. 41 Force–displacement responses of the shear specimens

8.4.3 EXPERIMENTS OF THE PLANE STRAIN SPECIMENS

The evaluation was carried out using six measurements of the plane strain specimens, as only a small number of these specimens were manufactured. The average thickness measured with a caliper was 5.03 mm. The displacement was monitored using a DIC probe with a gauge length of 2.5 mm. The force–displacement curves obtained from the experiments and simulation are plotted in Fig. 42.

In this case, the elastic response of the individual specimens did not match, in contrast to the measurements performed with the notched and shear samples. This scatter in the data may have been caused by damaging the samples during the gripping process, as the thickness in the central region was only 0.2 mm and the grips were not ideal for testing such fragile samples. However, it is not certain whether this has been the case or whether the responses were influenced by other factors since special attention was paid to the clamping process. All plane strain specimens had a similar maximum force with minimal scatter. The samples exhibited no hardening once a certain threshold was reached. The elongation of the probe at the moment of fracture ranged from 0.060 to 0.085 mm with an average of 0.070 mm. The force–displacement curve obtained from the numerical simulation using the provided

material parameters did not match the experimentally obtained responses in either the elastic or plastic parts. The simulation once again predicted a higher force with increasing elongation.

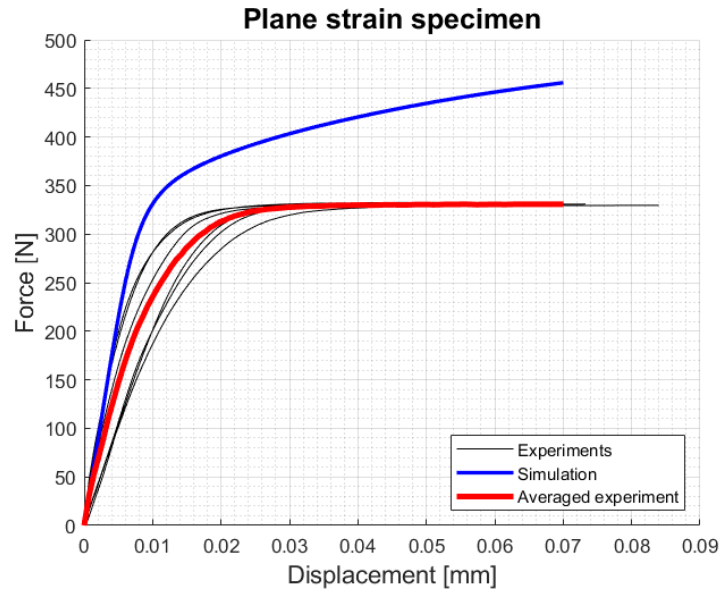


Fig. 42 Force–displacement responses of the plane strain specimens

8.4.4 EXPERIMENTS OF THE UNIAXIAL SPECIMENS

The last specimen that has been experimentally tested in this thesis is the uniaxial specimen. The average experimental response was evaluated based on ten measurements, which are plotted in Fig. 43. The DIC probe gauge length was set to 4 mm. The average thickness of the specimens was 0.465 mm.

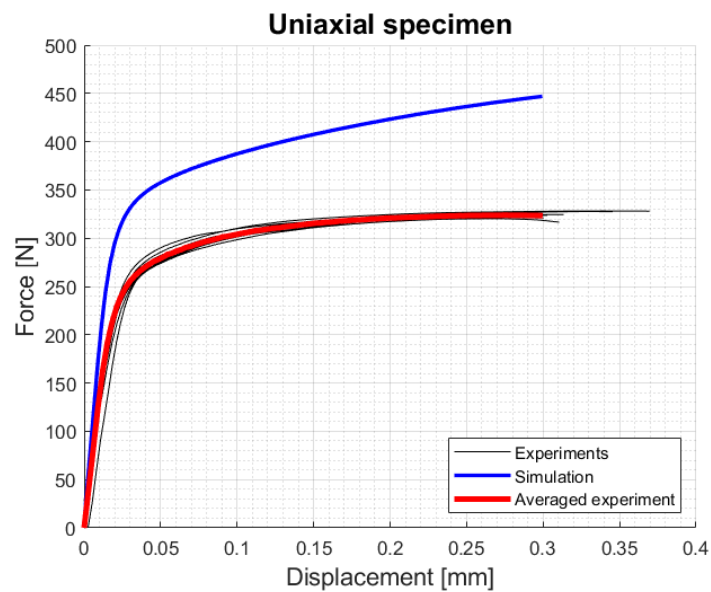


Fig. 43 Force–displacement responses of the uniaxial specimens

All experimental responses of the uniaxial specimen were almost identical in both the elastic and plastic regions. However, the fracture elongation of the gauge length varied between experiments. The average was 0.30 mm with a minimum of 0.25 mm and a maximum of 0.37 mm. The specimens fractured at an average force of 323 N, which is inconsistent with the simulation in which the predicted maximum force was 447 N. The predicted yield force and plastic hardening were also higher, as for the other specimen types.

8.4.5 SUMMARY OF THE EXPERIMENTS

The numerical simulations for all four proposed specimen geometries predicted significantly higher forces with increasing elongation than what was observed in the experiments. The discrepancy between the simulation and the experiments is considered to be mainly due to material anisotropy and size effect, as the material parameters were investigated for a different grain orientation than was used in the experiments. However, this does not invalidate any of the previous results. The stress state parameters at the fracture initiation site are expected to be similar to those listed in Table 12, regardless of the inconsistency with the experiments. It mainly affects the fracture strain, which would be determined in the following steps. The results indicate that the used bulk of material is highly anisotropic, and further investigation of the material parameters is required before extracting the calibration points from the numerical simulations to calibrate the ductile fracture criteria based on the miniature specimens. Additional discrepancies between simulation and experiments, besides anisotropy and size effect, may be caused by sample damage during gripping, manufacturing imperfections, dimension deviation, numerical errors, and measurement inaccuracies. However, neither of these effects can currently be quantified based on the obtained results. A more detailed description of further steps for the ductile fracture calibration is summarised in the final chapter titled Conclusion and suggestions for future studies. Ruptured specimens are displayed in Fig. 44.



Fig. 44 Tested specimens

8.4.6 SMALL PUNCH TEST

An additional miniature test used to capture $\xi = -1$, which was not covered by the four designed samples, is the SPT. The specimen for this experiment was designed and experimentally tested by Šebek et al. [72]. The initial principal stresses at the apex are $\sigma_1 = \sigma_2 > 0$ and $\sigma_3 = 0$, resulting in $\eta = 2/3$ and $\xi = -1$. [72].

The specimens were cut from a cylindrical rod with a roughness of $R_a = 0.4 \text{ mm}$ using an EDM. These samples initially had a diameter of $8 \pm 0.02 \text{ mm}$ and a thickness of $0.6 \pm 0.02 \text{ mm}$, which were subsequently ground and polished to a thickness of $0.5 \pm 0.005 \text{ mm}$. The samples were punched in an SPT apparatus using a cemented carbide ball with a diameter of 2.5 mm as a tool. The testing was carried out using a Zwick Z250 Allround-line, tCII, and a Zwick multiXtens extensometer. The force–displacement relationship was obtained from the experiment. [72].

The experiment was simulated using the material models presented in chapter 5, excluding the ductile fracture criteria, as element removal was not desired in this case. The sample was meshed using four-node bilinear axisymmetric quadrilateral elements with reduced integration formulation and hourglass control (CAX4R). The sample mesh size was $0.008 \times 0.008 \times 0.008 \text{ mm}$. All other parts were meshed using a two-node linear axisymmetric rigid link (RAX2) with a global element size of 0.03 mm . All components of the test apparatus that came into contact with the sample were included in the numerical model. The friction coefficient was set to 0.1 as in the original article [72]. The displacement of the tool at which fracture initiation occurred during the experiment, determined from the force–displacement response, was used as input to the numerical simulation. The values of η , ξ and $\bar{\varepsilon}_f$ were extracted at this displacement. The η and ξ parameters were averaged using the same functions and trapezoidal numerical integration as used in the design process of the proposed samples. The force–displacement response obtained from the numerical simulation is plotted alongside the experimental response in Fig. 45.

The force–displacement response calculated from the numerical simulation was not consistent with the response obtained from the experiment. The material parameters in the provided VUMAT subroutine have been calibrated using several different macroscopic samples. The SPT was not part of the calibration process. The material properties of a small punch specimen can vary locally, which affects the experimental results and increases the discrepancy between the simulation and the experiments. This is a complication for all small samples. Additional deviations between experiments and simulations can be caused by material anisotropy, clamping clearances, sample damage during the manufacturing or handling process, and material calibration errors. [72].

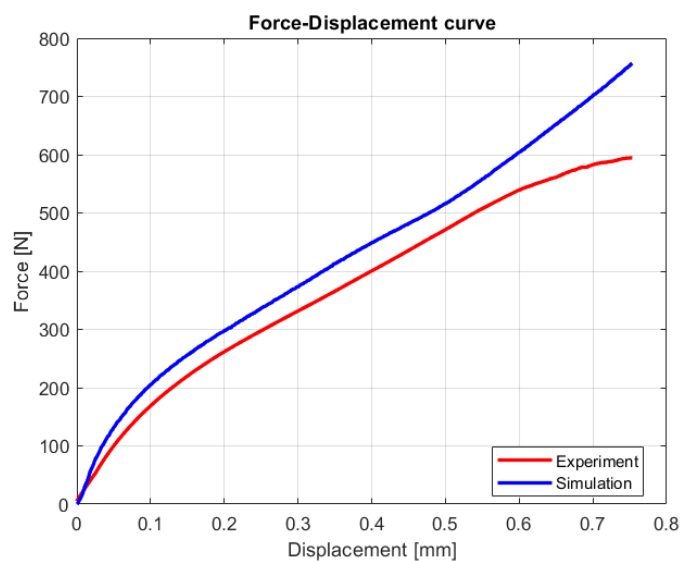


Fig. 45 Force–displacement response of the SPT

The numerical model, along with the node that was used to derive the fracture strain and stress parameters (indicated by the red circle), is shown in Fig. 46. The contours display an equivalent plastic strain distribution. The geometry was modelled using axisymmetry to reduce computation time. The computational time was further reduced by using a simulation time of 0.1 s and mass scaling with a target time increment of $5 \cdot 10^{-7}$ s, which was the same time and mass scaling that was used for all the numerical simulations performed in this thesis. Mesh sensitivity and comparison of kinetic to internal energy were checked. Fig. 47 shows the model of the test rig.

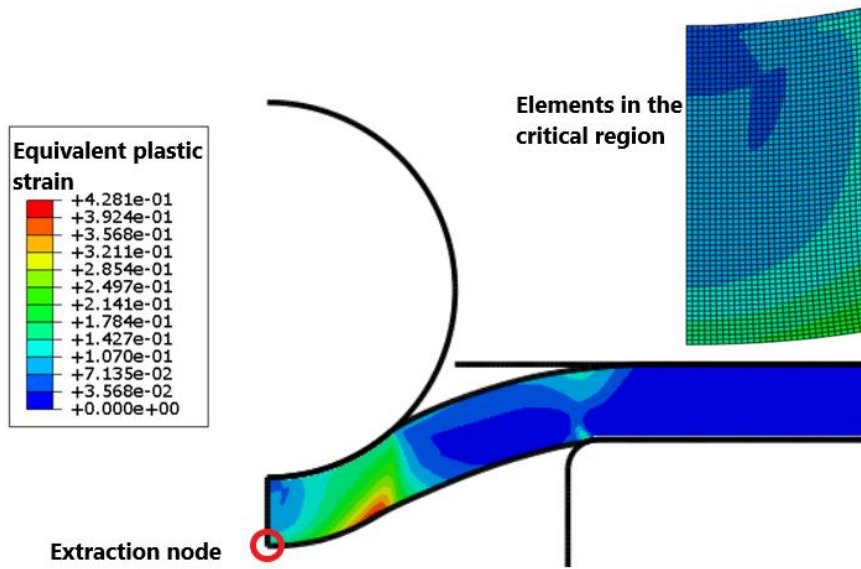


Fig. 46 Model of the SPT

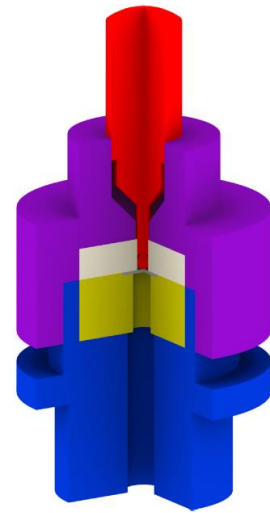


Fig. 47 SPT test apparatus [72]

CONCLUSION AND SUGGESTIONS FOR FUTURE STUDIES

This thesis dealt with the calibration of the ductile fracture criteria and the design of miniature specimens for an already constructed test rig. The specimens were designed in Abaqus/Explicit using the calibrated ductile fracture criteria and other already calibrated material models provided by the supervisor.

A total of four ductile fracture criteria called the modified Mohr–Coulomb, Ganjiani, KHPS2 and Lou–Huh have been examined and calibrated based on macroscopic specimens. The calibration was performed using an artificial intelligence-based method called particle swarm optimization, since the least squares method was not ideal for this task as it is strongly affected by local minima and initial estimation of material constants. The lowest calibration error of the four mentioned ductile fracture criteria was obtained by the KHPS2 criterion. This criterion also predicted a reasonable cut-off stress triaxiality, unlike the modified Mohr–Coulomb and Lou–Huh models. KHPS2 was used for the numerical simulations, due to the lowest calibration error, which was more than twice as low compared to the other criteria.

Four miniature specimens designed for the calibration of the ductile fracture criteria have been proposed. These specimens were designed using numerical simulations and material models calibrated by macroscopic samples. The proposed specimens, together with an additional SPT specimen, cover a wide range of stress states, which is essential for proper calibration. The stress states in the critical node of each specimen were similar to those in other studies, although the geometry and dimensions were restricted for easier fabrication. The specimens were made of aluminium alloy 2024-T351. They were experimentally tested until rupture at a rate of 0.05 mm/min to obtain a force–displacement response. The force was measured by a force transducer and the displacement was evaluated by DIC. Finally, the experiments were simulated and compared to the experimental response.

Calibration of the elastic and plastic material parameters was carried out for a grain orientation different from that of the tested samples. Therefore, the numerical simulations were not consistent with the experiments due to a strong anisotropy of the material and possible size effect. The simulations highly overestimated the force–displacement response. Currently, it is not possible to determine the effect of miniaturization from the obtained results. The effect of anisotropy must be eliminated first. This would require a recalibration of the material parameters for proper grain orientation based on macroscopic samples. The size effect can then be observed in the force–displacement curves obtained from experiments and simulations, although this would also be strongly influenced by many other factors, such as imperfections and residual stresses. The suitability of miniature samples for the ductile fracture calibration can be determined by fitting the experimentally measured curves to obtain the same responses from the simulations. Only then it is possible to extract the calibration points from the numerical simulations and calibrate the ductile fracture criteria using the proposed miniature samples. The suitability of the miniature specimens for the calibration of the ductile fracture criteria can then be assessed by comparing the fracture envelopes calibrated by macro and the proposed specimens. Another alternative to the fracture envelope comparison consists of recalibrating the material parameters based on the experimental results and performing an application test on normal-sized samples. This has yet to be done in future studies because without either of these steps, it is not possible to draw a clear conclusion as to whether the miniature samples were affected by the size effect or whether they represented a valid alternative to macroscopic samples.

The testing of small samples proved to be feasible and worth addressing in future studies as it requires only a small amount of material, which is a significant advantage over the normal-sized specimens for some applications, despite the complicated manufacturing process and greater potential for error.

REFERENCES

- [1] XUE, L. *Ductile fracture modeling – theory, experimental investigation and numerical verification*. Massachusetts, 2007. PhD Thesis. Massachusetts Institute of Technology. Supervisor T. WIERZBICKI.
- [2] KUMAR, D. A. *Brittle fracture and ductile fracture: definition, mechanism, differences* [online]. 2021 [cit. 2022-09-23]. Available from: <https://whatispiping.com/brittle-fracture-ductile-fracture>
- [3] MACKENZIE, D. S. *Four basic types of fracture mechanisms* [online]. 2020 [cit. 2022-09-23]. Available from: <https://gearsolutions.com/departments/hot-seat/four-basic-types-of-fracture-mechanisms>
- [4] *Fracture of materials* [online]. EN380 Naval Materials Science and Engineering Course Notes, U.S. Naval Academy, Chapter 11, 1–19 [cit. 2022-09-23]. Available from: https://www.usna.edu/NAOE/_files/documents/Courses/EN380/Course_Notes/Ch11_Fracture.pdf
- [5] *Ductile material – ductile fracture* [online]. Nuclear-Power [cit. 2022-09-23]. Available from: <https://www.nuclear-power.com/nuclear-engineering/materials-science/material-properties/toughness/ductile-material-ductile-fracture>
- [6] *Brittle and ductile fracture* [online]. Yena Engineering [cit. 2022-09-23]. available from: <https://yenaengineering.nl/brittle-and-ductile-fracture>
- [7] GARRISON, W. M. and N. R. MOODY. Ductile fracture. *Journal of Physics and Chemistry of Solids*. 1987, **48**(11), 1035–1074.
- [8] KWON, D. and R. J. ASARO. A study of void nucleation, growth, and coalescence in spheroidized 1518 steel. *Metallurgical Transactions A*. 1990, **21**(1), 117–134.
- [9] KOSSAKOWSKI, P. G. Influence of initial porosity on strength properties of S235JR steel at low stress triaxiality. *Archives of Civil Engineering*. 2012, **58**(3), 294–307.
- [10] RAN, J., M. W. FU and W. L. CHAN. The influence of size effect on the ductile fracture in micro-scaled plastic deformation. *International Journal of Plasticity*. 2013, **41**, 65–81.
- [11] XU, Z., L. PENG, X. M. LAI and M. W. FU. Geometry and grain size effects on the forming limit of sheet metals in micro-scaled plastic deformation. *Materials Science and Engineering A*. 2014, **611**, 345–353.
- [12] FU, M. W. and W. L. CHAN. Geometry and grain size effects on the fracture behavior of sheet metal in micro-scale plastic deformation. *Materials and Design*. 2011, **32**(10), 4738–4746.
- [13] LAI, X., L. PENG, P. HU, S. LAN and J. NI. Material behavior modelling in micro/meso-scale forming process with considering size/scale effects. *Computational Materials Science*. 2008, **43**(4), 1003–1009.

- [14] RAULEA, L. V., A. M. GOIJAERTS, L. E. GOVAERT and F. P. T. BAAIJENS. Size effects in the processing of thin metal sheets. *Journal of Materials Processing Technology*. 2001, **115**(1), 44–48.
- [15] WANG, J., M. W. FU and S. Q. SHI. Influences of size effect and stress condition on ductile fracture behavior in micro-scaled plastic deformation. *Materials and Design*. 2017, **131**(2), 69–80.
- [16] KUMAR, K., A. POOLEERY, K. MADHUSOODANAN, R. N. SINGH, J. K. CHAKRAVARTTY, B. K. DUTTA and R. SINHA. Use of miniature tensile specimen for measurement of mechanical properties. *Procedia Engineering*. 2014, **86**, 899–909.
- [17] RABENBERG, E. M. *Small specimen test techniques for evaluating radiation-induced changes in mechanical properties*. Boise, 2012. PhD Thesis. Boise State University. Supervisor D. P. BUTT.
- [18] KARTHIK, S. V. *Development of Miniature Specimen Test Techniques* [online]. Technology-13, 194–195 [cit. 2022-10-04]. Available from: <http://www.igcar.gov.in/benchmark/Tech/13-tech.pdf>
- [19] ZHANG, L., H. WILL, M. A. YAR, S. G. R. BROWN and N. P. LAVERY. The development of miniature tensile specimens with non-standard aspect and slimmness ratios for rapid alloy prototyping processes. *Journal of Materials Research and Technology*. 2021, **15**, 1830–1843.
- [20] ARUNKUMAR, S. Overview of Small Punch Test. *Metals and Materials International*. 2019, **26**(12), 719-738.
- [21] HAFEEZ, F. and A. HUSAIN. Standardization of diminutive specimen testing techniques for predicting the mechanical properties of metals. *AIP Conference Proceedings*. 2019, **2148**(1), 1–10.
- [22] BASARAN, M. *Stress State Dependent Damage Modeling with a Focus on the Lode Angle Influence*. Germany, 2011. PhD Thesis. Aachen Technical University. Supervisor D. WEICHERT.
- [23] JÍRA, J. *Introduction to the theory of elasticity* [online]. University of Technology Prague, 2011, Chapter 5, [cit. 2022-09-28]. Available from: http://mech.fd.cvut.cz/members/jira/studijni-podklady/ptp-plasticita-a-teorie-poruseni/K5_zakladymatempruznosti.pdf
- [24] *Plasticity review* [online]. Chapter 2, 5–13 [cit. 2022-09-28]. Available from: https://thesis.library.caltech.edu/1929/4/03_Chapter_2.pdf
- [25] KELLY, P. *Solid mechanics part II: engineering solid mechanics – small strain* [online]. Chapter 8.2, 252–258 [cit. 2022-09-28]. Available from: https://pkel015.connect.amazon.auckland.ac.nz/SolidMechanicsBooks/Part_II/index.html
- [26] THOMPSON, E. *The J2 invariant* [online]. Colorado State University, Department of Civil engineering. 2000 [cit. 2022-09-28]. Available from: https://www.engr.colostate.edu/~thompson/hPage/CourseMat/Tutorials/Solid_Mechanics/J2.pdf

- [27] KIM, N. H. *FEA for elastoplastic problems* [online]. Chapter 4, 1–162 [cit. 2022-09-28]. Available from: <https://mae.ufl.edu/nkim/egm6352/Chap4.pdf>
- [28] NEŽERKA, V. *Micromechanics and homogenization: materials containing coated and uncoated spherical inhomogeneities*. Prague, 2012. Master's Thesis. University of Technology Prague. Supervisor J. ZEMAN.
- [29] ŠEBEK, F. *Ductile fracture criteria in multiaxial loading: theory, experiments and application*. Brno, 2016. PhD Thesis. University of Technology Brno. Supervisor J. PETRUŠKA.
- [30] CORONA, E. and B. REEDLUNN. *A Review of macroscopic ductile failure criteria* [online]. 2013, 1–74 [cit. 2023-09-23]. Available from: <https://www.osti.gov/servlets/purl/1096245>
- [31] *The equations for isotropic von Mises plasticity* [online]. LS-DYNA Support, 2005 [cit. 2022-10-02]. Available from: <https://www.dynasupport.com/tutorial/computational-plasticity/the-equations-for-isotropic-von-mises-plasticity>
- [32] SÁNCHEZ-CARRILERO, M., M. Á. ALCÓN, P. MAYUET, Á. GÓMEZ-PARRA and M. MARCOS-BÁRCENA. Matrix stress-strain working method for determining the effective plastic strain. *Procedia Engineering*. 2015, **132**, 381–388.
- [33] BAI, Y. and T. WIERZBICKI. Application of extended Mohr–Coulomb criterion to ductile fracture. *International Journal of Fracture*. 2010, **161**(1), 1–20.
- [34] LI, W., F. LIAO, T. ZHOU and H. ASKES. Ductile fracture of Q460 steel: Effects of stress triaxiality and Lode angle. *Journal of Constructional Steel Research*. 2016, **123**, 1–17.
- [35] YAN, S. and X. ZHAO. A fracture criterion for fracture simulation of ductile metals based on micro-mechanisms. *Theoretical and Applied Fracture Mechanics*. 2018, **95**, 127–142.
- [36] QUACH, H., J. J. KIM, D. T. NGUYEN and Y. S. KIM. Uncoupled ductile fracture criterion considering secondary void band behaviors for failure prediction in sheet metal forming. *International Journal of Mechanical Sciences*. 2020, **169**, 1–17.
- [37] BAI, Y. *Effect of loading history on necking and fracture*. Massachusetts, 2008. PhD Thesis. Massachusetts Institute of Technology. Supervisor T. WIERZBICKI.
- [38] BAI, Y. and T. WIERZBICKI. A new model of metal plasticity and fracture with pressure and Lode dependence. *International Journal of Plasticity*. 2008, **24**(6), 1071–1096.
- [39] MU, L., Y. WANG, Y. ZANG and P. M. STEMLER. Edge fracture prediction using uncoupled ductile fracture models for DP780 sheet. *Journal of Failure Analysis and Prevention*. 2017, **17**(2), 322–329.

- [40] BRITEZ, D., S. WERDA, R. LAHEURTE, P. DARNIS and O. CAHUC. A comparison of different hardening rules on a multi-step global manufacturing process modeling. *ESAFORM 2021 - 24th International Conference on Material Forming*. 2021.
- [41] DVOŘÁK, P. *Methods of determination of the Young's modulus*. Prague, 2018. Bachelor's Thesis. University of Technology Prague. Supervisor F. TATÍČEK.
- [42] GORJI, M. B. and D. MOHR. Micro-tension and micro-shear experiments to characterize stress-state dependent ductile fracture. *Acta Materialia*. 2017, **131**(6), 65–76.
- [43] HŮLKA, J. *Computational prediction of ductile fracture: Short version of PhD Thesis*. Brno, 2014. PhD Thesis. University of Technology Brno. Supervisor J. PETRUŠKA.
- [44] YAO, D., S. PU, M. LI, Y. GUAN and Y. DUAN. Parameter identification method of the semi-coupled fracture model for 6061 aluminium alloy sheet based on machine learning assistance. *International Journal of Solids and Structures*. 2022, **254–255**, 111823.
- [45] JIROUŠEK, O. *Theoretical and applied mechanics* [online]. University of Technology Prague [cit. 2022-09-26]. Available from: http://kapradi.fd.cvut.cz/myPHP/lectures/18TAM/05_prostor_napeti_podminka_plasticity.pdf
- [46] HILL, R., E. H. LEE and S. J. TUPPER. The theory of combined plastic and elastic deformation with particular reference to a thick tube under internal pressure. *Proceedings of the Royal Society of London, Series A, Mathematical and Physical Sciences*. 1947, **191**, 278–303.
- [47] PETRUŠKA, J. *FEM in engineering calculations II: Plasticity* [online]. University of Technology Brno [cit. 2022-10-06]. Available from: https://moodle.vut.cz/pluginfile.php/392841/mod_resource/content/1/P2%20Plasticita%20-%20C3%BAvod.pdf
- [48] SINGULANI, PI. A. *Advanced methods for mechanical analysis and simulation of through Silicon Vias*. Wien, 2014. PhD Thesis. University of Technology Wien. Supervisor S. SELBERHERR.
- [49] SAFAEI, M., M. G. LEE, S. L. ZANG and W. D. WAELE. An evolutionary anisotropic model for sheet metals based on non-associated flow rule approach. *Computational Materials Science*. 2014, **81**, 15–29.
- [50] WIERZBICKI, T. *Structural mechanics* [online]. [cit. 2022-09-26]. Available from: [https://eng.libretexts.org/Bookshelves/Mechanical_Engineering/Structural_Mechanics_\(Wierzbicki\)](https://eng.libretexts.org/Bookshelves/Mechanical_Engineering/Structural_Mechanics_(Wierzbicki))
- [51] XIANG, Y. and J. J. VLASSAK. Bauschinger effect in thin metal films. *Scripta Materialia*. 2005, **53**(2), 177–182.
- [52] MALCHER, L., F. PIRES, and J. C. SÁ. An assessment of isotropic constitutive models for ductile fracture under high and low stress triaxiality. *International Journal of Plasticity*. 2012, **30–31**, 81–115.

- [53] LEMAITRE, J. Coupled elasto-plasticity and damage constitutive equations. *Computer Methods in Applied Mechanics and Engineering*. 1985, **51**(1–3), 31–49.
- [54] RAVINDRAN, S. *Prediction of material damage in orthotropic metals for virtual structural testing*. Cranfield, 2010. PhD Thesis. Cranfield University. Supervisor J. CAMPBELL.
- [55] KACHANOV, L. M. Rupture time under creep conditions. *International Journal of Fracture*. 1999, **97**, 26–31.
- [56] TSILOUFAS, S. P. and R. L. PLAUT. Ductile fracture characterization for medium carbon steel using continuum damage mechanics. *Materials Sciences and Applications*. 2012, **3**(11), 745–755.
- [57] CELENTANO, D. J. and J. L. CHABOCHE. Experimental and numerical characterization of damage evolution in steels. *International Journal of Plasticity*. 2007, **23**(10–11).
- [58] KUBÍK, P., F. ŠEBEK and J. PETRUŠKA. Notched specimen under compression for ductile failure criteria. *Mechanics of Materials*. 2018, **125**, 94–109.
- [59] GAO, J., T. HE, Y. HUO, M. SONG, T. YAO and W. YANG. Comparison of modified Mohr–Coulomb model and Bai–Wierzbicki model for constructing 3D ductile fracture envelope of AA6063. *Chinese Journal of Mechanical Engineering*. 2021, **34**(1), 1–25.
- [60] LI, H., M. W. FU, J. LU and H. YANG. Ductile fracture: experiments and computations. *International Journal of Plasticity*. 2011, **27**(2), 147–180.
- [61] COCKROFT, M. G. and D. J. LATHAM. Ductility and the workability of metals. *Journal of the Institute of Metals*. 1968, **96**, 33–39.
- [62] LOU, Y. and H. HUH. Evaluation of ductile fracture criteria in a general three-dimensional stress state considering the stress triaxiality and the lode parameter. *Acta Mechanica Sinica*. 2013, **26**(6), 642–658.
- [63] RICE, J. R. and D. M. TRACEY. On the ductile enlargement of voids in triaxial stress fields. *Journal of the Mechanics and Physics of Solids*. 1969, **17**(3), 201–217.
- [64] BROZZO, P., B. DELUCA and R. RENDINA. A new method for the prediction of formability limits in metal sheets. *Proceeding of the seventh Biennial Conference of the International Deep Drawing Research Group*. 1972, pp. 3.1–3.5.
- [65] OH, S. I., C. C. CHEN and S. KOBAYASHI. Ductile fracture in axisymmetric extrusion and drawing – part 2: workability in extrusion and drawing. *Journal of Manufacturing Science and Engineering*. 1979, **101**(1), 36–44.
- [66] KO, Y. K., J. S. LEE, H. HUH, H. K. KIM and S. PARK. Prediction of fracture in hub-hole expanding process using a new ductile fracture criterion. *Journal of Materials Processing Technology*. 2007, **187–188**, 358–362.

- [67] ŠEBEK, F. *Advanced multiaxial criteria in ductile fracture prediction*. Brno, 2020. Habilitation Thesis. University of Technology Brno.
- [68] VOBEJDA, R., F. ŠEBEK, P. KUBÍK and J. PETRUŠKA. Solution to problems caused by associated non-quadratic yield functions with respect to the ductile fracture. *International Journal of Plasticity*. 2022, **154**(4), 103301.
- [69] GANJIANI, M. A damage model for predicting ductile fracture with considering the dependency on stress triaxiality and Lode angle. *European Journal of Mechanics – A/Solids*. 2020, **84**(4), 101048.
- [70] GANJIANI, M. and M. HOMAYOUNFARD. Development of a ductile failure model sensitive to stress triaxiality and Lode angle. *International Journal of Solids and Structures*. 2021, **225**, 111066.
- [71] KUBÍK, P., J. PETRUŠKA, J. HŮLKA. A new ductile fracture criterion of aluminium alloy. *Modelling and Optimization of Physical Systems*. 2013, **12**, 43–46.
- [72] ŠEBEK, F., N. PARK, P. KUBÍK, J. PETRUŠKA and J. ZAPLETAL. Ductile fracture predictions in small punch testing of cold-rolled aluminium alloy. *Engineering Fracture Mechanics*. 2018, **206**(2), 509–525.
- [73] ŠEBEK, F., J. PETRUŠKA and P. KUBÍK. Lode dependent plasticity coupled with nonlinear damage accumulation for ductile fracture of aluminium alloy. *Materials and Design*. 2018, **137**, 90–107.
- [74] LOU, Y., H. HUH, S. LIM and K. PACK. New ductile fracture criterion for prediction of fracture forming limit diagrams of sheet metals. *International Journal of Solids and Structures*. 2012, **49**(25), 3605–3615.
- [75] LOU, Y., L. CHEN, T. CLAUSMEYER, A. E. TEKKAYA and J. W. YOON. Modeling of ductile fracture from shear to balanced biaxial tension for sheet metals. *International Journal of Solids and Structures*. 2017, **112**, 169–184.
- [76] SONG, M. P. and G. C. GU. Research on particle swarm optimization: a review. *Proceedings of 2004 International Conference on Machine Learning and Cybernetics*. 2004, **4**, 2236–2241.
- [77] WANG, D., D. TAN and L. LIU. Particle swarm optimization algorithm: an overview. *Soft Computing*. 2018, **22**(2), 387–408.
- [78] *What Is Particle Swarm Optimization?* [online]. MATHWORKS [cit. 2022-10-09]. Available from: <https://www.mathworks.com/help/gads/what-is-particle-swarm-optimization.html>
- [79] BRATTON, D. and J. KENNEDY. Defining a standard for particle swarm optimization. *2007 IEEE Swarm Intelligence Symposium*. 2007, 120–127.
- [80] LOU, Y. and H. HUH. Prediction of ductile fracture for advanced high strength steel with a new criterion: experiments and simulation. *Journal of Materials Processing Technology*. 2013, **213**(8), 1284–1302.

- [81] ZHANG, S., Y. LU, Z. SHEN, C. ZHOU and Y. LOU. Prediction of ductile fracture for Al6016-T4 with a ductile fracture criterion: experiment and simulation. *International Journal of Damage Mechanics*. 2020, **29**(8), 1199–1221.
- [82] 2024-T351 Aluminium [online]. Star Rapid [cit. 2022-09-26]. Available from: <https://www.starrapid.com/wp-content/uploads/2019/10/2024-T351.pdf>
- [83] EN AW 2024: the aerospace aluminum alloy 2024 clad (WL 3.1364) and unclad (WL 3.1354) for highly stressed parts [online]. ROBEMETALL [cit. 2022-10-06]. Available from: <https://www.robemetall.de/en/products/aluminum/en-aw-2024>
- [84] Aluminum 2024-T4; 2024-T351 [online]. MATWEB [cit. 2022-10-06]. Available from: <https://www.matweb.com/search/DataSheet.aspx?MatGUID=67d8cd7c00a04ba29b618484f7ff7524&ckck=1>
- [85] EN AW-2024 AlCu4Mg1 [online]. PROAL [cit. 2022-10-06]. Available from: <https://proal.cz/hlinik /slitiny-hliniku/en-aw-2024>
- [86] RASOCHA, D. *Control system design for small test machine*. Brno, 2020. Master's Thesis. University of Technology Brno. Supervisor S. VĚCHET.
- [87] VEJCHODA, O. *Application of DIC method for measurement of deformations on small specimens*. Brno, 2020. Master's Thesis. University of Technology Brno. Supervisor T. NÁVRAT.

LIST OF USED ABBREVIATIONS AND SYMBOLS

A	Initial resisting area
\tilde{A}	Effective resisting area
c_η, c_θ	Material parameters of Ganjani criterion
$c_{rel}, c, m, n_{TC}, n_\xi$	Material parameters of yield function
c_1, c_2	Material constants of modified Mohr–Coulomb criterion
C_{R-T}	Material constant of Rice–Tracey criterion
C_{Oh}	Material constant of Oh criterion
C_{K-H}	Material constant of Ko–Huh criterion
C_{C-L}	Material constant of Cockcroft–Latham criterion
C_B	Material constant of Brozzo criterion
C_1, C_2, C_3, C_4, C_5	Material constants of Lou–Huh criterion
D	Damage parameter
D_1, \dots, D_6	Material constants of Bai–Wierzbicki criterion
e	Engineering strain
\underline{e}^p	Deviatoric plastic strain tensor
E	Young’s modulus
\tilde{E}	Effective Young’s modulus
$f(\eta, \bar{\theta})$	Function of damage parameter
f	Yield function
f_m	Minimized residuum function
$f_{(c)}$	Relation function
G_1, \dots, G_6	Material constants of KHPS2 criterion
I_1, I_2, I_3	First, second and third invariants of the Cauchy stress tensor
\underline{I}	Identity tensor
J_1, J_2, J_3	First, second and third invariants of the stress deviator
k	Correction function
k_a, k_b, a_m, b_m	Material parameters of yield function
K	Strength coefficient of Swift hardening law
m	Material constant
M	Mass
n	Strain hardening exponent
N_w	Number of grains in whole workpiece
N_s	Number of surface grains
p, q, r	Invariants of stress tensor
p	Hydrostatic pressure
Q	Plastic potential
r	Radius of yield surface in deviatoric plane
s	Engineering stress

S	Deviatoric stress
S_1, S_2, S_3	Principal deviatoric stresses
\underline{S}	Deviatoric stress tensor
v	Velocity
V	Volume
α, β	Functions of ξ of the yield function
φ, z	Coordinates in the stress space
ρ	Density
λ	Plastic multiplier
σ	Normal stress
σ_{yT}	Yield stress in tension
σ_{yC}	Yield stress in compression
σ_y	Yield stress
$\sigma_x, \sigma_y, \sigma_z$	Normal stresses of the stress tensor
σ_s	Flow stress of surface grains
σ_m	Mean stress
σ_i	Flow stress of inner grains
$\sigma_I, \sigma_{II}, \sigma_{III}$	Principal stresses not ordered according to the magnitude
$\sigma_1, \sigma_2, \sigma_3$	Principal stresses ordered according to the magnitude
$\bar{\sigma}$	Equivalent stress
$\underline{\sigma}$	Stress tensor
$\tilde{\sigma}$	Effective stress
$\bar{\sigma}_f^{ref}$	Equivalent fracture stress of reference test
$\bar{\sigma}_f$	Equivalent fracture stress
$\tau_{xy}, \tau_{xz}, \tau_{yz}$	Shear stresses of the stress tensor
ε	True strain
$d\underline{\varepsilon}^p$	Plastic strain tensor increment
$\varepsilon_x^e, \varepsilon_y^e, \varepsilon_z^e$	Diagonal elastic strain components of the elastic strain tensor
ε_p	Plastic part of true strain
$\bar{\varepsilon}_f^{ref}$	Equivalent fracture strain of reference test
ε_0	Reference strain
$\underline{\varepsilon}$	Strain tensor
$\bar{\varepsilon}_p$	Equivalent plastic strain
$\underline{\varepsilon}^p$	Plastic strain tensor
$\dot{\varepsilon}^p$	Plastic strain rate
$\bar{\varepsilon}_f$	Fracture strain
$\hat{\varepsilon}_f$	Fracture strain of calibration point
$\underline{\varepsilon}^e$	Elastic strain tensor
$\dot{\bar{\varepsilon}}^p$	Equivalent plastic strain rate

$\underline{\dot{\xi}}^p$	Plastic strain rate tensor
ξ	Normalized third invariant of the deviatoric stress tensor
ξ_{av}	Averaged normalized third invariant of the deviatoric stress tensor
η	Stress triaxiality
η_s	Size factor
η^{ref}	Stress triaxiality of reference test
η_c	Cut-off stress triaxiality
η_{av}	Average value of stress triaxiality
θ	Lode angle
θ_A	Azimuth angle
$\bar{\theta}$	Normalized Lode angle
$\bar{\theta}^{ref}$	Normalized Lode angle of reference test
$\bar{\theta}_{av}$	Average value of normalized Lode angle
μ	Lode parameter
μ_p	Poisson's ratio
κ	Curvature
$tr(...)$	Trace
\times	Multiplication
$:$	Double dot product
$\langle ... \rangle$	Macaulay bracket
$... $	Absolute value
DIC	Digital Image Correlation
FEM	Finite Element Method
LSM	Least Squares Method
PSO	Particle Swarm Optimization
SPT	Small Punch Test
EDM	Electrical Discharge Machine

LIST OF FIGURES

Fig. 1 Stages of the ductile fracture process [9]	14
Fig. 2. Distribution of grains with decreasing geometrical size [13]	16
Fig. 3 Basic overview of flat miniature specimen geometries	17
Fig. 4 SPT setup [20]	18
Fig. 5 Butterfly specimens [22]	18
Fig. 6 General stress–strain diagram of ductile materials [27]	21
Fig. 7 Haigh–Westergaard stress space [33]	23
Fig. 8 Representation of various stress states in the plane of η and ξ [36]	25
Fig. 9 Dependence of ξ , θ , θ_A , μ parameters on stress triaxiality η for plane stress	26
Fig. 10 Geometrical representation of the deviatoric stress in the deviatoric plane	27
Fig. 11 Flowchart of the ductile fracture simulation process [36]	29
Fig. 12 Representation of the stress and strain increment of the associated flow rule	31
Fig. 13 Kinematic and isotropic hardening [50]	32
Fig. 14 Bauschinger effect [51]	32
Fig. 15 Fitted flow curve [29]	38
Fig. 16 Yield locus in the deviatoric plane [68]	41
Fig. 17 Graphical representation of material constants of the KHPS2 criterion [67]	44
Fig. 18 Flowchart of the particle swarm optimization algorithm [77]	46
Fig. 19 Calibrated ductile fracture criteria	48
Fig. 20 Location of calibration points in stress triaxiality – equivalent plastic stain plane	51
Fig. 21 Location of calibration points and cut-off stress triaxiality in $\xi - \eta$ plane	51
Fig. 22 Comparison of the KHPS2 calibration	52
Fig. 23 Comparison of kinetic and internal energy during numerical simulation	54
Fig. 24 Plane strain specimen	55
Fig. 25 Notched R4 specimen	55
Fig. 26 Uniaxial tension specimen	55
Fig. 27 Shear specimen	55
Fig. 28 Initially proposed shear specimen	57
Fig. 29 Model of the uniaxial tension specimen	57
Fig. 30 Model of the notched R4 specimen	58
Fig. 31 Model of the plane strain specimen	58
Fig. 32 Model of the shear specimen	59
Fig. 33 Shear specimen	60
Fig. 34 Evolution of stress triaxiality	60
Fig. 35 Evolution of normalized third invariant of the deviatoric stress tensor	61
Fig. 36 Test apparatus [86]	63
Fig. 37 Orientation of the samples relative to the rolling direction	63
Fig. 38 Designed specimens	63
Fig. 39 Detail of the test apparatus	64
Fig. 40 Force–displacement responses of the notched specimens	65
Fig. 41 Force–displacement responses of the shear specimens	66
Fig. 42 Force–displacement responses of the plane strain specimens	67
Fig. 43 Force–displacement responses of the uniaxial specimens	67
Fig. 44 Tested specimens	68
Fig. 45 Force–displacement response of the SPT	69
Fig. 46 Model of the SPT	70
Fig. 47 SPT test apparatus [72]	70